---

Editorial Office of *Earth's Cryosphere (Kriosfera Zemli)*
Institute of Geography, Russian Academy of Sciences
37 Vavilov St., office 22, Moscow, 117312, Russia
Editorial staff: *N.V. Arutyunyan, N.G. Belova, O.M. Lisitsyna, G.E. Oblogov*
Phone: +7(985) 957-10-01, e-mail: kriozem@gmail.com
Editor of the English translation: *D.E. Konyushkov*

**Journal promoted by**
Russian Academy of Sciences, Siberian Branch, Novosibirsk
Earth's Cryosphere Institute, Tyumen Scientific Centre SB RAS, Tyumen
Melnikov Permafrost Institute, SB RAS, Yakutsk

Editorial Manager *M.A. Trashkeeva*
Designed by *N.F. Suranova*
Typeset by *N.M. Raizvikh*

**RUSSIAN ACADEMY OF SCIENCES**
SIBERIAN BRANCH
EARTH'S CRYOSPHERE INSTITUTE, TYUMEN SCIENTIFIC CENTRE
MELNIKOV PERMAFROST INSTITUTE

**EARTH'S CRYOSPHERE**
SCIENTIFIC JOURNAL

| Founded in January 1997 | 6 issues per year | Vol. XXVI, No. 6 | November–December 2022 |
|---|---|---|---|

## CONTENTS

**EARTH'S CRYOSPHERE**
SCIENTIFIC JOURNAL

*Earth's Cryosphere*, 2022, vol. XXVI, No. 6, pp. 3–12

*REGIONAL AND HISTORICAL GEOCRYOLOGY*

# SOURCES OF POLLEN GRAINS IN WINTER PRECIPITATION OF THE ALTAI TERRITORY

**N.A. Kuryatnikova*, N.S. Malygina**

*Institute for Water and Environmental Problems, Siberian Branch of the Russian Academy of Sciences, Molodezhnaya St. 1, Barnaul, 656038 Russia*

**Corresponding author; e-mail: ryabchinnatalia@gmail.com*

The results of microscopic analysis of 118 samples of solid precipitation (snow) collected during the cold season of 2019/2020 at three key points located in the Altai Territory in the neighboring Altai–Sayan and Tobol–Irtysh glaciological regions and on their border are presented. In 45 samples (38%), advective pollen grains of trees (*Betula* sp., *Pinus* sp.) and herbs (*Artemisia* sp., family Asteraceae, Amranthaceae s.l. (incl. Chenopodiaceae), Fabaceae, Poaceae) were identified. Territories were identified from which pollen grains arrived with air masses that caused precipitation during the cold season. Advective pollen of wormwood (*Artemisia* sp.) was brought from the territory of the Kazakh Upland and was determined in the snow of both glaciological regions and on their border. Pollen grains of Amaranthaceae s.l. (incl. Chenopodiaceae) were introduced from the plains of Kazakhstan and, partially, from the snow-free slopes of the Altai Mountains and from the Middle Ob Lowland. Pollen grains of Fabaceae family were only found in the snow of the Altai–Sayan glaciological region, while pollen grains of Poaceae family were found in the snow of the Tobol–Irtysh region; in the border zone of these two glaciological regions, pollen grains of these taxa were not found.

***Keywords:*** *pollen, winter precipitation (snow), Altai Territory, Altai–Sayan glaciological region, Tobol–Irtysh glaciological region.*

***Recommended citation:*** Kuryatnikova N.A., Malygina N.S., 2022. Sources of pollen grains in winter precipitation of the Altai Territory. *Earth's Cryosphere* **26** (6), 3–12.

## INTRODUCTION

Intensive warming in recent decades has led to a widespread reduction in cryosphere objects and a significant mass loss of glaciers (outside Greenland and Antarctica) equal to 220 ± 30 Gt/yr (2006–2015), as well as to an increase in the temperature of permafrost by 0.29 ± 0.12°C (2007–2016) on average for the polar and high mountain regions of the world [*IPCC, 2019*]. In this regard, in the near future, considerable attention should be focused on research, primarily in those regions where multi-level nival-glacial systems are located, in the material composition of which ice and snow cover play a leading role, and which are sensitive to climatic changes [*Kotlyakov, 2004*]. One of the main methods of research in nival-glacial systems is the creation of real models that describe the dynamics of the objects included in them and their relationship both with one another and with other components of the environment [*Kotlyakov et al., 1984*]. In this type of modeling, reliable markers are used, for example, pollen grains, which reflect the relationship of elements in the studied nival-glacial system not only among themselves but also with natural systems of the same or adjacent hierarchical level. This is due to the fact that pollen is well preserved, as it has a shell resistant to external influences, and pollen spectra have already proven to be reliable indicators of paleoecological and paleoclimatic events, including those in the cryosphere [*Festi et al., 2017; Brugger et al., 2018*].

Pollen grains enter the cryosphere from the biosphere, mainly through the atmosphere as a result of sedimentation processes (dry deposition) or intracloud and undercloud washout (wet deposition). The contribution of dry deposition to the overall input of particles of biological origin from the atmosphere to the underlying surface in temperate latitudes can be only 10–20% [*Ivlev, 1999*], and its consideration is more important in local studies, since the contribution of dry deposition is often leveled out [*Fröhlich-Nowoisky et al., 2016*]. During wet deposition, snow washes away aerosols (including pollen grains) three–four times more efficiently than rain [*Semenchenko, 2002*]. However, studies devoted to the analysis of the supply and settling of pollen grains with atmospheric precipitation, especially in the form of snow, are scarce and localized [*Malygina et al., 2018; Kasprzyk, Borycka, 2019*].

In Poland, such studies were sporadic and were conducted only during the snowfall period (March 2018), when blossoming of *Alnus* sp. – one of the al-

lergenic plants – took place in Europe [*Kasprzyk, Borycka, 2019*]. In the Altai Territory, studies of the supply of pollen grains with snow were carried out during the cold season of 2014/2015, when vegetation was completely absent. At the same time, pollen grains of *Betula* sp., *Populus* sp., *Pinus* sp., and *Salix* sp. were identified in the selected samples, and the main areas from which these grains could come as a result of secondary uplift from the underlying surface were identified [*Malygina et al., 2018*]. In continuation of this work, the authors selected three key research points located at a distance of about 300 km from one another in adjacent hierarchical units of glaciological zoning. This zoning [*Kotlyakov, 1997*] is essentially a physical-geographical zoning, in which glacial landscapes are in the foreground, and when distinguishing structural units, atmospheric circulation (for provinces) and macrorelief features (for regions) are taken into account.

The key research points are located in the Altai Territory (Fig. 1) in neighboring glaciological regions and at their junction and are characterized by different synoptic conditions due to differentiation in the amount of solar radiation and atmospheric circulation regimes [*Kharlamova, 2013*], which is reflected in the vegetation cover of the territories. Key point (KP) 1 is located in the Altai–Sayan region of the Atlantic–North Eurasian glaciological province [*Kotlyakov, 1997*] at 244 m a.s.l., in the area with zonal forest-steppe vegetation largely converted to cropland. Within the valley-gully systems, there are meadow forb-grass steppes and grass-forb steppe meadows, aspen-birch gully forests, true and marshy meadows; along the Ob River terraces, pine and mixed forests [*Vinokurov, Tsimbaley, 2016; Landscape map..., 2016*]. Key point 2 is located in the Tobol–Irtysh region of the Atlantic–Eurasian province at 186 m a.s.l. in the subzone of the moderately arid steppe of the steppe zone of the Altai Territory. Zonal steppe vegetation is almost completely destroyed by plowing. Rich herb-turf-grass steppes, aspen-birch groves, and solonetz-salt marsh complexes are preserved in badland areas; pine and mixed forests are present within the Kasmalinsky hollow of the ancient runoff.

Key point 3 is located on the border of the Tobol–Irtysh and Altai–Sayan glaciological regions at 181 m a.s.l. in the northwestern part of the subzone of the middle forest-steppe of the forest-steppe zone of the Altai Territory. Most of the zonal forest-steppe vegetation has been replaced by arable land. Meadow forb-grass steppes and grass-forb steppe meadows, aspen-birch gully forests, real and marshy meadows are widespread along the valleys, logs, and gullies; along the terraces of the Ob River, there are pine and mixed forests.


**Fig. 1. Location of key points.**

*1* – state borders; *2* – border of Altai Territory; *3* – key point.

The main goal of this work was to study the taxonomic diversity of pollen grains in the snow that fell in neighboring glaciological regions (Altai–Sayan and Tobol–Irtysh) and in the zone of their contact, as well as to determine areas, from which advective pollen grains were transported with air masses to assess the possibility of their further use as markers of the processes of matter input into the nival-glacial systems.

## METHODS

### Sampling and microscopic analysis of precipitation

Snow samples, immediately after the end of each snowfall, were taken into cylindrical samplers with a volume that contained no less than the maximum daily amount of precipitation. Before use, the samplers were preliminarily washed with distilled water and installed immediately before the onset of precipitation. After the end of the snowfall, the obtained samples from the sampler were poured into plastic bags and hermetically sealed until the start of the analysis in order to exclude the secondary ingress of pollen. In total, during the cold period under study (from November 8, 2019 to March 10, 2020), 118 snow samples were taken at three key points. It is important to note that sampling was carried out during the period with a complete absence of vegetation, after the formation of a stable snow cover, which acted as a limiting factor and limited the secondary rise of pollen grains from the underlying surface at the sampling site. Before treatment, the samples were stored at subzero temperatures. In the laboratory, the samples were melted in the same polyethylene bags at room temperature, and then they were poured into prepared containers of a suitable volume, and 40% formalin was added to reduce the development of microflora. Further, according to the hydrobiological method [*Abakumov et al., 1992*], the samples were settled in a dark, cool place for 7–10 days, depending on the volume, and concentrated by decantation. The prepared samples were examined under a light microscope at 400× magnification and a Nageotte counting chamber with a volume of 0.2 mL was used to quantify the identified particles in a certain volume. Atlases [*Kupriyanova, Aleshina, 1972, 1978; Dzyuba, 2005; Karpovich et al., 2015*] and international databases [*https://www.paldat.org/search/A; https://pollenatlas.net/homepage*] were used to identify the species.

### Trajectory, synoptic, and cartographic analyses

To determine the areas from whose territories pollen grains could come with air masses as a result of secondary uplift, trajectory analysis was used, the parameters of which were adjusted relative to previously tested options [*Malygina et al., 2018*]. To do this, for each date of precipitation, using the HYSPLIT model (Hybrid Single Particle Lagrangian Integrated Trajectory [*https://www.ready.noaa.gov/HYSPLIT.php*]), we calculated the reverse trajectories of air masses.

The trajectories were built using the GDAS (Global Data Assimilation System) archive [*https://www.ncei.noaa.gov/products*], which has a high spatial resolution (grid of 0.25° by 0.25°). The heights, for which the reverse trajectories of the movement of air masses were calculated, were chosen taking into account the fact that, entering the atmosphere, biological particles, including pollen, are most often in the surface layer for the first time, the thickness of which depends on the nature of the underlying surface, time of day, temperature of environment, wind speed, and a number of other parameters. This layer of the atmosphere is characterized by the presence of turbulent flows that promote the movement of particles not only in the horizontal but also in the vertical direction, while the vertical transport of particles from the lower layers to the upper layers is carried out under the action of convective flows, and the horizontal transport is of advective nature [*Semenchenko, 2002*].

The surface layer is the lowest part of the atmospheric boundary layer (ABL), but at its upper boundary it is covered by an inversion layer that prevents further vertical mixing of air masses and, as a result, limits the entry of particles into higher layers [*Brunet et al., 2017*]. At the same time, at the upper boundary of the ABL, the wind direction almost always corresponds to the direction of the isobars, and the ABL heights can reach 1500–2000 m [*Semenchenko, 2002*]. In this regard, when calculating the reverse trajectories of the movement of air masses that cause precipitation, the ABL heights according to the ERA5 reanalysis data were used [*https://www.ecmwf.int/en/forecasts/datasets/reanalysis-datasets/era5*].

The reverse trajectories of the movement of air masses were calculated for a period of at least 120 h, which exceeded the most frequently used time intervals in aerobiological studies [*Hernandez-Ceballos et al., 2014*]. During this period, air masses could form over areas open from snow. The obtained reverse trajectories were then verified, first of all, using the analysis of daily surface maps (AT-1000) and, if necessary, baric topography maps (AT-500) [*http://www.aari.ru/*]. Also, data on changes in geopotential heights, wind directions and speeds from NCEP/NCAR [*https://www.esrl.noaa.gov/psd/data*] for 1000, 925, and 850 mbar were used. For each date of precipitation sampling, maps of the distribution of snow and ice cover [*https://www.natice.noaa.gov/pub/ims/ims_v3/ims_gif/ARCHIVE/EuAsia/2019/*] were analyzed as the factors preventing he secondary rise of pollen grains from the underlying surface and

thereby limiting the number of potential areas from which pollen could come. For all the identified taxa, the areas of their distribution were analyzed for the territories corresponding to the routes of the reverse trajectories of air masses [*http://www.euforgen.org/*].

Thus, in the course of this work based on the previously obtained results [*Malygina et al., 2018*], an approach was implemented that allows one to determine the areas, from which pollen grains could come and fall with snow. Thus, we took fresh snow samples immediately after each snowfall during the cold season at the selected key points and then analyzed them under a microscope to identify pollen grains. Further, both for the dates of precipitation and for previous periods (3–5 days), synoptic conditions were analyzed and ABL heights were determined, which were subsequently used to calculate the reverse trajectories of air masses that caused precipitation. In parallel, we analyzed the ranges of the identified taxa and the maps of snow cover distribution in order to determine the areas, from which the isolated pollen grains could come.

## RESULTS AND DISCUSSION

### Pollen spectra in precipitation

The microscopic analysis showed that in 45 out of 118 (i.e., 38%) event snow samples taken at three key points, pollen grains of trees (*Betula* sp., *Pinus* sp.) and grasses (*Artemisia* sp., families Asteraceae, Amaranthaceae s.l. (incl. Chenopodiaceae), Fabaceae, Poaceae) were present. These pollen grains presumably had an advective nature of entry as a result of the secondary rise from the underlying surfaces of areas open from snow, over which air masses causing precipitation could pass.

The maximum contribution (56%) to the formation of the total spectrum was made by tree pollen dominated by pine (*Pinus* sp.) (32% of the total spectrum); birch pollen (*Betula* sp.) was less frequent (24%) (Fig. 2). A large number of tree pollen grains is explained by the high pollen productivity of the trees and their anemophilic (wind-pollinated) pollination. Thus, birch pollen can be transported for a thousand kilometers, and pine pollen, due to morphological features (presence of dead-air spaces), for several thousand kilometers [*Karpovich et al., 2015*].

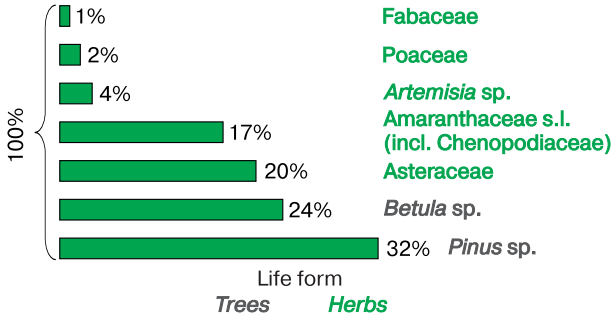


**Fig. 2. Taxonomic diversity in the total pollen spectrum of snow samples 2019/2020.**

Grass pollen is more diverse than tree pollen, but its contribution to the total pollen spectrum was only 44%, with pollen of the Asteraceae family (20%) dominating. A significant contribution (17%) to the overall spectrum was made by pollen grains of representatives of the Amaranthaceae s.l. (incl. Chenopodiaceae), while pollen of other herbs was present in much lower amounts: wormwood (*Artemisia* sp.) 4%, cereals (Poaceae) 2%, legumes (Fabaceae) 1%. Grass pollen, unlike tree pollen, is mainly transported within the range, but under the influence of advective flows, it can rise to considerable heights and be transported over long distances [*Golovko, 2004*].

The concentrations of pollen grains identified in the snow samples of each key point varied significantly (Table 1). Thus, the concentration of pollen of representatives of the family Asteraceae varied from 12 (KP 1) to 960 grains/L (KP 3). Among tree pollen, the maximum concentration (up to 640 grains/L) was found for *Betula* sp. in single samples from KP 1 and KP 3.

It should be noted that the taxonomic diversity of pollen grains identified in snow samples from three study sites is consistent with data obtained for an ice core sampled in Altai (Belukha massif) [*Papina et al., 2013*]. The low taxonomic diversity of pollen spectra in cryosphere objects (glaciers, snowfields, snow cover, etc.) is associated with the features of their formation, which is largely determined by circulation fea-

Table 1. **Pollen concentration (grains/L) in snow samples**

| Taxon | Key point | | |
|---|---|---|---|
| | 1 | 2 | 3 |
| | *Trees* | | |
| *Betula* sp. | 40–640 / 156 | 36–250 / 145 | 41–640 / 158 |
| *Pinus* sp. | 39–120 / 41 | 20–500 / 127 | 41–390 / 169 |
| | *Herbs* | | |
| *Artemisia* sp. | 0–13 / 6 | 0–252 / 84 | 0–150 / 37 |
| Asteraceae | 12–109 / 54 | 92–500 / 103 | 35–960 / 205 |
| Amaranthaceae s.l. (incl. Chenopodiaceae) | 22–24 / 23 | 53–518 / 225 | 26–118 / 57 |
| Poaceae | – | 0–129 / 64 | – |
| Fabaceae | 0–112 / 24 | – | – |

Note: Numerator, minimum and maximum values; denominator, average value.

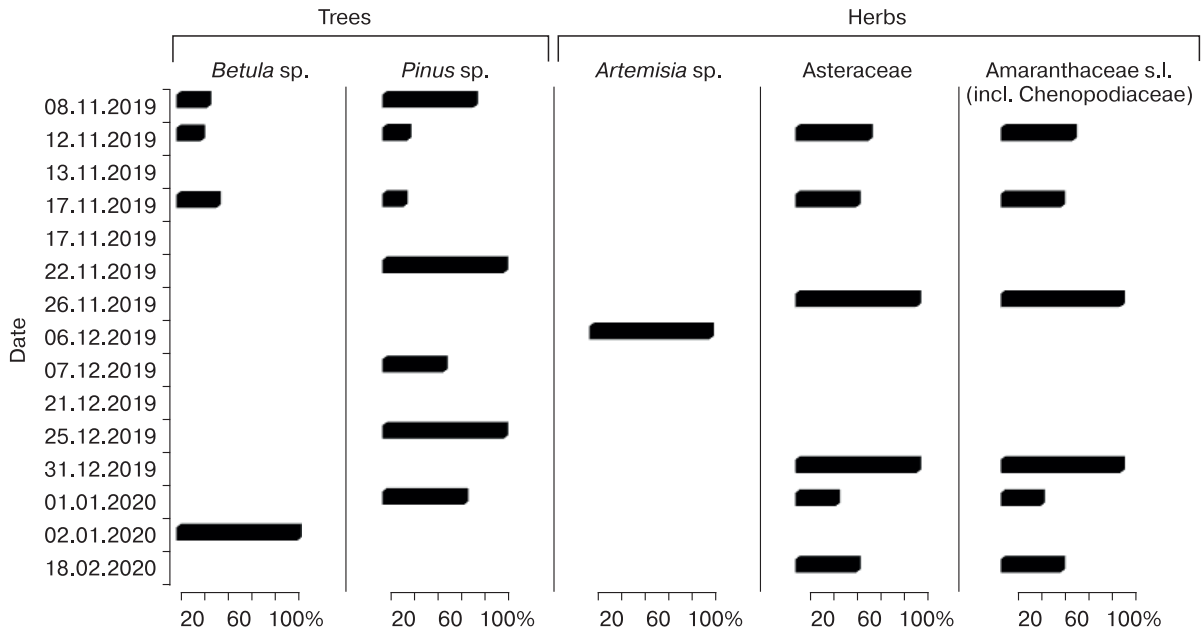


**Fig. 3. Pollen diagram of key point 3.**

tures [*Bourgeois, 2000*], and the diversity of pollen spectra can often differ significantly from the diversity of vegetation in the studied area.

It is important to note that the maximum number of samples (more than 40%) was taken at KP 3 on the border of glaciological areas; these samples were also characterized by the maximum number of identified pollen grains (Fig. 3).

Of the seven identified taxa, only five were identified in the samples from this point, and pine pollen (*Pinus* sp.) was dominant (34%) (Table 2), most of which was isolated in samples from the beginning of the cold season (Fig. 3). The contribution of pollen from representatives of the family Asteraceae and *Betula* sp. amounted to 26% and 21%, respectively, the maximum of which was also recorded in the samples from the beginning of the cold season. The pollen of representatives of the family Amaranthaceae s.l. (incl. Chenopodiaceae) accounted for 16% of the total spectrum and was identified in samples from the beginning and middle of the cold season. Pollen grains of *Artemisia* sp. were determined only in the snow sample taken on December 6, 2019, and their share in the total spectrum at this key point did not exceed 3% (Table 2).

At KP 1 in the cold season of 2019/2020, only 31 snow samples were taken (27% of the total number of samples), in 13 of which pollen was isolated (Fig. 4). The pollen spectrum in the samples from this point was very diverse and was represented by six taxa. The spectrum was dominated by birch pollen (*Betula* sp.) (41%) (Table 2), and most of birch pollen grains were identified in the samples taken at the beginning of the cold season (Fig. 4), in contrast to birch pollen in samples from KP 2 and KP 3. Among herbs, as well as at KP 3, pollen of representatives of the fam. Asteraceae predominated.

In 39 snow samples taken at KP 2, 34% of the total number of pollen grains counted in all samples were identified. A distinctive feature of the pollen spectrum at KP 3 was the predominance (51%) of pollen grains of herbs represented by *Artemisia* sp. and Asteraceae, Amaranthaceae s.l. (incl. Chenopodiaceae), and Poaceae families (Table 2).

The largest proportion of grass pollen was accounted for by representatives of the family Amaranthaceae s.l. (incl. Chenopodiaceae) – 26%, which

Table 2. **Contribution (%) of individual taxa to the total pollen spectrum of snow samples taken in the cold season of 2019/2020**

| Taxon | Key point | | |
|---|---|---|---|
| | 1 | 2 | 3 |
| *Trees* | | | |
| *Betula* sp. | 41 | 10 | 21 |
| *Pinus* sp. | 26 | 39 | 34 |
| Total tree pollen | 67 | 49 | 55 |
| *Herbs* | | | |
| *Artemisia* sp. | 3 | 5 | 3 |
| Asteraceae | 19 | 15 | 26 |
| Amaranthaceae s.l. (incl. Chenopodiaceae) | 8 | 26 | 16 |
| Poaceae | 0 | 5 | 0 |
| Fabaceae | 3 | 0 | 0 |
| Total herb pollen | 33 | 51 | 45 |
| Total pollen spectrum | 100 | 100 | 100 |

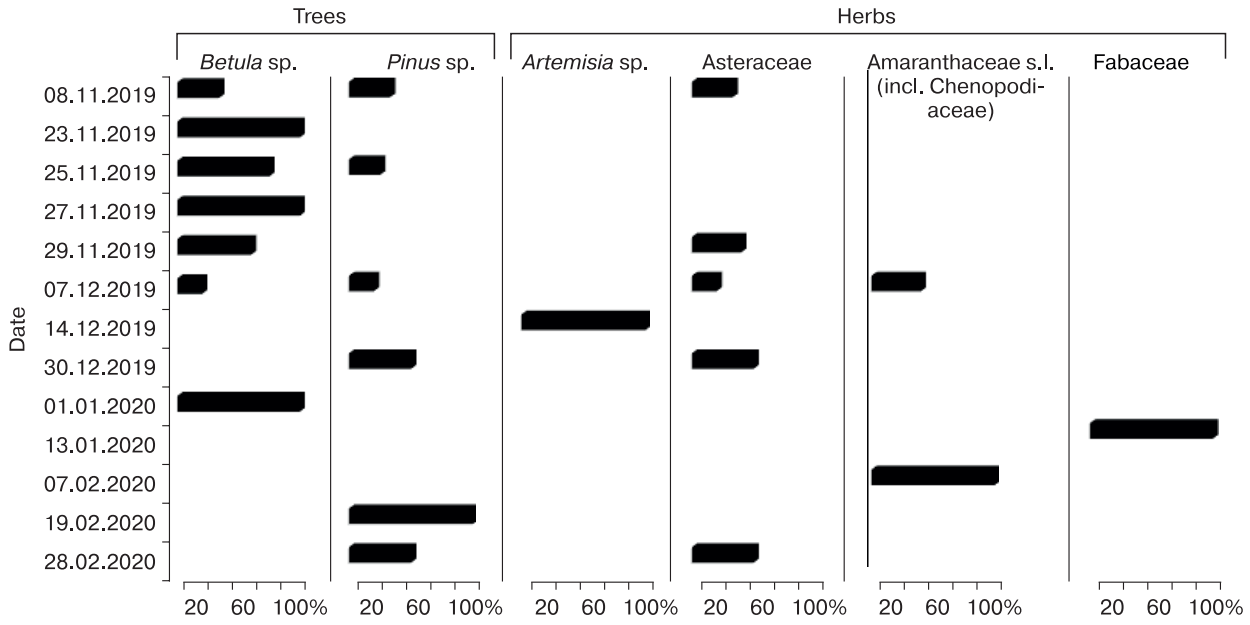


**Fig. 4. Pollen diagram of key point 1.**

were isolated in samples from the beginning of the cold season of 2019/2020 (Fig. 5). The proportion of Chenopodiaceae here was three times higher than that at KP 1 and one and a half times higher than that at KP 3. In the spectrum from KP 2, pollen of *Artemisia* sp. constituted 5% of the total pollen spectrum (Table 2) and it was only found in the samples from December 2019, as well as at the other key points. Grass pollen (family Poaceae) was identified only in the spectrum of KP 2 and amounted to 5% (Table 2). Among the trees, pine pollen (*Pinus* sp.) prevailed (39%); it was detected in the samples taken during the first half of the cold season. share of birch (*Betula* sp.) pollen in the pollen spectrum from KP 2 reached 10% and was the lowest in comparison with that at KP 1 and KP 3 (Table 2).

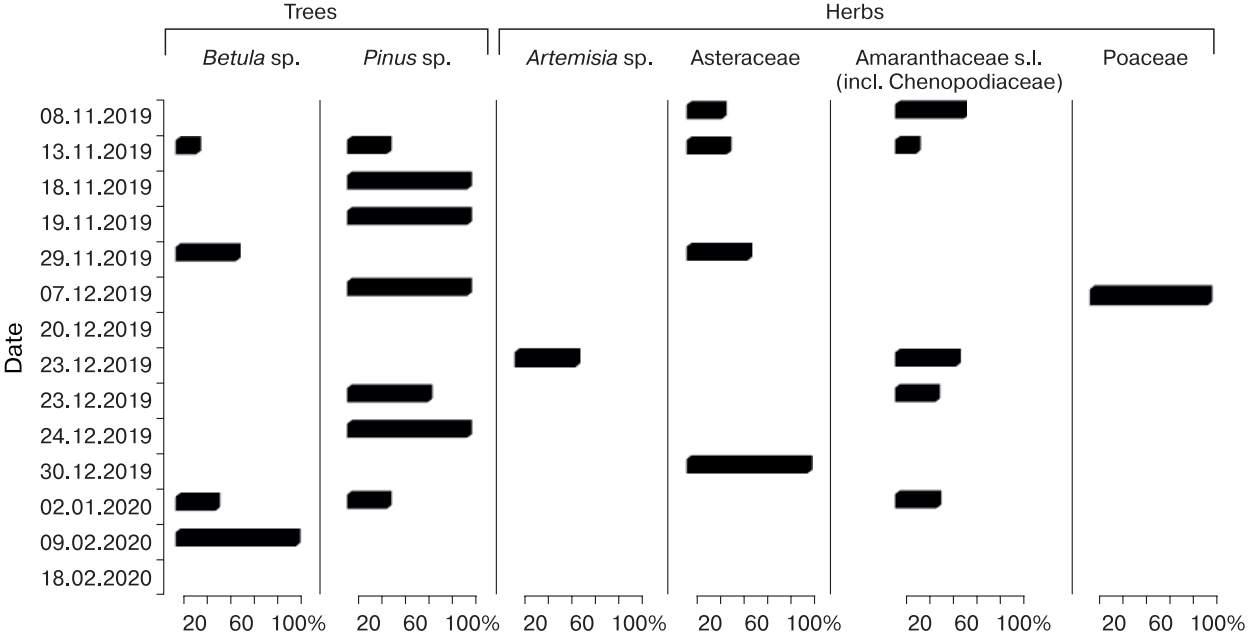


**Fig. 5. Pollen diagram of key point 2.**

### Areas, from which pollen grains came and were deposited with snow from air masses

The procedure to determine these areas is explained using the example of December 23, 2019, when pollen grains of wormwood (*Artemisia* sp.) were found in the sample taken at KP 2.

– The reverse trajectories of air mass movement were calculated (HYSPIT model) for the ABL height and duration of 120 h (Fig. 6*a*), which corresponds to the duration of the natural synoptic period for the study area.

– The ABL heights obtained from ERA 5 were used in calculations, as they ensure pollen transportation over considerable distances. Calculation with due account for the ABL heights is an important innovation of the approach in contrast to standard heights (500, 1500, 3000 m) previously used by the authors [*Malygina et al., 2018*].

– An analysis of synoptic situations was performed according to the AT-1000 baric topography maps, average wind speeds and directions according to NCEP/NCAR and ERA 5 data [*https://www.esrl.noaa.gov/psd/data*] for the heights of 1000, 925 and 850 mbar for the dates of precipitation events and for previous 3–5 days in order to verify the calculated trajectories.

– Delineation of the potential areas, from which the identified pollen grains could be brought.

– An analysis of available materials on the distribution of the identified taxa in the territory of the formation of air masses and along their route to confirm and refine the delineated areas.

– An analysis of the maps of snow cover distribution [*https://www.natice.noaa .gov/pub/ims/ims_v3/ims_gif/ARCHIVE/EuAsia/*] for the period of formation and movement of air masses that caused precipitation along their trajectory in order to exclude areas covered with snow, which limited the secondary rise of pollen grains from the underlying surface.

A comprehensive analysis of diverse data made it possible to determine that the air masses that caused snowfall on December 23, 2019 at KP 2 were formed over the Kazakh Uplands (Fig. 6*a*), which on this date and in advance (3–5 days) was free of snow, i.e., could act as a potential area for the entry of wormwood pollen. The direction of the calculated reverse trajectories of air mass movement was consistent with the direction of the wind (southwest) according to the maps of average wind speeds and directions (NCEP/NCAR) (Fig. 6*b*). The performed analysis of baric topography maps showed that at the time of the formation of air masses over the territory of the Kazakh Uplands, ascending flows prevailed (advection was observed) and facilitated the rise of pollen grains into air masses from the underlying surfaces that were not yet covered with snow. The absence of snow cover at the time of air mass formation is confirmed by the snow cover distribution maps, according to which the territories of key points and adjacent areas within a radius of 300 km were covered with snow, whereas the areas over which the formation of air masses took place were still free of snow during that period. The participation of wormwood in the vegetation cover of the Kazakh Uplands is significantly

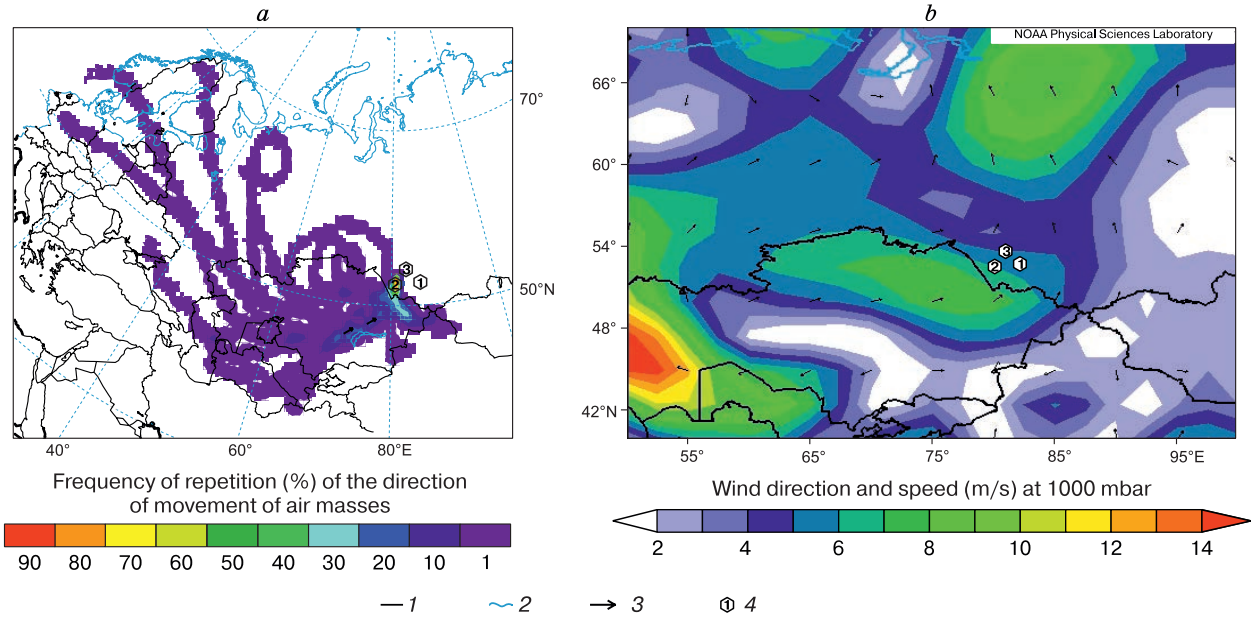


**Fig. 6. Reverse trajectories of air mass movement (*a*) [*https://www.ready.noaa.gov/HYSPLIT.php*] and map of average wind speed and direction (*b*) [*https://www.esrl.noaa.gov/psd/data*] on December 23, 2019.**

*1* – state border; *2* – coastline; *3* – wind direction; *4* – key point.

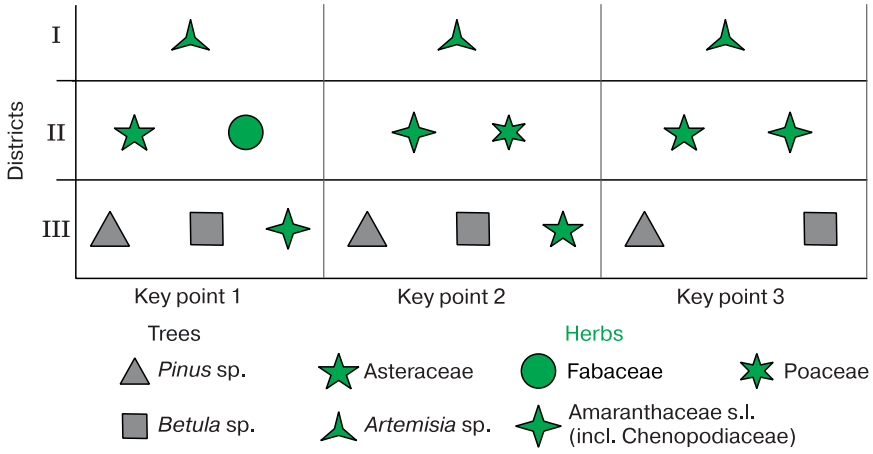


**Fig. 7. Areas of pollen grains supply to key points:**

(I) Kazakh Uplands, (II) plains of Kazakhstan, and (III) Altai Mountains and the Middle Ob Lowland.

large [*Polyakov, 1961*], which confirms the fact that this territory could be a source of pollen grains. The application of the approach described above made it possible to reliably determine the areas, from which wormwood pollen grains were brought to be deposited with snowfall at KP 2 on December 23, 2019.

For KP 1, pollen grains of wormwood (*Artemisia* sp.) were also introduced with air masses that formed over the Kazakh Uplands (Fig. 7). According to the analysis of the reverse trajectories of air masses, pollen grains of the families Asteraceae and Fabaceae with a high degree of probability (up to 70%) were brought from the plains of Kazakhstan, which were free of snow. Pollen grains of *Betula* sp. and *Pinus* sp. were brought from the still or already snow-free slopes of the Altai Mountains and from the Middle Ob Lowland (Fig. 7).

Wormwood (*Artemisia* sp.) isolated in samples from KP 2 also came from the Kazakh Uplands (Fig. 7). Pollen grains of grasses (Poaceae) that were only identified in samples taken at KP 2 came from the plains of Kazakhstan (Fig. 7), from which the pollen of Amaranthaceae s.l. (incl. Chenopodiaceae) was also introduced. Tree pollen (*Betula* sp., *Pinus* sp.) in samples from KP 2, as well as pollen of representatives of the family Asteraceae, came from the slopes of the Altai Mountains; at the beginning of the cold season of 2019/2020, it could also come from the snow-free areas of the Middle Ob Lowland.

The maximum contribution to the pollen spectrum at KP 3 at the border between the two glaciological regions was made by pollen grains of *Betula* sp. and *Pinus* sp. brought from the snow-free slopes of the Altai Mountains. As well as at KP 1 and KP 2, pollen of *Artemisia* sp. was brought from the snow-free areas of the Kazakh Uplands. Pollen grains of the families Asteraceae and Amaranthaceae s.l. (incl. Chenopodiaceae) ocame with air masses formed over the plains of Kazakhstan (Fig. 7).

Thus, during the cold season of 2019/2020 at three key points located in neighboring glaciological regions and in the zone of their contact, the main areas, from which pollen grains were brought and deposited with snowfalls were identified: the plains of Kazakhstan, the mountainous territories of Altai, and the Middle Ob Lowland. The Kazakh Uplands became the common source for the entry of wormwood pollen (*Artemisia* sp.) with air masses that caused snowfall at all the three points in December 2019.

Tree pollen (*Betula* sp., *Pinus* sp.) identified in the snow was brought in with air masses predominantly formed over snow-free slopes of the Altai Mountains and the Middle Ob Lowland. Pollen of Asteraceae family deposited with snowfall at KP 1 was brought from the snow-free plains of Kazakhstan; at KP 2, from the Altai Mountains; and at KP 3, from the Middle Ob Lowland. Pollen grains of the Amaranthaceae s.l. (incl. Chenopodiaceae) and Poaceae families identified in snow samples from KP 2 were also brought from the snow-free plains of Kazakhstan. These areas also served as the source of pollen of the Asteraceae and Fabaceae families deposited with snow at KP 1.

## CONCLUSIONS

1. Microscopic analysis of 118 snow samples taken immediately after snowfalls during the cold season of 2019/2020 in the Altai–Sayan and Tobol–Irtysh glaciological regions and in the zone of their contact showed the presence of pollen grains of trees (*Betula* sp., *Pinus* sp.) and herbs (*Artemisia* sp., families Asteraceae, Amaranthaceae s.l. (incl. Chenopodiaceae), Fabaceae and Poaceae) in 38% of the samples. The greatest contribution (57%) to the total pollen spec-

trum was made by trees, in particular, the pollen of *Pinus* sp. (32%) and *Betula* sp. (24%); among herbs, by the pollen of Asteraceae (21%) and Amaranthaceae s.l. (incl. Chenopodiaceae) (17%) families, while the contribution of the pollen of *Artemisia* sp., families Poaceae and Fabaceae did not exceed 7%.

2. In the pollen spectrum of snow sampled in the Altai–Sayan glaciological region, tree pollen significantly dominated (67%); in the pollen spectrum of snow samples at the contact zone between the two glaciological regions, the contribution of tree pollen was lower (up to 55%); pollen of herbs predominated in the pollen spectrum of snow samples from the Tobol–Irtysh glaciological region (51%). These differences can be largely due to the fact that the selected key points were found characterized neighboring glaciological regions belonging to different glaciological provinces.

3. The applied approach made it possible to determine the territories from which pollen grains came with snow to neighboring units of glaciological zoning (provinces and regions). It consisted of the event-based sampling of precipitation, microscopic analysis of the samples, construction of reverse trajectories of air masses (HYSPLIT) with due account for the height of the ABL, analysis of the maps of snow and ice cover, as well as the maps of distribution ranges of identified vegetation taxa.

4. The main source of pollen grains of *Artemisia* sp. in the snow precipitated in neighboring glaciological regions and in the zone of their contact in December 2019 became the Kazakh Uplands. This gives grounds to further use the pollen grains of this taxon as indicators of atmospheric transport and deposition with snowfalls in the Altai–Sayan and Tobol–Irtysh glaciological regions of not only pollen but also other particles of natural and anthropogenic origin during the cold season.

5. Territories from which pollen grains of the Amaranthaceae s.l. (incl. Chenopodiaceae) family were brought differed at the three key points. Thus, at KP 3 in the contact zone of the two glaciological regions, they came from both the plains of Kazakhstan (North Kazakh and Turan plains) and from the Middle Ob Lowland, as well as from the snow-free slopes of the Altai Mountains. In this regard, when using these pollen grains as markers of atmospheric processes of the cold season in the Altai–Sayan and Tobol–Irtysh glaciological regions, it is necessary to take into account the results obtained for each of the hierarchical units of the glaciological zoning.

6. Pollen grains of the family Fabaceae were identified only in the snow of the Altai–Sayan glaciological region, while pollen grains of the family Poaceae were found only in the snow of the Tobol–Irtysh glaciological region. However, pollen grains of both taxa were not found in the contact zone of these glaciological regions. This gives reason to consider the possibility of using pollen grains of each of these taxa to assess the pathways of air masses only for the glaciological region, where they were identified in the snow.

***Acknowledgments***. *This study was supported by the Russian Foundation for Basic Research, project nos. 19-35-90078 (sampling and microscopic analysis) and 19-05-50055 (trajectory analysis). The synoptic analysis was performed within the framework of state assignment FUFZ-2021-0007.*

## References

Abakumov V.A. et al., 1992. *Guidelines for Hydrobiological Monitoring of Freshwater Ecosystems*. Sankt-Peterburg, Gidrometeoizdat, 318 p. (in Russian).

Bourgeois J.C., 2000. Seasonal and interannual pollen variability in snow layers of Arctic ice caps. *Rev. Palaeobot. Palynol.* **108** (1–2), 17–36. DOI: 10.1016/S0034-6667(99)00031-7.

Brugger S., Gobet E., Sigl M. et al., 2018. Ice records provide new insights into climatic vulnerability of Central Asian forest and steppe communities. *Glob. Planet. Change* **169**, 188–201. DOI: 10.1016/j.gloplacha.2018.07.010.

Brunet Y., Wery N., Gales A., 2017. Short-scale transport of bioaerosols. In: A.M. Delort, P. Amato (eds.). *Microbiology of Aerosols*. Wiley–Blackwell, p. 137–154.

Dzyuba O.F., 2005. Atlas of pollen grains (non-acetolyzed and acetolyzed), most common in the air basin of Eastern Europe. Moscow, IGIRGI, 70 p. (in Russian).

Festi D., Carturan L., Kofler W. et al., 2017. Linking pollen deposition and snow accumulation on the Alto dell 'Ortles glacier (South Tyrol, Italy) for sub-seasonal dating of a firn temperate core. *The Cryosphere* **111**, 937–948, DOI: 10.5194/tc-11-937-2017.

Fröhlich-Nowoisky J., Kampf C.J., Weber B. et al., 2016. Bioaerosols in the Earth system: climate, health, and ecosystem interactions. *Atmos. Res.* **182**, 346–376. DOI: 10.1016/j.atmosres.2016.07.018.

Golovko V.V., 2004. *Ecological Aspects of Aeropalynology: An Analytical Review*. Novosibirsk, GPNTB, 107 p. (in Russian).

Hernandez-Ceballos M.A., Skjoth C.A., Garcia-Mozo H. et al., 2014. Improvement in the accuracy of back trajectories using WRF to identify pollen sources in southern Iberian Peninsula. *Int. J. Biometeorol.* **58** (10), 2031–2043. DOI: 10.1007/s00484-014-0804-x.

IPCC, 2019. *Summary for Policymakers*. In: *IPCC Special Report on the Ocean and Cryosphere in a Changing Climate* [H.-O. Pörtner, D.C. Roberts, V. Masson-Delmotte, P. Zhai, M. Tignor, E. Poloczanska, K. Mintenbeck, A. Alegría, M. Nicolai, A. Okem, J. Petzold, B. Rama, N.M. Weyer (eds.)].

Ivlev L.S., 1999. *Physics of Atmospheric Aerosol Systems*. Sankt-Peterburg, NIIH SPbGU, 194 p. (in Russian).

Karpovich I.V., Drebezgina E.S., Elovikova E.N. et al., 2015. *Pollen Atlas*. Ekaterinburg, Ural'skii rabochii, 318 p. (in Russian).

Kasprzyk I., Borycka K., 2019. Alder pollen concentrations in the air during snowfall. *Int. J. Biometeorol.* **63**, 1–8. DOI: 10.1007/s00484-019-01781-3.

Kharlamova N.F., 2013. *Climate of the Altai Region*. Barnaul, Publ. House of the Altai Univ., 108 p. (in Russian).

Kotlyakov V.M. (ed.), 1997. *The World Atlas of Snow and Ice Resources*. Moscow, Izd. Ross. Akad. Nauk, 392 p. (in Russian).

Kotlyakov V.M., 2004. *Selected Works. Book 2. Snow Cover and Glaciers of the Earth*. Moscow, Nauka, 448 p. (in Russian).

Kotlyakov V.M., Alekseev V.R., Volkov N.V. et al., 1984. *Glaciological Dictionary*. Leningrad, Gidrometeoizdat, 564 p. (in Russian).

Kupriyanova L.A., Aleshina L.A., 1972. *Pollen and Plant Spores of the Flora of the USSR*. Leningrad, Nauka, 171 p. (in Russian).

Kupriyanova L.A., Aleshina L.A., 1978. *Pollen and Spores of Dicotyledonous Plants of the Flora of the European Part of the USSR*. Leningrad, Nauka, 174 p. (in Russian).

*Landscape map of the Altai Territory*, 2016. IWEP SO RAN, 2 sheets (in Russian).

Malygina N.S., Zinchenko G.S., Ryabchinskaya N.A., Mitrofanova E.Yu., 2018. Sources of biological aerosols in winter precipitation in the south of Western Siberia. *Russian Meteorol. Hydrol.* **43** (4), 264–270. DOI: 10.3103/S1068373918040088.

Papina T., Blyakharchuk T., Eichler A. et al., 2013. Biological proxies recorded in a Belukha ice core, Russian Altai. *Climate of the Past* **9** (5), 2399–2411. DOI: 10.5194/cpd-9-2589-2013.

Polyakov P.P., 1961. Wormwood – *Artemisia* L. genus. In: *Flora of the USSR*. Moscow, Nauka, p. 425–631 (in Russian).

Semenchenko B.A., 2002. *Physical Meteorology*. Moscow, Aspekt Press, 417 p. (in Russian).

Vinokurov Yu.I., Tsimbaley Yu.M., 2016. *Landscape Indication in Ecological and Geographical Research*. Novosibirsk, Publ. House Geo, 258 p. (in Russian).

URL: http://www.aari.ru/ (last visited: Oct. 12, 2020).

URL: http://www.euforgen.org/ (last visited: Oct. 12, 2020).

URL: https://pollenatlas.net/homepage (last visited: Oct. 12, 2020).

URL: https://www.esrl.noaa.gov/psd/data (last visited: Oct. 12, 2020).

URL: https://www.ncei.noaa.gov/products (last visited: Mar. 4, 2021).

URL: https://www.natice.noaa.gov/pub/ims/ims_v3/ims_gif/ARCHIVE/EuAsia/2019/ (last visited: Oct. 12, 2020).

URL: https://www.paldat.org/search/A (last visited: Oct. 12, 2020).

URL: https://www.ready.noaa.gov/HYSPLIT.php (last visited: Oct. 12, 2020).

URL: https://www.ecmwf.int/en/forecasts/datasets/reanalysis-datasets/era5 (last visited: Oct. 12, 2020).

*Received January 20, 2021*
*Revised February 7, 2022*
*Accepted November 14, 2022*

*Translated by A.V. Muravyov*

**EARTH'S CRYOSPHERE**
SCIENTIFIC JOURNAL

*Earth's Cryosphere*, 2022, vol. XXVI, No. 6, pp. 13–20

*GEOTHERMAL FIELDS AND THERMAL PROCESSES IN CRYOSPHERE*

# A METHOD FOR EVALUATING THE THERMOPHYSICAL PROPERTIES OF SEASONALLY FREEZING AND SEASONALLY THAWING SOILS UNDER NATURAL CONDITIONS

**V.E. Ostroumov[1,*], D.G. Fedorov-Davydov[1], I.A. Komarov[2], F.A. Shevchik[2], A.M. Koloskov[2], M.P. Volokitin[3], V.V. Goncharov[1], S.S. Bykhovets[1], V.P. Shabaev[1], A.L. Kholodov[1,4], I.I. Eremin[5], D.Yu. Kropachev[5], S.P. Davydov[6], A.I. Davydova[6]**

[1] *Institute of Physicochemical and Biological Problems of Soil Science, Russian Academy of Sciences, Institutskaya St. 2, Pushchino, 142290 Russia*
[2] *Lomonosov Moscow State University, Faculty of Geology, Department of Geocryology, Leninskie Gory 1, Moscow, 119991 Russia*
[3] *Institute of Fundamental Problems of Biology, Russian Academy of Sciences, Institutskaya St. 2, Pushchino, 142290 Russia*
[4] *University of Alaska, Geophysical Institute, 2156 Koyukuk Drive, Fairbanks, Alaska, USA*
[5] *JSC SPA Etalon, Lermontov St. 175, Omsk, 644009 Russia*
[6] *Pacific Geographical Institute, Far Eastern Branch of the Russian Academy of Sciences, North-East Scientific Station, Chersky 18, Sakha (Yakutia), 678830 Russia*

**Corresponding author; e-mail: v.ostroumov@rambler.ru*

Under natural conditions, seasonally freezing and seasonally thawing soils are open systems of variable composition, structure, and properties. However, in engineering projects, to describe their thermal state, the values of thermal properties measured in laboratory on isolated samples of constant composition are used. To take into account the variability of the thermal properties of active layer soils under the influence of external factors, we propose a method for assessing the equivalent indicators of their volumetric heat capacity and thermal conductivity using a combined analysis of dynamics of the temperature and heat flow in soils based on long-term monitoring data. Monitoring of heat flow density and soil temperature is carried out in two areas, one of which characterizes the area of seasonal freezing, the second – the area of seasonal thawing of soils. A method has been developed for calculating the effective coefficients of thermal conductivity and heat capacity from monitoring data on temperature and heat flow in soils. A procedure for processing monitoring data is proposed, which makes it possible to determine the time-averaged effective values of the thermal conductivity coefficients and the heat capacity. The developed technique makes it possible to observe fluctuations in the coefficients of thermal conductivity and heat capacity in time series against the background of changes in the composition and external factors of heat transfer in seasonally freezing and seasonally thawing soils under natural conditions.

***Keywords:*** *permafrost, soils, active layer, thermophysical properties, heat flow, temperature regime, geocryological monitoring.*

***Recommended citation:*** Ostroumov V.E., Fedorov-Davydov D.G., Komarov I.A., Shevchik F.A., Koloskov A.M., Volokitin M.P., Goncharov V.V., Bykhovets S.S., Shabaev V.P., Kholodov A.L., Eremin I.I., Kropachev D.Yu., Davydov S.P., Davydova A.I., 2022. A method for evaluating the thermophysical properties of seasonally freezing and seasonally thawing soils under natural conditions. *Earth's Cryosphere* **26** (6), 13–20.

## INTRODUCTION

In the areas of distribution of seasonally frozen and seasonally thawed soils and rocks, their thermal state largely determines the choice of the method of construction of engineering facilities, the type of foundations, and their operation. In particular, the prediction of the depths of the seasonally frozen (SFL) and seasonally thawed (STL) soil layers in engineering practice is performed by solving the boundary value problem of heat conduction with an explicit separation of the front, as well as approximate analytical problems in an explicit or implicit form (transcendental, integral relations brought using library algorithms). In regulatory documents, the thickness of SFL and STL is estimated by the values of the normative freezing–thawing depths or calculated by modifications of the Stefan formula [*Bases and foundations..., 2012*]. The hydrophysical properties of dispersed rocks and soils (natural and characteristic moisture), density, thermal conductivity coefficient, heat capacity, freezing point, and phase composition of water used in the calculations are determined either in laboratory conditions on samples of dis-

turbed or undisturbed composition, or in field conditions on the basis of a one-time testing.

However, under natural conditions, the properties of soils and rocks of SFL and STL are very dynamic due to changes in the content and phase state of water. Along with conductive heat transfer characterized by the coefficient of thermal conductivity, convective heat and water transfer occurs in soils (infiltration of free water, migration of unfrozen water in the freezing zone to the freezing front, diffusion of water vapor and gases, and other processes). Important factors controlling the thermophysical properties of dispersed rocks and soils, their composition and density, change under natural conditions as a result of shrinkage, swelling, and heaving of soils and other processes associated with the restructuring of structural bonds. In addition, mass transfer in soils induces various exothermic and endothermic processes (condensation and evaporation of liquid water in soil, sublimation–desublimation of ice, chemical and biochemical transformations), which contribute to the heat balance of SFL and STL, along with the processes of water freezing or ice melting in pores [*Ivanov, 1969; Buldovich et al., 1978; Komarov, 2003; Zhirkov et al., 2018*]. Forecasting the depth of seasonal freezing and thawing of soils without taking into account these thermal effects can lead to significant errors. The influence of the variability of the listed factors on the effective values of the thermophysical properties of soils SFL and STL remains insufficiently studied.

The purpose of this work is to develop a methodology that allows, based on field measurements of the heat flow density ($B$) and temperature ($T$) of soils, to estimate the effective values of their volumetric heat capacity ($C_e$) and thermal conductivity coefficient ($\lambda_e$), which change in time series against the background of external heat transfer factors in the seasonally freezing and seasonally thawing soils.

## OBJECTS OF STUDY

The soils of two sites with different geocryological conditions were studied.

*The first site of field observations* (Pushchino site) characterizes soils in the area of seasonal freezing. The site is located in the center of the Russian Plain in the Zaokskaya part of Serpukhov district of the Moscow region on the southern outskirts of Pushchino. The studied gray forest soils are formed on the cover loam. Their bulk density is 1.49–1.54 g/cm$^3$, and their water content is usually about 24–25% of the field water capacity. The grassy ground cover on the site is continuous, there is no woody vegetation. The climate of the region is temperate continental with moderately cold winters, warm summers and stable moisture. The monitoring area is located on a horizontal surface. There is a permanent observation post of integrated environmental monitoring program of the Institute of Physicochemical and Biological Problems of Soil Science RAS on it.

The mean annual temperature of rocks in the Pushchino area is +6.0°C. Soil freezing begins in early November, seasonal frost persists until mid-late March. According to the results of field observations in winter season of 2014/2015, the maximum freezing depth in the area ranged from 0.1 to 0.3 m. In the seasonally frozen soil layer, segregated ice formation was observed, which was accompanied by heaving and compaction of mineral interlayers. In the summer, the processes of soil drying and structuring take place, which leads to soil decompaction and an increase in its permeability for liquid and gaseous components. This, in turn, contributes to both subsoil and surface evaporation of water.

*The second area* of of *field observations* – Chersky site – belongs to the zone of seasonal thawing of permafrost-affected soils. The site is located in the subarctic zone on the right bank of the Kolyma River in its lower reaches (northeast of the Republic of Sakha (Yakutia)), on the southern outskirts of the village of Chersky. Here, ice-rich silty loams of the Late Pleistocene age with thick ice wedges occur from the surface; they are attributed to the yedoma suite [*Decisions..., 1987; Schirrmeister et al., 2013; Vasilchuk, Budantseva, 2018*].

The point of heat flow and temperature measurements of STL rocks is located on a gentle slope (4–5°) of southern exposure, in a lichen-cowberry-green moss larch woodland with cryometamorphic pale soil. The peaty material on the soil surface has a thickness of up to 5 cm. The soil and underlying rocks are characterized by a high (2–14%) content of organic matter represented mainly by weakly decomposed plant residues (detritus) heterogeneously distributed along the profile. At the site, long-term observations are carried out by the Northeastern Scientific Station of the Pacific Institute of Geography, Far Eastern Branch of the Russian Academy of Sciences under a comprehensive monitoring program, which includes meteorological, geocryological, geobotanical, and other works.

The climate of the region is sharply continental with a long cold winter period. The soil bulk density is 1.4 g/cm$^3$. Usually, the soil is moistened to total water capacity; however, in summer, with prolonged droughts in the upper horizons, a decrease in the weight water content to 5–7% is observed. The mean annual rock temperature a depth of zero annual amplitudes in 2022 was –2.6°C. Seasonal soil thawing at the Chersky site begins in mid-late May. About 80% of the STL thaws in June–July. In the first half of September, soil thawing practically stops. Complete freezing of the thawed layer usually occurs by mid-January. According to long-term (1998–2020) observations (point R18 “Mountain Rodinka” of the inter-

national CALM program), the average thickness of the layer of seasonal soil thawing is 81 cm. At the point of heat flow measurement, this value is equal to 85 cm. At the monitoring site of soil temperature and heat flow, freezing of the STL is accompanied by heaving and cryogenic cracking. These processes contribute to the development of sublimation drying of the soil in winter. Since the site is located on a slope and is moistened, in the summer, suprapermafrost runoff is formed in the soil in some places, which affects the thermal state of the soil and underlying permafrost.

## THE METHOD OF MEASURING HEAT FLOW AND SOIL TEMPERATURE IN THE FIELD CONDITIONS AND DETERMINATION OF THEIR THERMOPHYSICAL PROPERTIES IN A LABORATORY

Soil temperature measurements were carried out according to the methodology provided for by [*Guidelines..., 1980*] in an automated mode using semiconductor sensors instead of mercury thermometers. At the Pushchino site, soil temperature monitoring was carried out using a measuring complex UGT DL-200 (Germany), which, based on a logger, combines the sensors of the meteorological station complex and soil temperature. Soil temperature sensors of the UGT system were installed at depths of 0, 10, 40, and 80 cm. At both sites, the boundary between live and dead vegetation was taken as the zero depth. Each sensor was placed in an uncased borehole filled with local soil after installation of the sensors. To reduce the mutual influence, the boreholes were spaced apart at a distance of 0.5 m from one another in accordance with the regulatory requirements [*Guidelines..., 1980*]. The measurements were carried out every minute, and the average values were recorded in the logger's memory every 15 minutes.

At the Chersky site, soil temperature measurements were carried out using MCDT sensors connected to an LCD-1/100-SC logger manufactured by SPA "Etalon" (Omsk). They were laid at depths of 0, 20, 40, and 80 cm. The sensors, assembled in the form of a thermo-braid, were installed in a well without casing filled with local soil material after installation; the ground cover was also placed back. The interval between soil temperature measurements was 2 h. At both sites, the equipment used provided soil temperature measurements with a sensitivity no worse than 0.05°C.

Heat flow measurements in the soil at the first and second sites were carried out using heat flow density sensors DTP-0924 and data loggers LCD-1/100-SC manufactured by SPA "Etalon". The sensors in the form of discs 100 mm in diameter and 7 mm thick together with the LCD-1/100-SC logger provide a heat flow sensitivity of 0.4 W/m$^2$. Heat flow sensors were installed in the soil in the wall of the pit. During installation, the distance between the sensors in the plan was 0.5 m. For each sensor, a niche was arranged in the wall of the pit in the form of a horizontal slot about 30 cm long and 2.0–2.5 cm high. in which the sensor was placed. Then the space above the sensor and the entire cavity in the wall of the pit were filled with the same suspension, and the soil removed from the pit was put back into place in layers. At the Pushchino site, heat flow sensors were installed at depths of 5, 20, and 45 cm; at the Chersky site, at depths of 5, 40, and 65 cm. The interval between measurements of the heat flow density at all depths was 1 h.

The effective values of thermal conductivity coefficients $\lambda_e$ and heat capacity $C_e$ of soils determined from the data of heat flow and temperature monitoring were compared with the values of thermal conductivity coefficients $\lambda$ and heat capacity $C$ measured under laboratory conditions. Laboratory measurements were performed on soil samples taken at the Pushchino monitoring site. To assess the effect of soil moisture on their thermophysical properties, samples of disturbed structure (paste) with a given moisture content were studied. Measurements of $C$ and $\lambda$ in the laboratory were carried out using a constant power cylindrical probe using a KD2 Thermal Properties Analyzer (Decagon Devices, USA).

## DATA PROCESSING

To determine the effective value of the thermal conductivity coefficient $\lambda_e$ [W/(m·K)] according to the measured values of temperature and heat flow density, the formula was used

$$\lambda_e = |B_1|(H_1 - H_2)/(T_1 - T_2), \quad (1)$$

where: $|B_1|$ is the modulus of heat flow density, W/m$^2$; $(H_1 - H_2)$ is the depth difference (m) between heat flow sensors 1 and 2; and $(T_1 - T_2)$ is the difference in average soil temperatures (K) at depths $(H_1 - H_2)$.

The effective value of the soil volumetric heat capacity $C_e$ (J/(m$^3$·K)) was calculated by the formula

$$C_e = \frac{(B_1 - B_2)\tau}{(H_1 - H_2)(T_3 - T_2)}, \quad (2)$$

where $(B_1 - B_2)$ is the difference in heat flow density between sensors 1 and 2, W/m$^2$; $\tau$ is the time interval between measurements, s; $(H_1 - H_2)$ is the depth difference between heat flow sensors 1 and 2, m; $(T_3 - T_2)$ is the difference in soil temperature (K) between the next and current measurements.

Formulas (1) and (2) are valid for the linear distribution of soil temperature over depth and over time. Therefore, when estimating the values of $C_e$ and $\lambda_e$ with their help, fragments of soil temperature series were used as initial data, in which its values at

the boundaries of the calculated soil blocks remained constant within the allowable accuracy of thermometry (0.1 K). Additional possibilities for obtaining data are provided by averaging the values of $\lambda_e$ and $C_e$ in fragments of the time sequence of the values of the heat flow and soil temperature. The average values of effective thermal conductivity $\left(\lambda_e^m\right)$ and heat capacity $\left(C_e^m\right)$ are calculated using the following formulas (3) and (4):

$$\lambda_e^m = \frac{n}{n-1}\left[\sum_{i=1}^{n-1} B_i \Big/ \sum_{\gamma=1}^{n} \frac{\Delta T_\gamma}{\Delta H_\gamma}\right], \qquad (3)$$

where $n - 1$ is the number of heat flow sensors in the first and second selected layers; $n$ is the number of temperature sensors; $\gamma$ is the number of measurements of the temperature gradient; $i$ is the number of heat flow measurements; $B_i$ is the current value of the heat flow density; $\Delta T_\gamma$ is the current value of soil temperature; and $\Delta H_\gamma$ is the current value of the sensor location depth;

$$C_e^m = \frac{1}{n}\sum_{i=1}^{n} \frac{\left(B_i + B_{i-1}\right)\tau_i}{2\Delta H \Delta T_\tau}, \qquad (4)$$

where $n$ is the number of heat flow measurements; $B_i$ is the current value of the heat flow intensity; $B_{i-1}$ is the previous value of the intensity of the heat flow; $\tau_i$ is the time between measurements; $\Delta T_\tau$ is the current temperature value; and $\Delta H$ is the current value of the sensor location depth.

The normality of the distribution of the obtained values was assessed by the Pearson criterion. The data, for which the following condition was fulfilled, were discarded:

$$\left|\overline{a} - x_i\right| > \nu S,$$

$$\overline{a} = \frac{1}{n}\sum_{i=1}^{n} x_i,$$

$$S = \sqrt{\frac{1}{n-1}\sum_{i=1}^{n}\left(\overline{a} - x_i\right)^2},$$

where $\nu$ is a statistical criterion adopted depending on the number of values; $S$ is the standard deviation; $\overline{a}$ is the average statistical value for each month; $n$ is the number of characteristic values; and $x_i$ is a particular value of the characteristic.

The values of $C_e$ and $\lambda_e$ obtained under the conditions $\left|T_i - T_{i+1}\right| < s_T$, $\left|B_i\right| < s_B$, $\left|B_i - B_{i+1}\right| < s_B$, where $s_T$, $s_B$ are the sensitivity of the temperature and heat flow meters, respectively, were also excluded from consideration.

The processing of the values $\lambda_e^m$ and $C_e^m$ obtained by formulas (3) and (4) showed that they fit into the confidence interval $\overline{a} \pm S$, which makes it possible to use averaged data in calculations.

## EXAMPLES OF PROCESSING MONITORING DATA AND DISCUSSION OF THE RESULTS

Figures 1 and 2 show examples of the results of monitoring temperature $T$ and heat flow density $B$ in soils for both study areas. With increasing depth, there is a regular decrease in the amplitude of fluctuations in both temperature and heat flow density, as

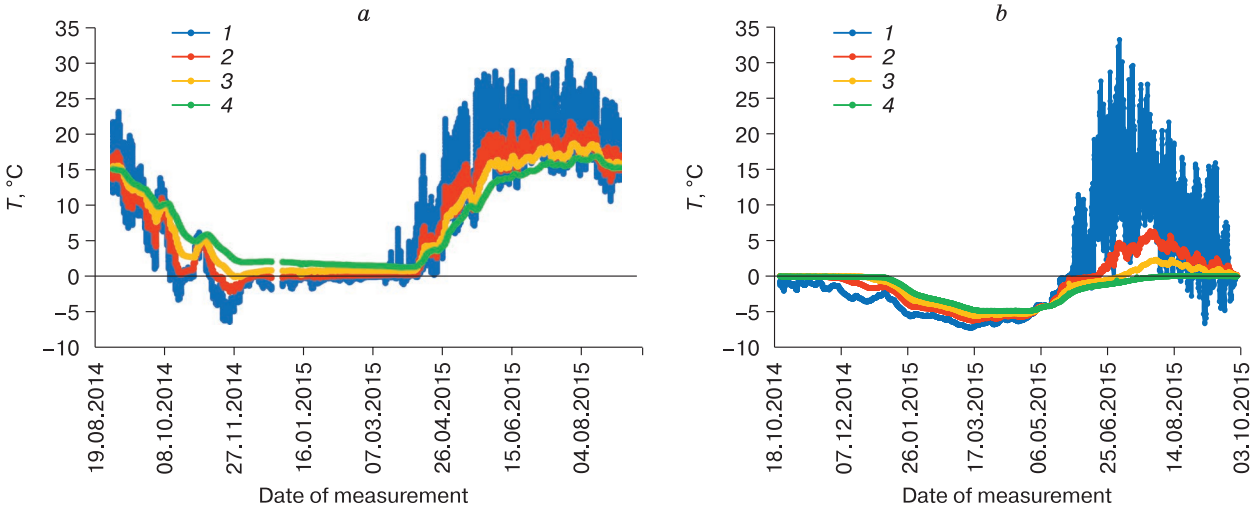


**Fig. 1. Dynamics of soil temperature ($T$) at different depths ($H$):**

($a$) soil of the seasonally frozen layer, Pushchino site, September 2014–September 2015; depths (*1*) 0, (*2*) 0.1, (*3*) 0.4, and (*4*) 0.8 m; ($b$) soil of the seasonally thawed layer, Chersky site, October 2014–September 2015; depths (*1*) 0, (*2*) 0.1, (*3*) 0.4, and (*4*) 0.8 m. The dates of measurements are indicated on the horizontal axis in the format day/month/year.

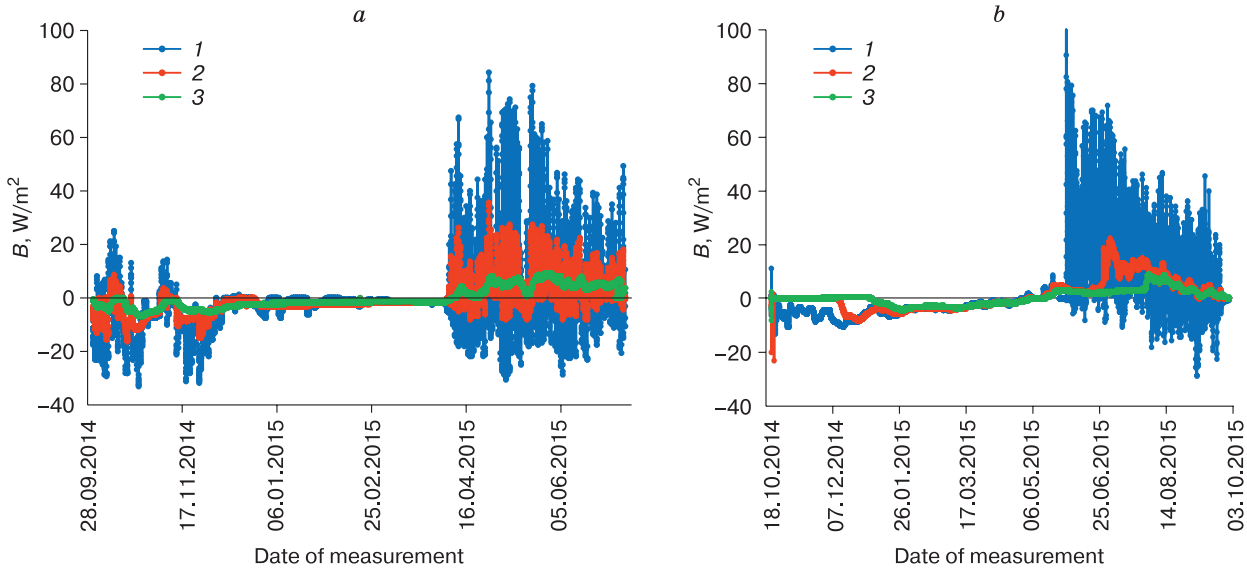


**Fig. 2. Dynamics of heat flow density ($B$) in soils at different depths ($H$):**

($a$) soil of the seasonally frozen layer, Pushchino site, September 2014–September 2015; depths (*1*) 0.05, (*2*) 0.20, and (*3*) 0.45 m; ($b$) soil of the seasonally thawed layer, Chersky site, October 2014–September 2015; depths (*1*) 0.05, (*2*) 0.40, and (*3*) 0.65 m.

well as an increase in the phase shift in daily and annual cycles. The dynamics of the indicators under consideration differ significantly in the snowless period and in the presence of snow cover. In both areas, diurnal temperature fluctuations, as a rule, do not penetrate through the snow mass.

Based on the results of monitoring the heat flow and soil temperature within the time series with heat transfer under quasistationary conditions at both monitoring sites, using formulas (1), (2), the effective values of the heat capacity and thermal conductivity of soils $C_e$ and $\lambda_e$ were calculated.

For the SFL of the Pushchino site (Fig. 3), the lowest $C_e$ values of about 1 MJ/(m$^3$·K) are observed in summer and mid-December 2014 in the upper (5–20 cm) soil layer. These relatively low effective $C_e$ values are close to the heat capacity values measured under laboratory conditions $C$, which increase with soil moisture from 1.2 to 3.2 MJ/(m$^3$·K). In other cases, the effective $C_e$ values turned out to be greater than the heat capacity values measured in the laboratory, reaching 7 MJ/(m$^3$·K). The observed excess of $C_e$ over $C$ in the upper horizon, which experiences freezing and thawing in winter, is explained by the

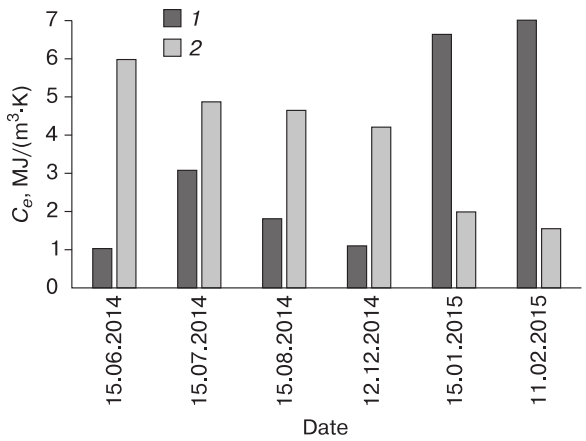


**Fig. 3. Effective values of soil heat capacity ($C_e$) at depths of (*1*) 5–20 cm and (*2*) 20–45 cm calculated using formula (2) according to monitoring data on heat flow and rock temperature at the Pushchino site.**

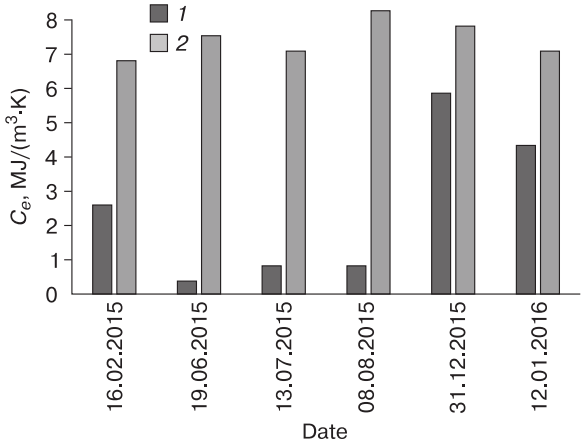


**Fig. 4. Effective values of soil heat capacity ($C_e$) at depths of (*1*) 0–40 cm and (*2*) 40–85 cm, calculated by formula (2) according to monitoring data of heat flow and soil temperature at the Chersky site.**

contribution of the heat of water phase transitions to the effective heat capacity of the soil. The high $C_e$ values observed in summer can be explained by their dependence on heat consumption during water evaporation from the soil surface.

A similar picture is observed in the dynamics of the heat capacity of seasonally thawing soil (Fig. 4). Here, the values of the effective heat capacity in the lower layer (40–85 cm) are noticeably higher than those near the surface (0–40 cm). Freezing of the soil in the surface layer at the beginning of winter is accompanied by an increase in the effective heat capacity, which is obviously related to the contribution of the heat of ice formation to $C_e$. The lowest $C_e$ values in the upper part of the STL at the beginning and end of summer can be explained by a seasonal decrease in soil moisture.

Figure 5 shows the dynamics of the effective values of the thermal conductivity coefficient $\lambda_e$ of seasonally freezing soil. The variability of $\lambda_e$ observed here from 0.3 to 2.2 W/(m·K) exceeds the range of values associated solely with conductive transfer (values of $\lambda$ measured in the laboratory vary from 0.13 to 1.79 W/(m·K)). Fluctuations in $\lambda_e$ are explained by the processes of convective transfer during infiltration of surface waters and during the transfer of the gas phase in the soil. The contribution of exo- and endothermic processes affecting the $C_e$ value in soils to the $\lambda_e$ values, cannot be excluded.

The values of $\lambda_e$ for the seasonally thawing soil of the Chersky site are even more variable (Fig. 6). The lowest effective values of thermal conductivity were noted in the layers at the depths of 20–40 and 80–85 cm in summer. Such dynamics of $\lambda_e$ is explained by the contribution of convective processes to heat transfer, as well as by the influence of exo- and endothermic transformations in soils under natural conditions.

For an approximate estimate of the possible contribution of the heat of evaporation to the effective values of the coefficients of thermal conductivity and heat capacity, we use formulas (1) and (2), replacing the measured $B_1$ values in them with the value of the intensity of the flow spent on the evaporation of water from the soil surface. A.R. Konstantinov [*1968*] gives data on evaporation from the soil surface for June (the month with the most intense evaporation) of 27.7 kg/(m$^2$·month) in the forests of the center of the Central Russian Upland (Moscow as the nearest station to the Pushchino site) and 21.6 kg/(m$^2$·month) for the Kolyma Lowland (Srednekolymsk as the nearest station to the Chersky site). Taking into account the specific heat of water evaporation equal to 2.4 MJ/kg, according to formulas (1) and (2), we find that the contribution of heat consumption for water evaporation to the effective values of the thermal conductivity coefficient is 1.2 and 1.9 W/(m·K) at the Pushchino and Chersky sites, respectively. The contributions of heat costs for water evaporation to the effective values of soil heat capacity calculated by formula (2) with the same replacement are 0.56 and 0.35 MJ/(m$^3$·K) for the Pushchino and Chersky sites. Therefore, the heat consumption for the evaporation of water from the soil can make a significant contribution to the observed excesses of $\lambda_e$ and $C_e$ over $\lambda$ and $C$.

Along with the evaporation of water, the values of $\lambda_e$ and $C_e$ are significantly affected by the processes of ice sublimation, convection of liquid and gaseous soil components, oxidation of organic matter, and other exo- and endothermic reactions. The study of the influence of these processes requires the involve-

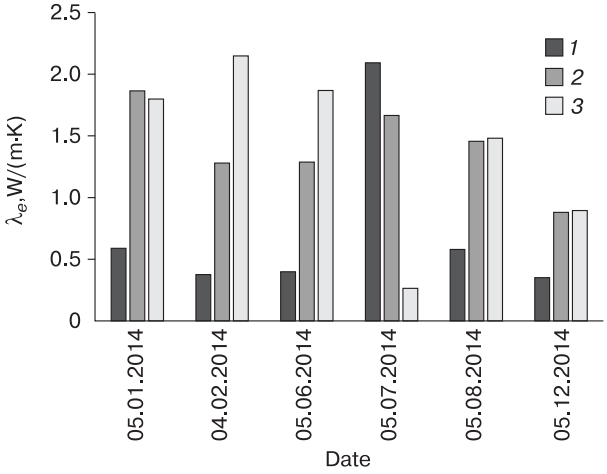


**Fig. 5. Effective values of the thermal conductivity coefficient ($\lambda_e$) of the soil (Pushchino site) at depths of (*1*) 0–10 cm, (*2*) 10–40 cm, and (*3*) 40–80 cm calculated by formula (1).**

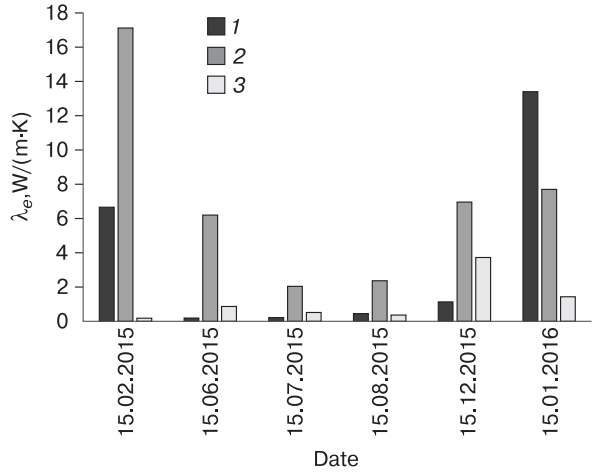


**Fig. 6. Effective values of the thermal conductivity coefficient ($\lambda_e$) of seasonally thawing soil (Chersky site) at depths of (*1*) 20–40 cm, (*2*) 40–80 cm, and (*3*) 80–85 cm calculated by formula (1).**

ment of additional data on the moisture regime, mass transfer in soils, emission of gaseous phases, etc.

The variability of the effective thermophysical coefficients is also characteristic of the monthly averages $\lambda_e^m$ and $C_e^m$ (Table 1). At the Pushchino site, the lowest values $\lambda_e^m$ are observed in winter and in the middle of summer in the upper part of the soil profile, when soil moisture is minimal and water phase transitions do not occur in it. The highest values of $\lambda_e$ are observed at the end of spring, which is probably caused by water evaporation. The lowest value of the effective heat capacity of the soil at the Pushchino site is observed in spring after thawing, and the highest value is observed at the beginning of winter, which may be due to the contribution of the heat of the phase transition of water during soil freezing.

At the Chersky site, the lowest effective values of the thermal conductivity of the soil are confined to the middle of summer and the middle of winter, when the intensity of phase transitions of water in the soil is minimal. The highest value of $\lambda_e$ was recorded in April during soil thawing. The lowest $C_e$ values are also noted here in summer and winter, but it is in summer that the maximum $C_e$ value occurs, which can be explained by the effect of water evaporation from the soil. The distribution in the soil profile and the dynamics of the effective values of thermophysical parameters in both areas are complex, and additional data are needed for their analysis.

Table 1. **Averaged values of effective coefficients of thermal conductivity (3) and heat capacity (4) of soils at different depths in summer and winter periods**

| Month, year | $\lambda_e^m$, W/(m·K) | | | $C_e^m$, MJ/(m$^3$·K) | |
|---|---|---|---|---|---|
| | 0–0.1 m | 0.1–0.4 m | 0.4–0.8 m | 0.05–0.20 m | 0.20–0.45 m |
| *Pushchino site* | | | | | |
| December 2013 | 1.04 ± 0.08 | 1.18 ± 0.06 | 1.00 ± 0.01 | 6.79 ± 0.99 | 4.52 ± 0.68 |
| January 2014 | 0.51 ± 0.07 | 0.77 ± 0.11 | 0.99 ± 0.01 | 6.34 ± 0.96 | 4.67 ± 0.90 |
| February 2014 | 0.33 ± 0.10 | 0.90 ± 0.18 | 0.92 ± 0.02 | – | – |
| April 2014 | 0.47 ± 0.79 | 0.90 ± 0.04 | – | 1.65 ± 0.56 | 3.33 ± 0.07 |
| May 2014 | 0.56 ± 0.71 | 0.87 ± 0.03 | 1.00 ± 0.02 | 3.36 ± 0.45 | 4.02 ± 0.48 |
| June 2014 | 0.35 ± 0.13 | 0.77 ± 0.03 | 0.97 ± 0.05 | – | 2.87 ± 1.98 |
| July 2014 | 0.33 ± 0.02 | 0.53 ± 0.10 | 0.92 ± 0.02 | – | 5.50 ± 0.75 |
| November 2014 | – | – | 0.40 ± 0.09 | – | 3.92 ± 2.34 |
| December 2014 | 0.65 ± 0.34 | 0.73 ± 0.36 | 0.81 ± 0.06 | 5.74 ± 1.89 | – |
| January 2015 | 0.38 ± 0.11 | 1.07 ± 0.18 | 0.67 ± 0.03 | 5.80 ± 2.13 | – |
| February 2015 | – | 0.77 ± 0.04 | 0.74 ± 0.01 | 5.66 ± 2.20 | – |
| March 2015 | 0.37 ± 0.06 | 0.88 ± 0.06 | 0.62 ± 0.02 | 4.01 ± 2.07 | – |
| April 2015 | – | – | 0.92 ± 0.40 | – | 2.96 ± 2.45 |
| May 2015 | 0.55 ± 0.14 | 1.10 ± 0.24 | 1.30 ± 0.24 | 3.60 ± 1.95 | 4.60 ± 1.45 |
| June 2015 | 0.37 ± 0.15 | 0.73 ± 0.16 | 1.25 ± 0.05 | – | – |
| | 0–0.2 m | 0.2–0.4 m | 0.4–0.8 m | 0.05–0.40 m | 0.40–0.65 m |
| *Chersky site* | | | | | |
| December 2014 | 1.30 ± 0.30 | 0.35 ± 0.03 | 1.06 ± 0.03 | 6.12 ± 0.78 | 4.56 ± 0.99 |
| June 2015 | – | 0.28 ± 0.45 | 0.25 ± 0.01 | 4.88 ± 0.29 | 6.84 ± 0.14 |
| October 2015 | 1.11 ± 0.30 | – | – | 6.44 ± 0.56 | – |
| January 2016 | – | 0.28 ± 0.01 | 1.35 ± 2.49 | 0.87 ± 0.01 | 3.13 ± 0.05 |
| May 2016 | – | 4.07 ± 0.02 | 0.30 ± 0.52 | – | 0.96 ± 0.06 |
| June 2016 | 1.27 ± 0.30 | – | 0.21 ± 0.01 | 5.72 ± 0.04 | 7.58 ± 0.14 |
| October 2016 | 1.30 ± 0.30 | – | 0.68 ± 0.05 | 6.12 ± 0.41 | 3.48 ± 0.31 |
| December 2016 | – | 4.84 ± 0.050 | – | 6.65 ± 0.42 | 3.80 ± 0.30 |
| May 2017 | 0.83 ± 1.14 | – | 0.69 ± 0.59 | – | – |
| June 2017 | – | 8.45 ± 4.80 | 0.26 ± 0.01 | 6.56 ± 0.39 | 2.95 ± 0.31 |
| September 2017 | – | 13.38 ± 1.37 | 0.26 ± 0.01 | 6.41 ± 0.39 | 3.00 ± 0.30 |
| October 2017 | 0.79 ± 0.39 | 12.78 ± 3.02 | 0.65 ± 0.69 | 6.40 ± 0.38 | 3.08 ± 0.30 |
| June 2018 | 0.76 ± 0.79 | 7.49 ± 0.23 | 0.27 ± 0.01 | 5.76 ± 0.14 | 3.20 ± 0.31 |
| April 2019 | – | 17.80 ± 0.80 | – | 4.68 ± 0.34 | 4.04 ± 0.30 |
| November 2019 | – | 15.78 ± 0.86 | 8.08 ± 0.77 | – | – |

## CONCLUSIONS

The data of monitoring the heat flow density and soil temperature at two observation sites, which characterize the areas of seasonal freezing and seasonal thawing of soils in natural conditions, are considered. A technique for estimating the effective values of the coefficients of thermal conductivity and heat capacity of soils based on monitoring results is proposed. A procedure has been developed that makes it possible to obtain time-averaged effective values of $C_e$ and $\lambda_e$. For control in the laboratory, on samples with a given water content, $C$ and $\lambda$ were measured by the cylindrical probe method, which determines only the conductive heat transfer. The values of $C$ and $\lambda$ are compared with the effective values of the $C_e$ and $\lambda_e$ coefficients characterizing heat transfer in soils as in open natural systems.

The results show that $C_e$ and $\lambda_e$ do not remain constant under natural conditions, but change significantly with time. The dependence of $C_e$ and $\lambda_e$ on soil moisture only partly explains the observed differences. In autumn and spring, during freezing and thawing of the soil, the effective coefficients $C_e$ and $\lambda_e$ change significantly due to the heat of phase transitions during freezing of water and melting of ice. In summer, the observed anomalously high values of the effective coefficients $C_e$ and $\lambda_e$ are probably associated with heat consumption for water evaporation from the soil. The thermal effects of water freezing and melting, as well as its evaporation, explain the main features of the observed dynamics of $C_e$ and $\lambda_e$. At the same time, to analyze the full picture of changes in these coefficients, additional data on condensation, sublimation, desublimation of water, oxidation of organic matter, changes in soil structure, and other processes are required.

The proposed method for determining the effective values of heat capacity and thermal conductivity ($C_e$ and $\lambda_e$) from temperature and heat flow monitoring data makes it possible to evaluate the thermophysical properties of soils as quantitative values associated not only with the conductive mechanism of heat transfer but also with the probable contribution of processes occurring in seasonally freezing and seasonally thawing soils under natural conditions to heat transfer.

***Acknowledgments.*** *This study was carried out within the framework of state assignments AAAA-A18-121040800142-5 and AAAA-A18-118013190180-9 and supported by the Russian Foundation for Basic Research, project 20-05-00559.*

## References

*Bases and Foundations on Permafrost*, 2012. Set of Rules RS 25.13330.2012. Moscow, FCS, 118 p. (in Russian).

Buldovich S.N., Afanasenko V.E., Melent'ev V.S., 1978. Some data on condensation of water vapor in coarse detrital soils of South Yakutia. In: *Merzlotnye issledovaniya*. Moscow, Mosk. Gos. Univ., vol. 17, p. 169–175 (in Russian).

*Decisions of the Interdepartmental Stratigraphic Meeting of the Quaternary System of the East of the USSR*, 1987. Magadan, SVKNII DVO AN SSSR, 241 p. (in Russian).

*Guidelines for Agrometeorological Posts*, 1980. Leningrad, Gidrometeoizdat, 82 p. (in Russian).

Ivanov N.S., 1969. *Heat and Mass Transfer in Frozen Rocks*. Moscow, Nauka, 240 p. (in Russian).

Komarov I.A., 2003. *Thermodynamics and Heat and Mass Transfer in Dispersed Frozen Rocks*. Moscow, Nauchnyi Mir, 608 p. (in Russian).

Konstantinov A.R., 1968. *Evaporation in Nature*. Leningrad, Gidrometeoizdat, 532 p. (in Russian).

Schirrmeister L., Froese D., Tumskoy V. et al., 2013. Yedoma: Late Pleistocene ice-rich syngenetic permafrost of Beringia. In: *Encyclopedia of Quaternary Science*. Amsterdam, Elsevier, p. 542–552.

Vasilchuk Yu.K., Budantseva N.A., 2018. Stable oxygen isotopes in new sections of the Yedoma and Holocene deposits of the Chersky settlement in the lower reaches of the Kolyma River. *Arktika i Antarktika,* no. 3, 95–106.

Zhirkov A.F., Permyakov P.P., Zheleznyak M.N., 2018. Influence of the water condensation on the thermal and water regime of grounds. *Probl. Region. Ekolog.,* no. 3, 77–89.

*Received October 10, 2021*
*Revised May 8, 2022*
*Accepted October 29, 2022*

*Translated by A.V. Muravyov*

**EARTH'S CRYOSPHERE**
SCIENTIFIC JOURNAL

*Earth's Cryosphere*, 2022, vol. XXVI, No. 6, pp. 21–27

*PERMAFROST ENGINEERING*

# CONSTRUCTION OF BUILDINGS IN THE ARCTIC WITH THE APPLICATION OF GRANULATED FOAM-GLASS CERAMICS IN THEIR BASES

**K.S. Ivanov[1,*], A.A. Melnikova[2]**

[1] *Earth Cryosphere Institute, Tyumen Scientific Center, Siberian Branch of the Russian Academy of Sciences, Malygina St. 86, Tyumen, 625026 Russia*
[2] *Tyumen Industrial University, Faculty of Architecture and Construction, Department of Design of the Architectural Environment, Volodarskogo St. 38, Tyumen, 625000 Russia*

**Corresponding author; e-mail: sillicium@bk.ru*

The construction of heated buildings in the Arctic is considered. To increase the bearing capacity of the foundations via their preservation in the frozen state, an environmentally friendly heat-insulating material obtained from the Arctic raw materials (opal-cristobalite and zeolite rocks) has been proposed. The aim of this work is to evaluate the efficiency of insulation layer made of granular foam-glass ceramic on the basis of numerical modeling of the thermal interaction between the heated building and the frozen base. We have investigated the influence of protective screens, construction parameters of a dome-shaped building, and the thickness of insulation layer on the thermal regime of a frozen base over 30 years in comparison with the option without the use of special engineering measures. Calculations indicate that the safe exploitation of a heated building without traditional seasonal cooling devices and a ventilated underground is only possible with the use of protective screens. The building can have the shape of not only a dome but also an elongated ellipsoid of unlimited length. In this case, for building width of 6–8 m, the thickness of insulation layer should be 1.0–1.4 m. The proposed technology is promising to reduce the cost of low-rise Arctic construction, rational use of mineral resources, and preservation of the permafrost and Arctic landscapes.

***Keywords:*** *Arctic, permafrost, foundations, building construction, heat-insulating material.*

***Recommended citation:*** Ivanov K.S., Melnikova A.A., 2022. Construction of buildings in the Arctic with the application of granulated foam-glass ceramics in their bases. *Earth's Cryosphere* **26** (6), 21–27.

## INTRODUCTION

Natural resources and infrastructure of the Northern Sea Route are among governmental priorities of the future Arctic development [*Fauser, Smirnov, 2018*]. However, such economic and geographical features as remoteness from the developed industrial regions and permafrost conditions hamper construction works and further development of vast Arctic territories. In this regard, improvement of construction technologies in the Arctic is an urgent task.

In Arctic conditions, construction is carried out according to the principle of preserving foundations in a frozen state, which increases the bearing capacity. Therefore, the key feature of construction in the Arctic is the thermal regime of the foundation, whose changes lead to permafrost thawing and may cause accidents [*Melnikov et al., 2019*]. In this regard, while constructing the heated buildings on permafrost, seasonal cooling devices (SCDs) are being applied. These devices support the frozen state of foundations decreasing the ground temperatures in winter despite the emitted heat from buildings. In studies of recent years, the best effect of SCDs coupled with thermal insulation layer has been documented. For example, extruded polystyrene foam boards decrease the heat flux from building to the frozen foundation in summer, when SCDs are out of operation [*Melnikov et al., 2014*].

Ventilated undergrounds are the engineering alternatives for maintaining the frozen state of foundations. For their deployment, pile supports are used with depths exceeding active layer to transfer the load on the frozen ground. Also, the technology of spatial frames (platforms) made of steel or wooden structures maintained directly on the surface is known. Having many points of support, such structures contribute to the uniform distribution of the load on the ground, while at the same time having a ventilated underground [*Vangool, 2018; Inzhutov et al., 2019*].

It is necessary to mention the practice of constructing roads and railways on permafrost with the use of artificial embankments that rise the upper horizon of permafrost (UHP) up to their base. Thanks to this approach, the design standards for construction on permafrost allow the use of peat, subsiding, high-ice, and other grounds as foundations. This ensures high economic efficiency of construction. An additional cooling measure is the use of heat-insulating

materials in the body of the embankment and screen structures (canopies) on the slopes of the embankment. Screen structures hinder snow accumulation, promote ventilation and cooling of embankment slopes in winter, and reduce the impact of solar radiation in summer [*Wenjie et al., 2006; Kondratiev et al., 2015; Chen et al., 2020*].

Above mentioned engineering measures to ensure the safe operation of buildings in the Arctic lead to an inevitable increase in construction costs. The remoteness of thousands of kilometers from the developed industrial regions greatly increases the cost of construction materials and structures at the construction site. Therefore, the application of forefront engineering solutions is a necessary condition for Arctic construction from a practical point of view, but insufficient from an economic point of view. Solving the problem of rationalizing construction in the Arctic requires localizing the production of construction materials near objects under construction using local raw materials and energy resources.

Construction technologies in permafrost areas indicate the high efficiency and attest to the high demand for thermal insulation materials [*Melnikov et al., 2014, 2019, 2021; Chen et al., 2020; Niu et al., 2021*]. Meanwhile, the Arctic territory has the largest raw material potential for their production in Russia – the deposits of opal-cristobalite rocks of the Yamalo-Nenets Autonomous Okrug [*Smirnov, Ivanov, 2015*] and zeolite rocks of Yakutia [*Ivanov, 2021*]. Publications of recent years indicate promising technologies for the synthesis of inorganic heat-insulating materials with a cellular structure called foam glass ceramics produced from these rocks [*Erofeev et al., 2018; Goltsman et al., 2020; da Silva et al., 2021; Konovalova et al., 2021*]. Due to its closed-porous structure, the material has low water absorption, retains thermal insulation properties in the ground, and has the required strength for use in the foundations of buildings and structures in granular form [*Ivanov, 2021; Melnikov et al., 2021*].

Further economic development of the Arctic will require hundreds of thousands of cubic meters of thermal insulation materials, where granular glass-ceramic foam can find wide practical application. Instead of traditional SCD and ventilated underground, in this work authors propose an alternative design solution in the form of a thermal insulation layer (TIL) insulating the building from the frozen foundation. Since the design standards for the permafrost require a rationale for the temperature regime for the entire period of operation, the purpose of this research is to evaluate the efficiency of using a proposed layer made of granular foam glass ceramics by numerical modeling of the thermal interaction between a heated building with a frozen foundation.

## MATERIALS AND METHODS

Modelling site is located in permafrost area in Novy Urengoy, Yamalo-Nenets Autonomous Okrug, Tyumen Region. The choice is determined by the corresponding climatic characteristics, the availability of the required calculated data from engineering-geological surveys, and raw material reserves in the form of nearby large deposits of opal-cristobalite rocks for producing granular foam glass ceramics [*Smirnov, Ivanov, 2015*].

Table 1 shows the climatic characteristics averaged for 2006–2020 according to the Urengoy weather station (no. 23453). The total solar radiation is given according to reference values [*SP 131.13330.2012, 2015*] reduced by considering average cloud conditions for the city of Tarko-Sale [*Scientific..., 1998*]. Mean annual ground temperature is –1.2°C at the lower boundary of zero annual amplitude depth (15 m), and active layer depth is 1.5 m. Base of the construction site is composed of fine slightly heaving sand with a low ice content (type 1) to a depth of 0.2 m and weakly decomposed peat with a low ice content (type 2) (0.2–5.5 m). The remaining section (5.5–15 m) consists of type 1 sediment.

Table 1. **Climatic characteristic of the construction area**

| Characteristic | Months | | | | | | | | | | | |
|---|---|---|---|---|---|---|---|---|---|---|---|---|
| | I | II | III | IV | V | VI | VII | VIII | IX | X | XI | XII |
| Air temperature, °C | –23.8 | –20.8 | –14.7 | –5.7 | –0.2 | 12.2 | 16.3 | 12.0 | 6.2 | –3.5 | –16.6 | –20.9 |
| Wind speed, m/s | 2.9 | 2.7 | 3.2 | 3.6 | 3.6 | 3.3 | 3.1 | 2.8 | 3.0 | 3.2 | 2.6 | 2.8 |
| Total solar radiation, W/m$^2$ | 2 | 15 | 44 | 74 | 105 | 111 | 113 | 82 | 49 | 19 | 6 | 0 |
| Snow depth, m | 0.64 | 0.73 | 0.80 | 0.75 | 0.42 | 0.07 | – | – | – | 0.10 | 0.23 | 0.48 |

Table 2. **Calculation ground characteristics**

| Ground type | Wetness, % | Temperature of freezing onset, °C | Thermal conductivity, W/(m·°C) | | Specific heat capacity, kJ/(m$^3$·°C) | | Heat of phase change, MJ/m$^3$ |
|---|---|---|---|---|---|---|---|
| | | | thawed | frozen | thawed | frozen | |
| 1 | 22 | –0.28 | 1.85 | 2.18 | 2784 | 2120 | 108 |
| 2 | 124 | –0.40 | 0.94 | 1.41 | 3444 | 2762 | 174 |

The calculated characteristics of the foundation grounds are presented in Table 2. The regime of groundwater found at a depth of up to 3.8 m depends on the infiltration of atmospheric precipitation and has fluctuations of up to 1.0 m.

As the study object, we have chosen a dome-shaped residential heated building with a minimum surface area of contact with the environment, which reduces heat loss through the walls. Technical ideas for the construction of energy-efficient residential architecturally expressive structures of aerodynamic shapes in the form of a sphere, dome, ellipsoid, lens, or cone are especially relevant in the climatic conditions of the Arctic and can be implemented in the near future [*Inzhutov et al., 2019*].

The dome-shaped building is mounted on a pre-prepared layer made of granulated glass-ceramic foam laid in a geosynthetic shell. The material is produced in industrial quantities and has the following characteristics: fraction 5–20 mm, calculated coefficient of effective thermal conductivity 0.09 W/(m·°C), bulk density 280 kg/m$^3$, compressive strength 1.8 MPa, specific heat capacity 260 kJ/(m·°C) [*Melnikov et al., 2021*].

The proposed design solution has multifunctionality and the following practical advantages:

1. Acting as a load-bearing element, the layer evenly transfers the load from the building without requiring special preparation of the natural base surface.

2. The layer is an artificial embankment that insulates a heated building from the frozen foundation by heat-insulating material.

3. The floor covering in the room is arranged over the surface of the layer, so there is no need for its thermal insulation, unlike a ventilated underground.

A cross section of the dome-shaped building is shown schematically in Fig. 1. The internal radius of the dome is accepted to be 4 m, taking into account the living area of the room equal to 50 m$^2$. The thickness of the thermal insulation layer is taken to be 1 m; in terms of thermal resistance, this is equivalent to a 0.3-m-thick layer of extruded polystyrene foam traditionally used in the construction on permafrost [*Melnikov et al., 2014, 2019*]. The material used for wall enclosing structures was lightweight concrete based on granulated glass-ceramic foam aggregate with a thermal conductivity of 0.12 W/(m·°C) and a heat capacity of 720 kJ/(m$^3$·°C).

Predictive calculation of the frozen base temperature field was carried out using a modern numerical method for solving the equation of non-stationary thermal conductivity, considering phase transitions and the amount of unfrozen water in the ground [*Melnikov et al., 2014, 2019*]. In solving the plane axisymmetric problem of finding the temperature field of the dome-shaped building base, its right half-plane was considered (Fig. 1) so that the left boundary of the calculation area adjoins the axis of the building.

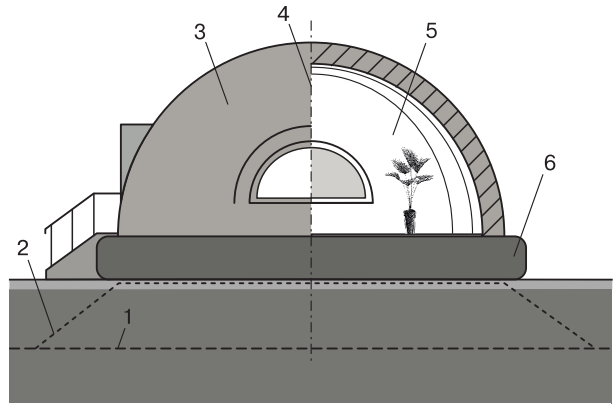


**Fig. 1. Cross-section of dome-shaped building:**

1 – natural location of UHP; 2 – normative location of UHP; 3 – enclosing structure made from lightweight concrete 0.5 m thick; 4 – building's axis of symmetry; 5 – inner living space; 6 – layer of granular ceramic foam in a geosynthetic shell.

The width of the calculation area was three times the internal radius of the dome in order to take into account the lateral temperature effect exerted by the surface. The vertical size of the calculation area corresponded to the depth of the lower boundary of the zero annual amplitude layer. In this regard, at the lower boundary of the calculation area, boundary conditions of the first kind were accepted with a constant temperature of –1.2°C, equal to the mean annual ground temperature. At the lateral boundaries of the computational domain, the condition of heat flux being equal to zero was accepted, which corresponds to boundary conditions of the second kind.

Boundary conditions of the third kind corresponded to the upper boundary of calculation area, including building and surface. Air temperature inside the building was accepted to be 23°C annually. For the surface, the mean monthly air temperature, total solar radiation, thermal resistance of the snow cover in winter (Table 1) and of the 0.1-m-thick surface turf with a thermal conductivity of 0.52 W/(m·°C) were specified. The heat transfer coefficient on the surface was calculated depending on the wind speed and the presence of snow cover (Table 1) according to the method [*Vabishchevich et al., 2017*].

The calculation start date of January 15, 2020 met the condition of installing a layer in winter in order to reduce the thermal impact in summer, when the dome construction was performed. The initial temperature distribution at the base corresponded to the borehole thermometry data on the start date of the calculation: from –6 to –4°C at a depth of 0–0.3 m, from –4 to –0.8°C at a depth of 0.3–3 m, and from –0.8 to –1.2°C at depths 3–15 m. Predictive calculation of the temperature field of the base was car-

ried out for the long operation of the building: up to 30 years and 8 months, given the high rate of climate warming with an annual increase in the mean air temperature by 0.08°C [*Pavlov et al., 2010*]. The final calculated date of September 15 corresponded to the maximum active layer depth at the base.

## RESULTS AND DISCUSSION

The results of calculating the thermal interaction of a building with a frozen foundation at the required time are the temperature field consisting of a set of temperature values of ground blocks 0.05 × 0.05 m in size, into which the calculation area is divided. The position of the UHP at the base changes under the influence of the building, which characterizes the boundary between frozen and thawed ground. Thus, knowing the temperature field at the base, it is possible to visualize the UHP using an isotherm characterizing the temperature at which the ground begins to freeze (Table 2).

Figure 2 shows a reduced fragment of the calculation area reflecting the dynamics of the position of the UHP directly under the dome-shaped building on a thermal insulation layer in comparison with a traditional 1-m-high embankment composed of the local ground type 1. In the second case, the calculation considered the thermal resistance of the floor inside the building, which corresponded to the territorial standard value of 5.5 m·°C/W for floors above unheated undergrounds of residential buildings.

The results of predictive calculation indicate significant dynamics of thawing at the frozen base. As a result, active layer depth under the central part of the building by September 2030 reaches 2.6 and 4.8 m for buildings on a thermal insulation layer and a traditional ground embankment, respectively (right and left in Fig. 2). The significantly greater thaw depth of a building on an embankment confirms the efficiency of a heat-insulating layer. However, in the proposed form, the design solution does not allow achieving the normative (close to the thermal insulation layer) position of the UHP (Fig. 1), which requires additional cooling measures.

In this regard, further calculations considered the year-round impact of screen structures installed along the perimeter of buildings. In winter, snow accumulation occurs on the surface of the structure, so the thermal resistance of snow on the ground surface has not been taken into account.

It should be emphasized that screen structures and their supports must remain stable under the standard snow load reaching 4 kPa for Arctic territories, according to [*SP 20.13330.2016, 2018*]. Taking this into account, their dimensions were limited to a 2.5-m distance from the building wall, as shown in Fig. 3, where the screen structures are shown schematically. The design features of screen structures in the construction of transportation structures on permafrost are covered in more detail in Russian and foreign literature [*Wenjie et al., 2006; Kondratiev et al., 2015; Chen et al., 2020*].

We considered the reflective effect of screen structures in the calculation from May to September by zeroing the values of total solar radiation (Table 1) when setting boundary conditions on the ground surface under the screens, which corresponds to the natural and numerical experiments of the authors [*Wenjie et al., 2006*]. The dimensions of the dome, embankment, and layer were preserved. The results of modeling the impact of screen structures are presented in Fig. 3.

The additional cooling measure taken into account in the calculation contributes to a significant cooling of the base under the building-enclosing structures, which is characterized by a rise of the

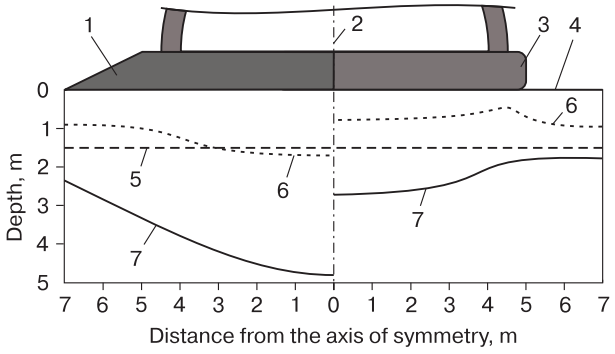


**Fig. 2. Impact of ground embarkment (*left*) and thermal insulation layer (*right*) on the change of UHP:**

1 – artificial embarkment; 2 – building's axis of symmetry; 3 – thermal insulation layer; 4 – base surface; 5 – natural location of UHP; 6 – September 2022; 7 – September 2030.

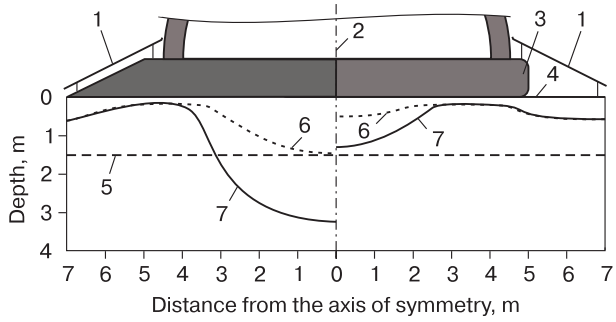


**Fig. 3. Impact of screen structures on the UHP for buildings on ground embarkment (*left*) and thermal insulation layer (*right*):**

1 – screen structure (shown schematically); 2 – building's axis of symmetry; 3 – thermal insulation layer; 4 – base surface; 5 – natural location of UHP; 6 – September 2022; 7 – September 2030.

UHP to the base of the embankment and the heat-insulating layer (left and right in Fig. 3). In the case of the ground embankment, however, the formation of a 3.4-m-deep talik under the center of the building (by September 2030) requires the use of alternative measures: deployment of horizontal or inclined SCDs under the building or replacing the embankment with a ventilated underground. Due to its low efficiency, the embankment was not considered in further calculations.

The efficiency of screen structures is noted when comparing the positions of the UHP in Fig. 2 and Fig. 3 (right) in the case of building a dome on a thermal insulation layer. Nevertheless, the dynamics of the talik formation under the center of the building with a depth of 1.4 m by September 2030 (Fig. 3, right) indicates that the UHP is not sufficiently close to the normative (Fig. 1). In order to minimize or completely eliminate the talik development at the base, authors changed the design parameters of the building in further predictive calculations: the dimensions of the dome and the thickness of the heat-insulating layer.

In the first case, we have reduced the internal radius of the dome by 1.3 times (to 3 m). In order to maintain the accepted area of the room, the building took therefore an elongated ellipsoid shape. With a fixed width of the ellipsoid, the area of the room will depend on its length, which does not affect changes in the UHP in the cross-profile of the base, as well as in the case of linear engineering structures (roads, pipelines, etc). Thus, the area of the room can significantly exceed the accepted one and is only limited by the constructive length of the ellipsoidal building. In the second case, the thickness of the thermal insulation layer was increased to 1.4 m (approximately by a factor of decreasing the radius of the dome) while maintaining the initial internal radius of the dome.

The results of modeling the thermal impact of buildings with structural changes made for the first and second cases are presented in Fig. 4 to the left and right of the axis of symmetry of buildings. It can be seen that the position of the talik by September 2030 in both cases reaches the boundary of the frozen foundation at a depth of 0.2 m, i.e., weak-bearing ground of type 2 remains frozen. The position of the talik by September 2050 characterizes the insignificant dynamics of thawing at the base to a depth of 0.4 m only under the center of buildings. The remaining part of the base is characterized by the constant position of the UHP throughout 30 years of building operation and its almost complete approach to the base of the thermal insulation layer, i.e. to the normative position in Fig. 1.

As seen from Fig. 4, safe operation of a heated dome-shaped building on a thermal insulation layer is possible only with the use of additional cooling measures and considering the design parameters of the building. This is achieved, for example, by reducing the width of the building, or increasing the thickness of the layer; it is possible to completely prevent the thawing of weak-bearing ground at the base without removal, and also without the use of SCD and a ventilated underground.

The economic efficiency of a thermal insulation layer made of granular ceramic foam with a thickness of 1.4 m in comparison with the installation of a pile foundation with a ventilated underground is an almost threefold reduction in cost per unit area. Based on the well-known practice of reducing costs by 30% when using horizontal SCD instead of a ventilated underground [*Melnikov et al., 2014, 2019*], savings in comparison with SCD reach a double value.

An additional economic effect is possible due to a reduction in transportation costs in the case of the production of granular glass-ceramic foam near Arctic construction sites using mobile complexes based on a railway platform [*Melnikov et al., 2021*]. The material is applicable as a filler in lightweight concrete used in the form of monolithic enclosing structures (domes, shells, etc.), blocks, wall panels, floor screeds, etc. Thus, granular glass-ceramic foam can replace traditional heat insulators (for example, polystyrene foam), whose transportation to the Arctic is unprofitable.

A disadvantage of the proposed construction technology is the limitation of the width of an ellipsoid building (6 or 8 m in size), while the width of buildings supported by horizontal SCDs reaches 100 m. In this regard, the construction zone will increase due to the additional area between buildings required for communications, passages, technical and economic needs, fire safety purposes, etc. Herewith, an ellipsoid building can have an unlimited length and area, and its plan configuration can differ from linear, taking the form of an arc, circle, torus, spiral, etc, despite the fixed width. Consequently, the location of ellipsoidal buildings in the built-up area

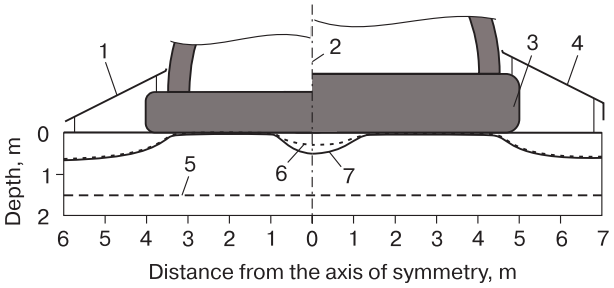


**Fig. 4. Impact of reduced (up to 3 m) inner radii of the dome (*left*) and increased (up to 1.4 m) thermal insulation layer (*right*) on the position of UHP:**

1 – screen structure (shown schematically); 2 – building's axis of symmetry; 3 – thermal insulation layer; 4 – base surface; 5 – natural location of UHP; 6 – September, 2022; 7 – September, 2030.

**Fig. 5. Dome-shaped building made of granulated foam glass ceramics.**

should be linked to their configuration in plan, considering the possible thermal interaction of adjacent buildings.

Currently, there is practical experience in the use of granulated foam glass ceramics in the construction of a dome-shaped building in the Natural Rehabilitation Complex "GNEZDO" in Tyumen, Fig. 5. The building was built on a 0.4-m-thick thermal insulation layer, which eliminated frost heaving under conditions of deep (up to 2 m) seasonal freezing of the base, as well as reduced heat loss through the floor. Wall blocks made of granulated glass-ceramic foam laid on the concrete load-bearing shell of the dome were used in the building enclosing structures.

The modeling results indicate broad prospects for such construction in the Arctic. The high strength, hydrophobicity, low thermal conductivity, flowability, and fire safety of granular foam glass ceramics allow the construction of dome-shaped and ellipsoidal buildings, which are not only an object of Arctic infrastructure, but also an element of landscape design, as follows from Fig. 5. Thus, the proposed technical solution can ensure the safety of not only permafrost proper but also the entire natural landscape, a part of the Arctic ecosystem.

## CONCLUSIONS

A technology for the Arctic construction of heated low-rise dome-shaped buildings on a thermal insulation layer made of granular glass-ceramic foam is proposed. Mathematical modeling of the thermal interaction of a building with a frozen base made it possible to estimate the influence of cooling measures and design parameters of buildings on the temperature regime of the frozen base. Buildings on an ellipsoidal shape with a width of 6–8 m on a thermal insulation layer of 1.0–1.4 m in thickness meet the condition for preserving the foundation in a frozen state. The cost of the ow-rise construction on permafrost is reduced because of the exclusion of seasonal cooling devices and ventilated undergrounds; localization of the the production of granular foam glass ceramics from local sources in remote Arctic territories also reduces the cost of construction. The use of granular foam glass ceramics in the proposed design solutions contributes to the rational use of mineral resources and preservation of permafrost, Arctic landscapes, and ecosystems.

***Acknowledgments.*** *This work has been performed within the framework of state assignment no. AAAA-A17-117051850061-9.*

## References

Chen L., Fortier D., McKenzie J.M., Sliger M., 2020. Impact of heat advection on the thermal regime of roads built on permafrost. *Hydrol. Process.* **34** (7), 1647–1664.

da Silva R.C., Puglieri F.N., Chiroli D.M., Bartmeyer G.A., 2021. Recycling of glass waste into foam glass boards: A comparison of cradle-to-gate life cycles of boards with different foaming agents. *Sci. Tot. Environ.* **771**, 145276.

Erofeev V.T., Rodin A.I., Kravchuk A.S., Kaznacheev S.V., 2018. Biostable silicic rock-based glass ceramic foams. *Magaz. Civil Engin.* **84** (8), 48–56.

Fauser V.V., Smirnov A.V., 2018. World Arctic: natural resources, population settlement, economy. *Arctic: Ecol. Econom.* **31** (3), 6–20.

Goltsman B.M., Yatsenko L.A., Goltsman N.S., 2020. Production of foam glass materials from silicate raw materials by hydrate mechanism. *Solid State Phenom.* **299**, 293–298.

Inzhutov I., Zhadanov V., Melnikov P., Amelchugov S., 2019. Buildings and constructions on the base of timber for the Arctic regions. *E3S Web of Conf.* **110**, 01089.

Ivanov K.S., 2021. Application of zeolites of Yakutia for obtaining granular thermal insulation material. *Bull. Tomsk Polytechnic Univ. Geo Assets Engineering*, **332** (8), 160–167 (in Russian).

Kondratiev V.G., Valiev N.A., Kondratiev S.V., 2015. Subgrade roads on icy permafrost: problems and ways to solve them. In: *Proc. Second Int. Symp. on Subgrade Problems in Cold Regions, 24–26 Sept.* STU, Novosibirsk, p. 26–33 (in Russian).

Konovalova N., Pankov P., Rush E., Avseenko N., 2021. Environmentally friendly road-building thermal insulating materials based on zeolite-containing rocks. *Lecture Notes in Civil Engin.* **141**, 103–109.

Melnikov V.P., Anikin G.V., Spasennikova K.A., 2019. Operation of thermosyphons beneath an oil tank at the Varandey field: Prediction by stochastic analysis. *Earth's Cryosphere* **23** (1), 54–61.

Melnikov V.P., Ivanov K.S., Melnikova A.A., Dashinimaev Z.B., 2021. Granular thermal insulation material for transport construction in the Arctic zones. Ekolog. Promyshlennost Ross. **25** (5), 32–38 (in Russian).

Melnikov V.P., Melnikova A.A., Anikin G.V., Ivanov K.S., 2014. Engineering solutions for building on permafrost in perspective energy-efficient enhancement. *Kriosfera Zemli* **18** (3), 82–90 (in Russian).

Niu F., Jiang H., Su W., Jiang W., 2021. Performance degradation of polymer material under freeze-thaw cycles: A case study of extruded polystyrene board. *Polymer Testing* **96**, 107067.

Pavlov A.V., Perlstein G.Z., Tipenko G.S., 2010. Actual aspects of modeling and forecasting the thermal state of permafrost in a changing climate. *Kriosfera Zemli* **14** (1), 3–12 (in Russian).

*Scientific and Applied Reference Book on Climate of the USSR*, 1998. Gidrometeoizdat, St. Petersburg, Iss. 17, 704 p. (in Russian).

Smirnov P.V., Ivanov K.S., 2015. Resource potential of the Tomcharu-Yakha River on diatomite raw materials. *Geol. Miner. Resursy Sibiri,* no. 2, 97–103 (in Russian).

SP 131.13330.2012, 2015. *Building Climatology*. Moscow, FTsS, 122 p. (in Russian).

SP 20.13330.2016, 2018. *Loads and Impacts*. Moscow, Standartinform, 76 p. (in Russian).

Vabishchevich P.N., Varlamov S.P., Vasiliev V.I., Vasilieva M.V., 2017. Numerical simulation of the temperature dynamics of railway foundation material in permafrost. *Mathem. Models Computer Simul.* **9** (3), 292–304.

Vangool W.J., 2018. Mechanical foundation system for new and retrofit construction. In: *Proc. Sixth Int. Structural Specialty Conf*. 13–16 June, Fredericton, Canada, p. 27–35.

Wenjie F., Wei M., Dongqing L., Luxin Z., 2006. Application investigation of awning to roadway engineering on the Qinghai-Tibet Plateau. *Cold Regions Sci. Technol.* **45**, 51–58.

*Received December 15, 2021*
*Revised March 6, 2022*
*Accepted October 17, 2022*

*Translated by Yu.A. Dvornikov*

**EARTH'S CRYOSPHERE**
SCIENTIFIC JOURNAL

*Earth's Cryosphere*, 2022, vol. XXVI, No. 6, pp. 28–36

*SNOW COVER AND GLACIERS*

# FEATURES OF GLACIATION IN THE NORTHERN BAIKAL AREA AT THE BEGINNING OF THE 21ST CENTURY

**M.D. Ananicheva[1,*], A.A. Abramov[2], Yu.M. Kononov[1], I.A. Patrikeeva[3], G.Yu. Pakin[1]**

[1] *Institute of Geography, Russian Academy of Sciences, Staromonetnyi per. 29, Moscow, 119017 Russia*
[2] *Institute of Physicochemical and Biological Problems in Soil Science, Russian Academy of Sciences, Institutskaya St. 2, Pushchino, 142290 Russia*
[3] *Lomonosov Moscow State University, Leninskie Gory 1, Moscow, 119991 Russia*

**Corresponding author; e-mail: maranan@gmail.com*

Glaciation of the northern Baikal region is associated with the mountain ridges surrounding Lake Baikal. The underlying rocks are in the frozen state. The existing glaciers are remnants of the vast Pleistocene glaciation, and their area is subjected to continuous shrinking. The analysis of core samples from trees allowed us to reconstruct the climatic background of the glaciation changes in the recent past. A dendroclimatic curve is divided into two periods: the first period lasted until about 1860–1865, when the summer air temperature was almost always below the average temperature for the entire considered period (~16°C); the second part is characterized by the above-average temperatures. During the field work, the current state of the regional glaciation was described for the areas of the Baikalsky, Barguzinsky, and Verkhneangarsky ridges. The areas of glaciation were determined from the Landsat 7 and Sentinel-2 satellite images for 2000 and 2021 and were controlled by orthophotoplans based on the UAV survey in August 2021. The maximum reduction of the area over 21 years is generally typical for small forms of glaciation and reaches 10–30% for the main glaciers. Data on temperature regimes of air and rock surface along an altitudinal profile in the Verkhneangarsky Ridge were obtained for the first time.

***Keywords:*** *Baikal, glacier, permafrost, satellite image, temperature, precipitation, dendrochronology, paleoreconstruction.*

***Recommended citation:*** Ananicheva M.D., Abramov A.A., Kononov Yu.M., Patrikeeva I.A., Pakin G.Yu., 2022. Features of glaciation in the northern Baikal area at the beginning of the 21st century. *Earth's Cryosphere* **26** (6), 28–36.

## INTRODUCTION

The northern Baikal region is characterized by the presence of several glacial groups confined to the Baikalsky, Barguzinsky, and Verkhneangarsky ridges (Fig. 1). Like all small forms, the glaciers are very sensitive to climate fluctuations and are unique in their existence near the southern boundary of the cryolithozone. They are mainly located in deep shaded cirques below the snow line and have mostly the northern, eastern, and southeastern exposures corresponding to directions of snowdrift transport. The studies of glaciation in this area began relatively recently, in the 1980s. The geocryological works were previously carried out only in the Baikal–Amur Mainline (BAM) area. Therefore, the obtained data complement the conceptions about the existence and interaction of different objects of the cryosphere in this zone.

Annual tree rings hold a special place among the natural archives, which are used to study the environmental conditions, including climatic factors. A number of advantages, such as high temporal resolution (year–season), precise dating, lifetime of trees, and wide distribution of woody vegetation gave the possibility to use the annual rings and chronologies, derived from them, in climatology, ecology, glaciology, archaeology, etc. [*Fritts, 1976; Vaganov et al., 1998; Shiyatov et al., 2002; Kononov et al., 2005, 2009; McCarroll et al., 2013; Arzhannikov et al., 2017; Voronin et al., 2020*]. The summer temperature reconstructed by the tree-ring chronology allows us to better understand the cause of climatic changes. Factual data on the air and soil surface temperature regime in the area of mountain glaciation of the Baikal region obtained for the first time allow us to assess its influence on the glacier dynamics.

## HISTORY OF GLACIER STUDIES IN THE BAIKAL REGION

Glaciers in the ridges in northern part of the Baikal region were first interpreted and mapped according to the aerial imaginary in the 1960s [*Kitov, Plyusnin, 2015*]. However, their field studies began much later because of the limited availability of these mate-

rials. First data on the Barguzin Ridge glaciers were published in the early 1980s, when employees of the Institute of Geography of the Siberian Branch of the USSR Academy of Sciences together with representatives of the State Center Priroda studied mountain areas of the Baikal area to work out the methods of the comprehensive investigation and mapping of natural resources of the region on the basis of satellite information. Snow-ice formations with signs of glaciers were detected during the interpretation of satellite images of the upper reaches of the Svetlaya River on the Barguzinsky Ridge. They involved modern moraines, zones of open ice, cracks, bergschrunds, and ogives. This allowed L.D. Dolgushin and G.B. Osipova [*1989*] to reveal that "on the Barguzin Ridge, there are many cirque snow patches and several small cirque glaciers" [*Kitov et al., 2014*]. Earlier, in 1979–1980, the expedition of the Institute of Geography of the USSR Academy of Sciences started working on the glaciers [*Aleshin, 1982*] and performed the first glaciological survey.

New research began only in 2009. The Sochava Institute of Geography, Siberian Branch of the Russian Academy of Sciences restarted the expeditionary glaciological studies in the Baikal region. Field works in 2011 and 2012 confirmed the existence of nival-glacial formations within the Baikalsky and Barguzinsky ridges [*Kitov et al., 2014*].

The discovered glaciers were included in the database (DB) of glaciers of the Northern Baikal, in the Registry of databases of the Russian Federation, as well as in the catalog of glaciers created by the Institute of Geography of the Russian Academy of Sciences [*Catalogue of Russian Glaciers, 2021*].

In 2017, a group of glaciers was discovered on the northwestern branch of the central part of the Verkhneangarsky Ridge. According to the results of the 2017–2018 studies, it was revealed that the Verkhneangarsky glacier group is represented by the cirque glaciers and other small forms of glaciation. It was logical to combine the glaciers of the region into the Baikal glacier system [*Ananicheva et al., 2019a*].

## PHYSIOGRAPHIC CHARACTERISTICS OF THE AREA

Lake Baikal is surrounded by the mountain ridges on all sides (Fig. 1). The Baikalsky Ridge extends for 300 km along the western shore of Lake Baikal within 54°–56° N. The highest point of the ridge is the Chersky Mountain (2572 m a.s.l.). The slopes of the ridge up to 900–1400 m a.s.l. are occupied by mountainous taiga forests. Larch taiga predominates in the middle and northern parts. Shrub thickets and sparse larch forests predominate above 1400 m a.s.l. [*Tyulina, 1990*].

The Barguzinsky Ridge frames Lake Baikal from the northeast. The low-mountain part of the ridge

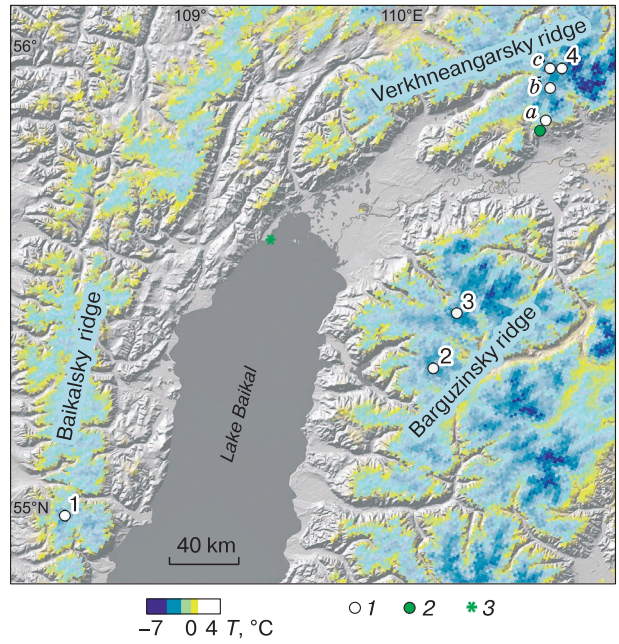


**Fig. 1. Studied area.**

(*1*) glaciers (1 – Chersky; 2 – Urel–Amutis; 3 – Akuli; 4 – Ogdynda–Maskit), (*2*) wood core sampling site, (*3*) Nizhneangarsk weather station. *T* is the mean annual rock temperature, °C [*Obu et al., 2019*]. Location of loggers to measure air and surface temperatures (*a* – 1280 m, *b* – 2280 m, *c* – 1845 m a.s.l.).

(600–1000 m a.s.l.) is covered by dark coniferous taiga with dense undergrowth. The middle-mountain (1600–1800 m) and high-mountain (1800–2800 m a.s.l.) parts are mostly devoid of continuous vegetation and are covered by coarse rock fragments [*Kitov et al., 2014*].

The Verkhneangarsky Ridge is a part of the Stanovoy Highland with the highest point of Bezymyannyi Peak (2641 m a.s.l.). The mountain ridge serves as the southern boundary of the North Baikal Highland and separates it from the Verkhneangarsky Basin. Mixed and larch forests predominate on the lower slopes and are replaced by mountainous tundra at higher altitudes.

The mountain glaciers in this region exist under the conditions of the dry continental climate in the area of continuous permafrost mainly due to precipitation brought from the Atlantic and Arctic Oceans. The redistribution of air flows coming from the Baikal Depression also contributes to the existence of the glaciers regions [*Ananicheva et al., 2019b*].

## METHODS

The authors used satellite images for the end of August – the beginning of September, i.e., in the period of maximum melting of the snow cover, to estimate the areas of glaciers in the Northern Baikal region in the 21st century. The archive of images includ-

ed data from Landsat 7 ETM+ L1 (2000) and Sentinel-2 L1C (for 2021) satellites. Contours were processed and distinguished on the portal [*Sentinel-hub EO-Browser, 2021*]. Delineation of the glaciers on the multispectral images was performed manually.

The error of delineation depended on the boundaries of particular glaciers, as it was not always possible to use the images with the surface completely free of seasonal snow. Taking into consideration pixel size (10 to 30 m) and the characteristic size of glaciers, the error in determining the area of the glaciers could be up to 5%.

The orthofotoplans and digital elevation models were created in the Metashape software on the basis of images from a DJI Mavic 2 Pro drone; the survey altitude was 400–500 meters. The survey was conducted on July 29–30, 2021. The state of glaciation in the middle of the 20$^{th}$ century was assessed using the archived aerial images from 1947–1949 provided by the Department of Remote Sensing Methods of the Institute of Geography, Russian Academy of Sciences. Orthotransformation of stereo pairs was also performed in the Metashape software. The quality of the archived images does not allow us to speak about comparable accuracy with the modern data, but we believe that these data are of interest for the reader.

Wood samples (Scots pine) for the dendroclimatic analysis were taken with a drill at the end of July 2019. At least two samples were taken from each tree at different radiuses. The sampling site was located on the southern macroslope of the Verkhneangarsky Ridge, on the right side of the Vershina Darmikov River valley in the vicinity of the upper forest boundary (Fig. 1). The sampling was performed at five plots spaced apart at about 500 m. At each plot, samples were taken from at least five trees. The sampling site was found at a considerable distance from the weather stations with available records. The nearest Nizhneangarsk weather station is located 90 km away. However, it is located on a flat area in the depression between mountain ridges and in the immediate vicinity of Lake Baikal, so its data cannot be representative of the studied site. Therefore, we used data from nine more stations (Table 1) to obtain a more general picture of climate conditions in the region.

Wood samples were collected and processed, the radial growth rate was measured, and chronologies were determined using standard dendrochronological methods [*Cook, Kairiuksitis, 1990*]. The radial growth rate was measured on the LINTAB 6 device using the TSAP Win computer program (0.01 mm accuracy). The climatic signal influencing on the width of annual rings was judged after the standardization (indexation) procedure. In the standardization of individual chronologies, the age trend is removed. The age trend is considered the main non-climatic factor that manifests itself in variability of the radial growth

Table 1. **Correlation matrix of summer air temperatures recorded at weather stations**

| Weather station | Nizhneangarsk | Bratsk | Kirensk | Mamakan | Bodaibo | Taksimo | Chara | Orlinga | Kalakan | Zhigalovo |
|---|---|---|---|---|---|---|---|---|---|---|
| Nizhneangarsk (90 km)*<br>55.5° N, 109.3° E, 477 m a.s.l. | | 0.67 | 0.78 | 0.72 | 0.65 | 0.78 | 0.62 | 0.82 | 0.58 | 0.85 |
| Bratsk (570 km)<br>56.2° N, 101.5° E, 410 m a.s.l. | 0.67**<br>**480*** ** | | 0.70 | 0.67 | 0.58 | 0.70 | 0.49 | 0.74 | 0.54 | 0.84 |
| Kirensk (250 km)<br>57.5° N, 108° E, 256 m a.s.l. | 0.78<br>**250** | 0.70<br>**430** | | 0.89 | 0.87 | 0.88 | 0.77 | 0.85 | 0.77 | 0.85 |
| Mamakan (270 km)<br>57.5° N, 114.1° E, 244 m a.s.l. | 0.72<br>**370** | 0.67<br>**780** | 0.89<br>**350** | | 0.99 | 0.94 | 0.89 | 0.81 | 0.85 | 0.78 |
| Bodaibo (280 km)<br>57.5° N, 114.1° E, 278 m a.s.l. | 0.65<br>**390** | 0.60<br>**790** | 0.87<br>**360** | 0.99<br>**10** | | 0.95 | 0.91 | 0.76 | 0.89 | 0.75 |
| Taksimo (250 km)<br>56.2° N, 114.5° E, 513 m a.s.l. | 0.78<br>**350** | 0.70<br>**820** | 0.88<br>**430** | 0.94<br>**170** | 0.95<br>**170** | | 0.91 | 0.83 | 0.89 | 0.82 |
| Chara (465 km)<br>56.5° N, 118.2° E, 709 m a.s.l. | 0.62<br>**580** | 0.49<br>**1020** | 0.77<br>**620** | 0.89<br>**270** | 0.90<br>**270** | 0.91<br>**220** | | 0.69 | 0.90 | 0.68 |
| Orlinga (310 km)<br>56° N, 105.5° E, 338 m a.s.l. | 0.82<br>**220** | 0.74<br>**270** | 0.85<br>**240** | 0.81<br>**530** | 0.77<br>**540** | 0.83<br>**550** | 0.69<br>**770** | | 0.72 | 0.95 |
| Kalakan (390 km)<br>55.1° N, 116.5° E, 612 m a.s.l. | 0.58<br>**470** | 0.54<br>**960** | 0.77<br>**600** | 0.85<br>**340** | 0.86<br>**340** | 0.89<br>**180** | 0.90<br>**220** | 0.72<br>**700** | | 0.72 |
| Zhigalovo (390 km)<br>54.5° N, 105.1° E, 416 m a.s.l. | 0.85<br>**280** | 0.84<br>**270** | 0.85<br>**380** | 0.78<br>**650** | 0.74<br>**650** | 0.82<br>**640** | 0.68<br>**850** | 0.95<br>**140** | 0.72<br>**740** | |

* Distance between the weather station and the sampling site, m.
** Pearson correlation coefficients.
*** Distances between stations, m.

rate. As a result, we obtain the chronologies – time series with dimensionless values (indices) allowing us to compare them with one another. Then, the individual indexed curves of the growth rate were combined into the single basic chronology. The standardization procedure was performed using the ARSTAN program [*Cook, Krusic, 2005*].

The temperature regime of air and the rock surface were studied using automatic loggers. The Onset HOBO MX2305 model with an internal electronic temperature sensor was used; the measuring accuracy was ±0.2°C. One logger was placed on a pole or on a tree trunk at a height of 2 m above the surface, and the second logger was placed a depth of 5 cm from the surface. Measurements were taken every 4 hours.

The radiocarbon analysis was performed in the Radiocarbon Laboratory of the Institute of Geography, Russian Academy of Sciences.

## SPATIAL AND TEMPORAL FEATURES OF THE SUMMER TEMPERATURE REGIME ACCORDING TO DATA FROM WEATHER STATIONS

According to numerous studies, the climatic signal in tree-ring chronologies obtained near the upper (high-altitude) forest boundary is most clearly manifested in data on air temperature of the warm season. To assess the potential of the resulting tree-ring chronology for the climate reconstruction, a comprehensive statistical analysis of the air temperature dynamics recorded at the weather stations was carried out. In spite of significant distances between weather stations and differences in the absolute heights, a significant ($p < 0.001$) statistical relationship between all stations for more than a 50-year-long period was revealed (Table 1).

The Bodaibo and Mamakan weather stations are located at a distance of only about 10 km from one another, which explains the high ($r = 0.99$) correlation between them. However, both stations have a significant disadvantage related to the length of the observation period. For the Bodaibo station, a longer series of measurements is available (1934–2005). For the Mamakan station, data are available for a period from 1958 to 2019. For further analysis, the series of weather records from the Bodaibo station was used. These data were supplemented with data from the Mamakan station for the last 14 years, which made it possible to obtain the generalized series for the period of 86 years.

All weather stations demonstrate a distinct regime of summer temperatures throughout the 20th and early 21st centuries. Up to the end of the 1970s, the summer temperature in the region tended to slightly decrease. Since the early 1980s, all weather

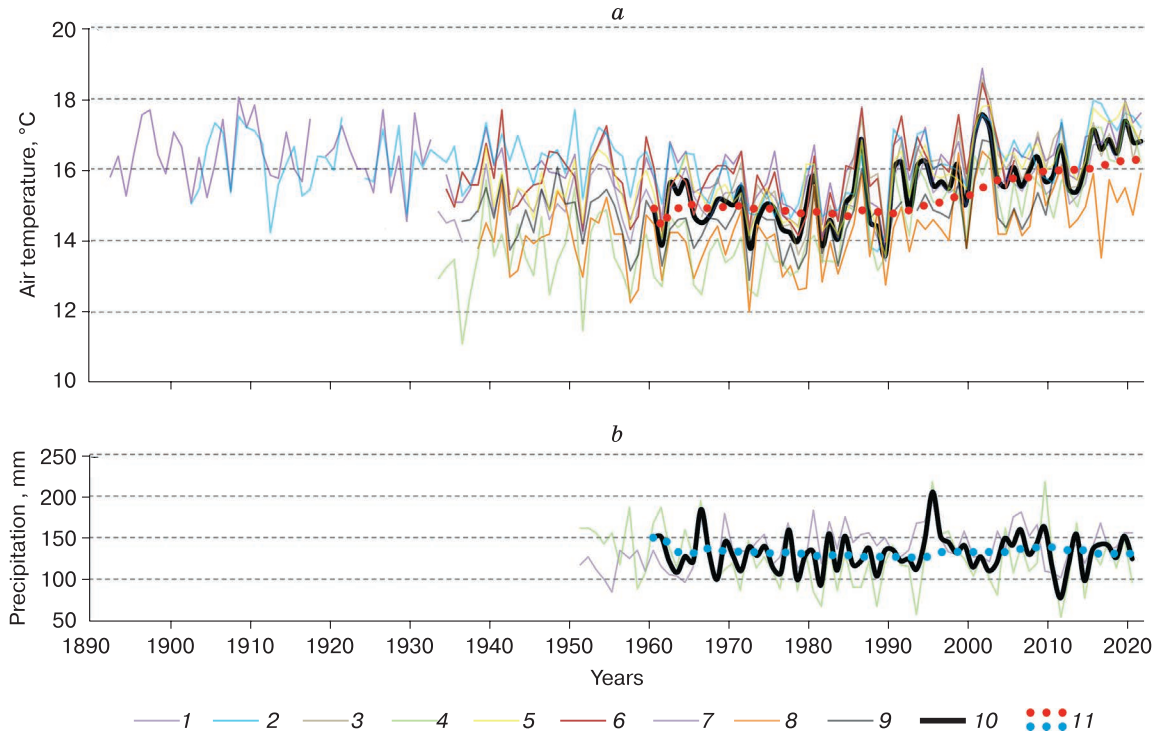


**Fig. 2. Mean summer air temperature controlling ablation (*a*) and precipitation of the cold period affecting snow accumulation (*b*) according to records of weather stations:**

*1* – Kirensk; *2* – Bratsk; *3* – Taksimo; *4* – Nizhneangarsk; *5* – Zhigalovo; *6* – Bodaibo; *7* – Orlinga; *8* – Chara; *9* – Kalakan; *10* – average values for all stations for the period of 1980–2021; *11* – moving average.

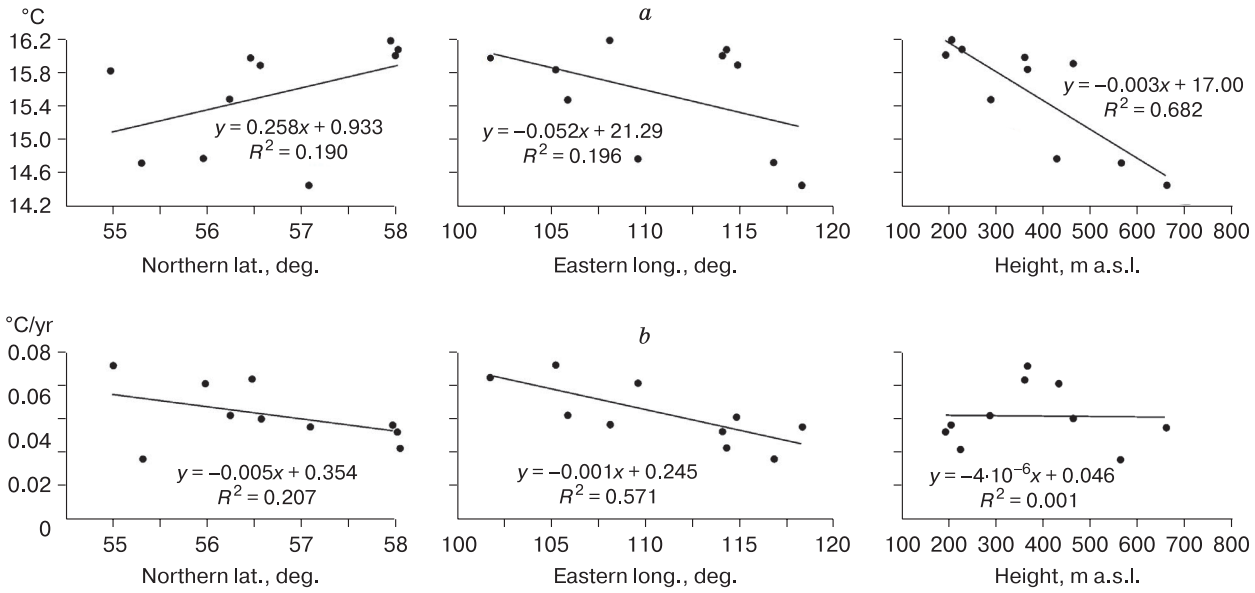


**Fig. 3. Dependence of the (*a*) value and (*b*) increase rate of the mean summer temperatures on the location of weather station.**

For (*a*), the period of 1960–2019 was used; for (*b*), the period of temperature rise manifested at all the stations from 1980 to 2019 was taken into account.

stations have indicated an opposite trend towards the rise in summer air temperatures. Precipitation is quite stable; the trend is weakly expressed: a slight increase until 2012 and a decrease in recent years have been recorded (Fig. 2). It is obvious that the value of the summer air temperature primarily depends on the altitude of the station (Fig. 3*a*). At the same time, the rate of warming in the late 20$^{th}$–early 21$^{st}$ centuries tends to slow down from west to east, as evidenced by the approximation coefficient $R^2 = 0.57$ (Fig. 3*b*). It should be noted that the latitudinal pattern in warming during recent decades also takes place. Only one weather station – Kalakan – substantially lowers the statistical significance of this pattern (Fig. 3*b*).

In general, fluctuations of the summer air temperature display a definite trend typical of the entire study area.

## RECONSTRUCTION OF THE SUMMER AIR TEMPERATURE

The dendroclimatic reconstruction for the last 230 years was obtained on the basis of the significant relationships between the width of annual rings and the summer air temperature (Fig. 4). Visual analysis subdivides the entire reconstructed period into two parts. In the first part (until about 1860–1865), the summer air temperature was almost always below the mean summer air temperature (~16°C) for the entire considered period. During the second part, the summer air temperature was generally higher than the mean summer air temperature, except for interval at the end of the 20$^{th}$ century (Fig. 4).

According to available data, the Little Ice Age (LIA) preceded the 20$^{th}$ century and was characterized by cooling and the development of mountain glaciation [*Lamb, 1977*]. Most likely, the first part of the presented reconstruction reflects the final stage of the LIA. During this time, summer temperatures dropped to 14.2–14.5°C (1794, 1804, 1847, and 1860), which was 1.8–1.5°C lower than the mean summer temperature for the entire considered period by. These years were the coldest in the last 230 years. Then, climate warming began, which passed through several stages to reach its maximum in the 1940s. Then, temperatures began to fall; from about 1965 to 1995, the summer temperatures were below the long-term average. The cooling in these 30 years was comparable to the cold interval at the beginning of the reconstruction (Fig. 4) in the mean summer temperatures. Since the 1980s, the summer temperatures have been steadily increasing. This coincides with the dynamics of the summer temperature fluctuations at the nearest weather station of Nizhneangarsk (Fig. 2*a*), where the mean summer temperature from the beginning of the observation to 2021 increased by 3°C.

The current climatic conditions of the study area for the glacier zone in winter are characterized by strong western winds leading to the redistribution and compaction of the snow cover and to the formation of thick snow patches and cornices [*Aleshin, 1982*].

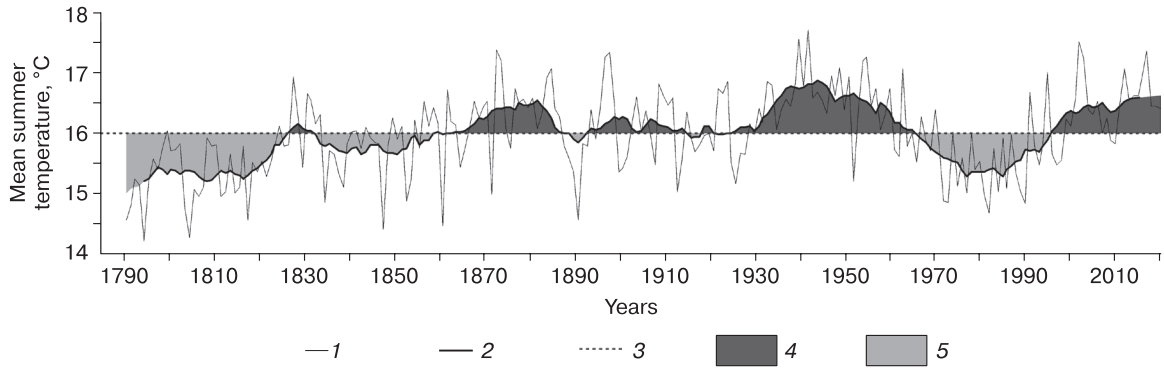


**Fig. 4. The dendroclimatic reconstruction of summer air temperatures in the Verkhneangarsky Ridge area for the last 230 years.**

*1* – annual values; *2* – smoothed by 11-yr average; *3* – average for the entire observation period; *4* – periods with temperatures above the average; and *5* – periods with temperatures below the average.

At the stations relatively close to glaciers (Nizhneangarsk, Kirensk), the mean annual air temperature ranges from –2.3 to –3.7°C (14 to 16°C in summer), annual precipitation is 390 mm, including 120–140 mm in the cold season (for 1966–2020). The maximum precipitation falls in July–August, the minimum, usually in March.

As seen from Fig. 2*a*, the trend of the mean summer temperature has been positive since the 1980s; it averages 2°C over 40 years. This contributes to the increased intensity of the glacier ablation and to prolongation of the ablation period. Warming takes place due to the summer and autumn temperatures resulting in a longer period of ablation.

Thus, climate changes in the past several decades have not contributed to the development of glaciation.

## DYNAMICS OF THE GLACIATION AREAS

According to the archival aerial imaginary of the late September in 1947–1949, the areas of the main glaciers were 0.19 km$^2$ (Ogdynda–Maskit), 0.24 km$^2$ (Urel–Amutis), and 0.53 km$^2$ (Chersky). In the 1960s, the areas of the Chersky and Urel–Amutis glaciers were 0.47 and 0.24 km$^2$, respectively [*Kitov, Plyusnin, 2015*].

Using the Landsat and Sentinel-2 images and orthophotoplans from UAV imagery, the areas of the glaciers were determined for the period 2000–2021. Table 2 demonstrates the results, including data on changes in the area of the glaciers in the 21st century according to various calculations. In terms of morphology, the studied glaciers belong to the cirque type of glaciers; some of them can be considered as small forms of glaciation.

Comparison of the areas occupied by glaciers in 2000 and 2021 attests to their reduction from about 2.0 to 0.9 km$^2$. Figure 5 demonstrates changes in the boundaries of the main glaciers for that period. The

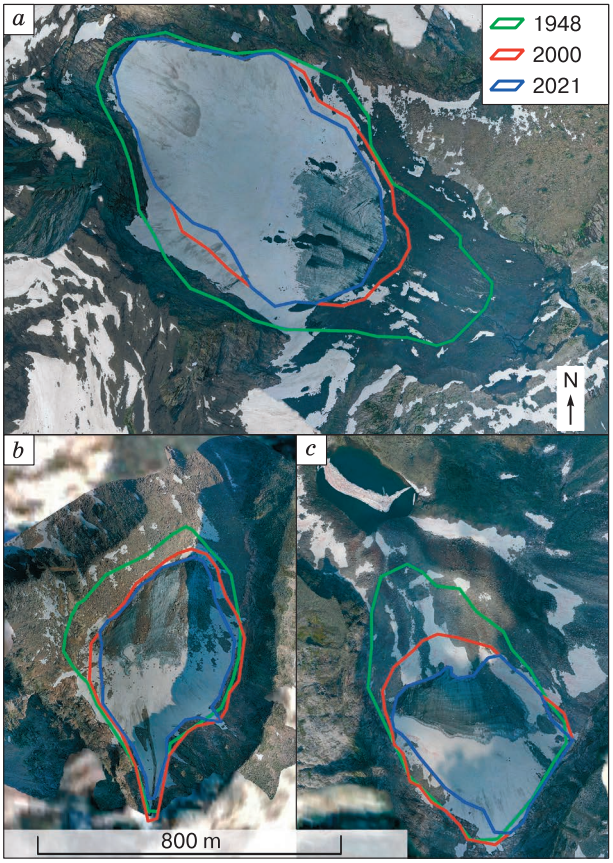


**Fig. 5. Contours of the Chersky (*a*), Urel–Amutis (*b*), and Ogdynda–Maskit (*c*) glaciers in 1948 (from aerial images) and in 2000, 2021 (from Landsat/Sentinel-2 imagery).**

The orthophotos by the end of July 2021 were used as the base layer.

Table 2. **Areas of glaciers of the Baikal region**

| No. | Ridge (total area of glaciers) | Glacier ID | Coordinates | Exposure | Area, km$^2$ | | | Reduction over, % (2000–2021) |
|---|---|---|---|---|---|---|---|---|
| | | | | | 2000* | 2012** | 2021*** | |
| 1 | Baikalsky (0.58 km$^2$) | Ru10-19.0001 | 108.70° E 55.0° N | SE | 0.03 | 0.04 | 0.01 | 67 |
| 2 | | Ru10-19.0002 | 108.70° E 55.01° N | SE | 0.10 | 0.06 | 0.08 | 20 |
| 3 | | Ru10-19.0003 | 108.70° E 55.01° N | E | 0.10 | 0.06 | 0.08 | 20 |
| 3 | | Ru10-19.0004 | 108.69° E 55.03° N | SE | 0.02 | 0.01 | 0.001 | 95 |
| 5 | | Ru10-19.0005 Razirvanny | 108.70° E 55.04° N | E | 0.10 | 0.03 | 0.05 | 50 |
| 6 | | Ru10-19.0006 Chersky | 108.70° E 55.06° N | E | 0.35 | 0.38 | 0.31 | 11 |
| 7 | | Ru10-19.0007 | 108.73° E 55.47° N | E | 0.01 | 0.01 | 0.01 | 0 |
| 8 | | Ru10-19.0008 | 108.65° E 55.83° N | SE | 0.09 | 0.03 | 0.04 | 56 |
| 9 | Barguzinsky (0.13 km$^2$) | Ru10-20.0001 Urel–Amutis | 110.36° E 55.46° N | NE | 0.15 | 0.09 | 0.13 | 13 |
| 10 | Verkhneangarsky (0.12 km$^2$) | Ogdynda–Maskit | 110.53° E 56.13° N | N | 0.17 | – | 0.12 | 29 |
| 11 | TOTAL | | | | 1.12 | – | 0.83 | 25.8 |

* According to [*Kitov, Plyusnin, 2015*].
** According to [*Catalogue of Russian Glaciers, 2021*].
*** According to [*Sentinel-hub EO-Browser, 2021*].

greatest reduction in area is typical for the small forms. In general, the dynamics of glaciers in the region reflect the trend of climate changes.

Table 2 demonstrates that the glaciers of the Northern Baikal region are currently at the stage of degradation of varying degrees of intensity. From 2000 to 2021, the area of all studied glaciers of the region decreased. The total reduction of the area of glaciers over these two decades reached 25.8%. For particular glaciers, it varied from 0 to 95%. This variation is related to the size of glaciers and their location. Position relative to the direction of moisture-carrying air flows, aspect (leeward or windward slope of the glacier location), shading (direct sunlight exposure is minimal), and a host form (the best preservation of small glaciers is in deep cirques) have the strongest influence. Glaciers on the slopes of the southeastern exposure are affected by the most intensive degradation; a little less glacier degradation is manifested on the slopes of the eastern and northern aspects. The key factors of the glacier degradation are the increase in the mean annual air temperature and, more importantly, the increase in the mean summer air temperature during the last decades, as well as the reduction of precipitation during the cold period. Compared to archival aerial images, the areas of major glaciers have decreased by 40% since the mid-20$^{th}$ century. It is interesting that the images of 1948 clearly illustrate the absence of glacier Ru10-19.0001, which confirms the high dynamics of variability of the smallest forms of glaciation in the area.

The maximum development of glaciation in the northern frame of Lake Baikal took place in the Late Pleistocene (35–15 ka ago). Deposits in the bottom of the central part of the valley of the Ogdynda–Maskit Glacier (1820 m a.s.l.) in the Verkhneanagarsky Ridge were dated (IGAN 7747). According to these data, this glacier has not descended lower, at least, for the last 5800 years. A zone of modern rock glaciers is an additional factor of the altitudinal zonation, which helps to reveal the area of glaciation in the past. The lower boundary of the rock glaciers coincides with the paleo-snow line [*Enikeev, Staryzhko, 2009*]. F.I. Enikeev [*2020*] reconstructed an orographic snow boundary of the maximum phase of the Sartan epoch of the Late Pleistocene glaciation. It encompassed the areas with predomination of solid precipitation forming the snow cover. The latter determined the areas of glacier feeding in that time. The largest of them covered the watershed areas of the ridges mentioned in this paper, and the Northern and Southern Muysky and Kodar ridges.

## THE AIR AND ROCK SURFACE TEMPERATURES OF THE VERKHNEANGARSKY RIDGE

In the mountainous areas of the studied region, permafrost is widespread at heights above 900–1000 m a.s.l. [*Ershov, 1989; Obu et al., 2019*]. This is confirmed by the presence of the active rock glaciers, the development of polygonal relief, etc. It is known that the subzero mean annual temperatures of rocks contribute to the stability of glacial systems, but data on rock temperatures have not been available so far for the studied region.

The automatic air and rock surface temperature sensors installed in the area of the Verkhneangarsky Ridge allowed us for the first time to analyze the patterns of changes of the air and rock surface temperatures from 460 to 2200 m a.s.l. for the period from August 2019 to the late July 2021 (Fig. 6) [*Abramov et al., 2021*].

The mean annual air temperature is –0.9°C at the level of Lake Baikal (460 m a.s.l., Nizhneangarsk weather station); it drops to –5.1°C at 1280 m a.s.l. and to –9.6°C at 2280 m a.s.l. The period of the subzero air temperatures in the mountains lasts from the end of September to May; at heights above 2000 m a.s.l., subzero air temperatures may be observed during the whole summer. In winter, temperature inversions may be formed, when a temperature in the lower part of valleys is lower than on tops of ridges.

Altitudinal gradients of the mean annual air temperature are 0.53°C/100 m at 460–1280 m a.s.l. and 0.45°C/100 m at 1280–2280 m a.s.l. These gradients agree with the gradients obtained for other mountain areas of the northern Russia.

The mean annual surface temperature was –6.2°C in the lower part of the Ogdynda–Maskit Glacier (1845 m) and –4.5°C in the upper part of the ridge (2280 m). Freezing of the active layer begins in the late September, and thawing begins in the late May. The higher surface temperature in the top part, as it can be seen from the character of temperature fluctuations, is most likely related to the formation of thick snow cornices, which isolate the rock surface from cooling. These data agree with the results of the temperature simulation at the permafrost table from satellite data [*Obu et al., 2019*].

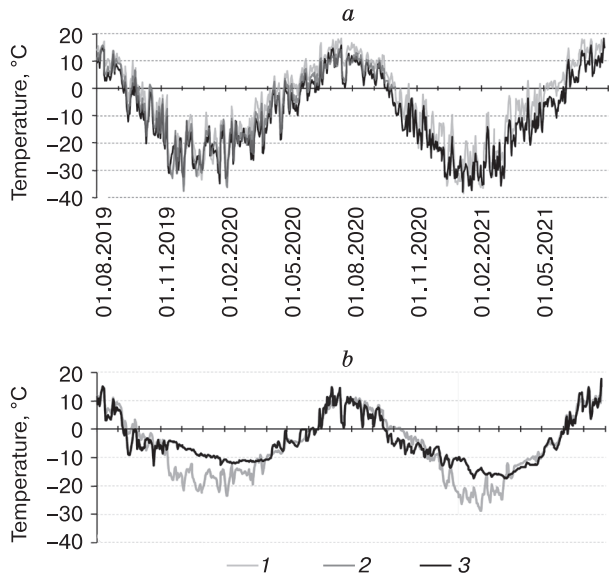


**Fig. 6. Dynamics of the (*a*) mean annual air temperature and (*b*) rock surface temperature in the Vershina Darmikov valley (*1, 3*) and at the Ogdynda–Maskit Glacier (*2*).**

*1* – 1280 m; *2* – 1845 m; *3* – 2280 m.

## CONCLUSIONS

The glaciers of the ridges in the Baikal region have been actively decreasing in recent decades. The small glaciers of the Baikal region located on the slopes of the southeastern exposure have been subjected to the greatest degradation. Glaciation of the three ridges has generally decreased by 25.8% over two decades of the 21st century, while relatively large glaciers have lost 10–30% of their area (and about 40% since the mid-20th century).

At present, the degradation rate of glaciers depends on their location on a slope, activity of snow-drift transport, and avalanche snow accumulation.

The temperature regime of the studied area is spatially stable. During most of the 20th century, the summer season temperature varied without a distinct trend. Since ~1980 and up to the present, the steady widespread warming is observed. The warming rate decreases in the eastward direction. The summer temperatures strongly depend on the elevation of weather stations. According to the dendroclimatic reconstructions, the period from the late 18th to the mid-19th centuries is characterized by the lowest summer temperature over the last 230 years.

Location of a glacier bed on permafrost contributes to maintenance of the cold reserve, which is a factor in preservation of these glaciers in cirques. The mean annual temperature of the rock surface (at a depth of up to 10 cm) in the area of glaciers existence (1800–2200 m a.s.l.) ranges from –5 to –7°C. In the crest part of the ridges, the milder temperature conditions on the surface of rocks are observed in winter, which is most likely associated with the formation of thick snow cornices.

The modern climatic conditions and the observed trends of their change cannot be considered favorable for the existence of glaciers in the Northern Baikal region. However, the glaciation is still far from the complete disappearance. Glaciers have decreased in area and thickness. A comprehensive assessment of their present state and forecast for the future is the relevant research task.

***Acknowledgments.*** *We are grateful to the staff of the Laboratory of Cartography of the Institute of Geography, Russian Academy of Sciences, for providing archival images of the Baikal ridges.*

*This work was supported by the Russian Foundation for Basic Research, project no. 19-05-00822 and, in part, by the State Assignment "Glaciation and Related Natural Processes in Climate Change" no. 0148-2019-0004 (AAAA-A19-119022190172-5).*

## References

Abramov A., Ananicheva M., Pakin G., 2021. Air and surface temperatures for the Northern Baikal area (Verhneangarsky ridge). PANGAEA, Data Publisher for Earth & Environmental Science. URL: https://doi.org/10.1594/PANGAEA.937618 (last visited: 30.10.2022).

Aleshin G.V., 1982. Modern glaciers and their relief-forming importance on the Baikal ridge. *Geografiya i Prirodn. Resursy,* no. 4, 133–136 (in Russian).

Ananicheva M.D., Pakin G.Yu., Kononov Yu.M., 2019a. Baikal glacier system, new findings. *Led i Sneg* **59** (1), 135–144 (in Russian).

Ananicheva M.D., Pakin G.Yu., Entin A.L., 2019b. Studies of the Upper Angara group of glaciers. *Led i Sneg* **59** (3), 423–432 (in Russian).

Arzhannikov S.G., Ivanov A.V., Arzhannikova A.V. et al., 2017. Age of the Jombolok lava field (East Sayan): evidence from dendrochronology and radiocarbon dating. *Russian Geology and Geophysics* **58** (1), 20–36. DOI: 10.15372/GiG20170103.

*Catalogue of Russian Glaciers,* 2021. Institute of Geography, Russian Academy of Sciences. URL: https://www.glacrus.ru/ (last visited: 30.10.2021).

Cook E., Kairiuksitis L. (eds.), 1990. *Methods of Dendrochronology: Applications in the Environmental Sciences*. Dordrecht, Kluwer Acad. Publ., 394 p.

Cook E.R., Krusic P.J., 2005. Program ARSTAN: a tree-ring standardization program based on detrending and autoregressive time series modeling, with interactive graphics. Tree-Ring Laboratory, Lamont-Doherty Earth Obs. Columbia Univ., Palisades NY. URL: http://www.ldeo. columbia.edu/tree-ring-laboratory/resources/software/ (last visited: 15.11.2021).

Dolgushin L.D., Osipova G.B., 1989. *Glaciers*. Moscow, Musl', 447 p. (in Russian).

Enikeev F.I., 2020. Peculiarities of the depression of the snow boundary of the Sartan glaciation in the Baikal region. *Geosfernye issledovaniya,* no. 4, 33–41 (in Russian).

Enikeev F.I., Staryzhko V.E., 2009. *Glacial Morphogenesis and Formation of Placers in Eastern Transbaikalia*. Chita, Izd. Chit. Gos. Univ., 370 p. (in Russian).

Ershov E.D. (ed.), 1989. *Geocryology of the USSR. Eastern Siberia and the Far East*. Moscow, Nedra, 515 p. (in Russian).

Fritts H.C., 1976. *Tree Rings and Climate*. London, UK, Acad. Press, 567 p.

Kitov A.D., Kovalenko S.N., Plyusnin V.M., 2014. Nival-glacial bodies in the Barguzin Ridge. *Led i Sneg* **54** (1), 48–60 (in Russian).

Kitov A.D., Plyusnin V.M., 2015. Database of glaciers in the Baikal region. Proc. Intern. Conf. *InterCarto. InterGIS* **21** (1), 318–322 (in Russian).

Kononov Yu.M., Ananicheva M.D., Willis I.C., 2005. High-resolution reconstruction of Polar Ural glacier mass balance for the last millennium. *Ann. Glaciol.* **42**, 163–170. DOI: 10.3189/172756405781812709.

Kononov Yu.M., Friedrich M., Boettger T., 2009. Regional summer temperature reconstruction in the Khibiny Low Mountains (Kola Peninsula, NW Russia) by means of tree-ring width during the last four centuries. *Arct., Antarct., Alp. Res.* **41** (4), 460–468. DOI: 10.1657/1938-4246-41.4.460.

Lamb H.H., 1977. *Climate: Present, Past and Future. Vol. 2. Climatic History and the Future*. London, UK, Methuen, 888 p.

McCarroll D., Loader N.J., Jalkanen R. et al., 2013. A 1200-year multiproxy record of tree growth and summer temperature at the northern pine forest limit of Europe. *The Holocene* **23** (4), 471–484.

Obu J., Westermann S., Bartsch A. et al., 2019. Northern Hemisphere permafrost map based on TTOP modeling for 2000–2016 at 1 km$^2$ scale. *Earth Sci. Rev.* **193**, 299–316.

*Sentinel-hub EO-Browser*, Sinergise Ltd. 2021. URL: https://apps.sentinel-hub.com/eo-browser/ (last visited: 30.10.2021).

Shiyatov S.G., Khantemirov R.M., Gorlanova L.A., 2002. Millennial reconstruction of summer temperature in the Polar Urals: data on tree rings of Siberian juniper and Siberian larch. *Arkheol., Etnogr., Antropol. Evrazii* **9** (1), 72–80 (in Russian).

Tyulina L.N., 1990. *Mountain Forests of the Northern Baikal Region*. Novosibirsk, Nauka, 118 p. (in Russian).

Vaganov E.A., Shiyatov S.G., Khantemirov R.M., Naurzbaev M.M., 1998. The variability of summer air temperature at high latitudes in the northern hemisphere for the last 1.5 ka: a comparative analysis of the data on annual tree rings and ice cores. *Dokl. Earth Sciences* **359** (2), 267–270.

Voronin V.I., Antipin V.S., Oskolkov V.A., Fedorov A.M., 2020. The age of the Patom crater: dendrochronological and biogeochemical investigations. *Geogr. and Natural Res.* **41** (4), 390–398. DOI: 10.1134/S1875372841040101.

*Received November 30, 2021*
*Revised July 21, 2022*
*Accepted November 10, 2022*

*Translated by A.V. Muravyov*

**EARTH'S CRYOSPHERE**
SCIENTIFIC JOURNAL

*Earth's Cryosphere*, 2022, vol. XXVI, No. 6, pp. 37–49

*METHODS OF CRYOSPHERIC RESEARCH*

# A PROBABILISTIC MODEL FOR PREDICTING SANDSTONE STRENGTH USING ELECTROMAGNETIC INDUCTION SOUNDING IN THE SOUTHERN YAKUTIAN PERMAFROST REGION: A CASE STUDY IN NERYUNGRI

**L.G. Neradovsky**

*Melnikov Permafrost Institute, Siberian Branch of the Russian Academy of Sciences, Merslotnaya St. 36, Yakutsk, 677010 Russia; e-mail: leoner@mpi.ysn.ru*

This paper presents a retrospective analysis of the geometric electromagnetic induction (EMI) sounding data. The data were acquired in the 1990s in the city of Neryungri to determine probabilistic relationships between unconfined compressive strength of saturated sandstone samples and the attenuation coefficient of the harmonic field induced by a high-frequency vertical magnetic dipole at 1.125 MHz in frozen sandstone massif. The results indicate that the consistent increase in the attenuation coefficient with decreasing strength of sandstone massif is correctly described by a logistic function equation. The inverse regression relationship is adequately described by a power function equation which can be used as a probabilistic model for predicting mean values of unconfined compressive strength of saturated sandstone massif (but not only sandstone rock samples) from the attenuation coefficient. The relative error of model predictions at the 70–80% confidence level is ±(27.7–32.0)%, which is close to the limit of allowable error (±20%) for laboratory measurements of mean strength of rock samples. This provides favorable conditions for applying the geometric EMI method in rock strength mapping for geotechnical engineering in Neryungri, as well as in areas of similar geology in southern Yakutia with sporadic permafrost.

***Keywords****: strength, sandstone massif, geometric electromagnetic induction sounding, field of high-frequency vertical magnetic dipole, amplitude decrease coefficient, statistics, histograms and variograms, probabilistic model, prediction error.*

***Recommended citation:*** Neradovsky L.G., 2022. A probabilistic model for predicting sandstone strength using electromagnetic induction sounding in the southern Yakutian permafrost region: a case study in Neryungri. *Earth's Cryosphere* **26** (6), 37–49.

## INTRODUCTION

V.S. Yakupov with coauthors [*1998*] attached great importance to probabilistic models seeing their great possibilities in solving petrophysical problems by geoelectric methods in the cryolithozone of Russia. This class of physical-geological models, to the development of which G.S. Vakhromeev made a great pioneer contribution, is very informative and is urgently needed for the most complete and reliable solution of forecasting problems by geophysical methods. These models integrate knowledge about the natural probabilistic relationships between the geological and geophysical characteristics of the Earth rather than represent particular isolated facts. V.P. Melnikov drew attention to the need of application of geophysical methods to solve the problems of predicting the state of permafrost [*1977, p. 60*]: *"Information is needed about how the parameters of the electromagnetic field characterize not the individual elements of the part of the section we are interested in, but the site and the type of landscape as a whole. The evaluation criteria can be the types of vertical electrical sounding curves*".

The solution to one of the geomechanical problems of frozen soil – the problem of probabilistic prediction of the average strength of a frozen high-temperature sandstone massif according to the geometric electromagnetic induction (EMI) sounding method – is discussed in this paper. This problem is important for design and survey geological works. Two study cases are considered: sandstone massif at the base of engineering structures in Neryungri and sandstone massif composing the sides of quarries of mineral deposits in the South Yakutian Basin.

The forecast problem is solved by the classical way of comparing and linking the values of two geological-geophysical characteristics to one another. From the side of geology, the laboratory characteristic $R_c$ is considered – the time limit of strength for uniaxial compression of sandstone samples in a water-saturated state (strength characteristic $R_c$). From the geophysics' side, the characteristic of the attenuation of the harmonic high-frequency field of a vertical magnetic dipole (HFVMD) in a frozen high-temperature sandstone massif is considered. The coefficient

of reduction of the amplitude of the vertical component of the field depending on the spacing of the dipole installation of the EMI method ($k$) is taken as a quantitative estimate of the measure of the HFVMD field integral attenuation within the layer of annual temperature fluctuations. A.T. Akimov wrote about the paramount importance of the layer of annual temperature fluctuations for the construction and operation of engineering structures [*1971, p. 10*], figuratively and accurately calling it a "factory" of cryogenic processes.

The results of a retrospective analysis of the EMI data obtained in Neryungri in the 1990s and presented in this article fully justify the choice of the coefficient $k$. For the first time, the statistical relationships of the coefficient $k$ with the $R_c$ are studied. On this basis, a previously unknown probabilistic model designed to predict the average strength of a sandstone massif in a water-saturated state was built. This model complements the results of petrophysical studies in the sporadic permafrost zone of southern Yakutia using well logging [*Grib, Samokhin, 1999*] and the georadar method [*Neradovsky, Fedorova, 2015; Neradovsky, Syasko, 2015*].

## STUDY AREA

The only comprehensive work on permafrost in southern Yakutia is the study by a team of researchers from Moscow State University headed by V.A. Kudryavtsev [*Kudryavtsev, 1975*]. It is rich in factual materials and their versatile systematization. This work provides information about all aspects of the natural environment of southern Yakutia before its industrial development. According to this study, the research area, including the city of Neryungri, is located in the folding zone along the marginal suture of the Cis-Stanovoy Trough in the southern margin of the Aldan Plateau within the Chulman Depression composed of coal-bearing sedimentary rocks of the Jurassic and Lower Cretaceous. In the southern part of the Chulman Plateau (in the middle course of the Chulman River), deposits of the Lower Cretaceous Kholodnik Formation (sandstones with layers of conglomerates, siltstones, and coal) lie on the sediments of the Gorkita Formation (sandstones with interlayers of conglomerates, siltstones, coal), with the former formation serving as the core of the Neryungri syncline with fault dislocations. This tectonic factor put a specific imprint on the permafrost in Southern Yakutia [*Buldovich et al., 1976*]. In general, the research area is characterized by complicated engineering and geocryological conditions, including heterogeneity and dynamism of permafrost soil conditions. This natural feature manifests itself in a significant depth of seasonal thaw–freeze processes (about 3–6 m) with the possibility of multiple transition of frozen rocks into a thawed state and vice versa.

The city of Neryungri – the administrative center of South Yakutia – is located 800 km southwest of Yakutsk. The city occupies the top and slopes of the watershed of the Chulman, Upper Neryungri, Maly Berkakit, and Amnunnakta rivers. The absolute heights of the watershed vary from 773 to 868 m a.s.l. The watershed surfaces have mild permafrost conditions with the development of sporadic permafrost of small thickness (20–50 m) with the mean annual temperature in the lower part of the layer of annual temperature fluctuations close to 0°C. The natural temperature regime of permafrost is largely controlled by the convective heat transfer processes. The movement of air and water from the surface and from the depths of the Earth along the bedrock fracture zones leads to a decrease in the permafrost thickness, as well as to an increase in the thickness of the layer of annual temperature fluctuations. According to various estimates , the lower boundary of this layer lies at a depth of 15–30 m.

Unstable and spatially variable natural temperature regime of the bedrock in Neryungri has been disturbed during the construction and operation of engineering facilities. Since 1975, complete degradation of permafrost in some of the city sites has taken place. According to the generalized thermometry data from survey boreholes, the temperature at the permafrost degradation sites at a depth of 10 m varies from 0 to 6.5°C. In areas of preserved permafrost with a thickness of 13–18 m, the mean annual temperature at a depth of 10 m is $-(0.4 \pm 0.1)$°C.

The analysis of data obtained by the South Yakutian Engineering and Construction Survey Center (Yuzhyakuttisiz) allows us to make a number of generalizations in relation to the geological structure of the territory of Neryungri.

First, the thickness of colluvium covering hard bedrock is about 2–3 m. Second, the bedrock of sedimentary genesis lies with a small dip angle. Third, up to a depth of 6–7 m, the bedrock is strongly loosened by physical weathering; below, to the maximum depth of drilling (10–20 m), its strength state is preserved. Fourth, the bedrock is composed mainly of sandstone, which is found in almost every borehole with a probability of 97%. The detecting probability of other rocks – interlayers or layers of siltstone, carbonaceous mudstone, and coal layers – is 18%, 8%, and 29%, respectively. Fifth, blocks of medium strength are most often found in the sandstone massif. The occurrence probability of sandstone blocks of low, reduced, or high strength is 26%, 41%, 50%.

These data are in agreement with the data on the coal-bearing rocks of the Aldan–Chulman Coal Basin. For example, according to V.M. Zhelinsky [*1980*], sandstone (fine-medium-coarse-grained) prevails in all the suites of Southern Yakutia. Its share varies from 52.6% in the Durai suite to 86.5% in the Yukhta suite. In the Neryungri Formation, spatially close to

the territory of Neryungri, the proportion of fine- to medium-grained sandstone is 78.7%.

## METHOD OF GEOMETRIC ELECTROMAGNETIC INDUCTION SOUNDING

The study of the HFVMD attenuation in a frozen high-temperature sandstone massif was carried out within the layer of annual temperature fluctuations by the EMI method with the medium-frequency electromagnetic sounding (MEMS) equipment manufactured by the NPO Sibtsvetmetavtomatika (Krasnoyarsk). This measurement technique made it possible to study all the components of the polarization ellipse of the HFVMD at four fixed frequencies (0.281; 0.562; 1.225; 2.250 MHz) and to determine the effective values of the electrical resistance $\rho_{ef}$ and permittivity $\varepsilon_{ef}$ from them [*System..., 1991*]. The modern analogue of the MEMS equipment is the digital KAV–EMM equipment. Until 2016, it was manufactured by R D Science LLC in Krasnoyarsk with the participation of employees of the Siberian Federal University. In the 1990s, the MEMS equipment was considered unique in terms of technical and economic parameters both in centers of engineering and construction surveys and in geological exploration enterprises. The antennas of the MEMS equipment have a round shape with an external diameter of 32 cm. The current in the transmitting antenna is regulated by the power supply block from 0 to 100 μA. The dynamic range of the microvoltmeter is 70 dB (from 0.5 to 1000 μV).

In Russia, the electromagnetic induction sounding method was classified as a geometric variant of the methods of AC geoelectrics. Abroad, it is referred to as the electromagnetic induction (EMI) method. Most often, EM-31 and EM-38 ground conductivity meters are used. A general overview of the EMI equipment is given in in the work of J. Boaga [*2017*].

The EMI method in Russia has been applied since the 1969s; the history of its development in Russia is briefly described in [*Igolkin et al., 2016*]. In addition, interesting and instructive information about the development of the inductive methods in the Urals is available on the website of the Bulashevich Institute of Geophysics of the Ural Branch of the Russian Academy of Sciences. In this institute, the technology of the EMI method was born through the efforts of the head of the Laboratory of Electrical Induction Survey G.V. Astrakhantsev and his colleague V.S. Titlinov. Almost unchanged, it has been used for many years with the equipment of DEMP-SF, AFS-78 and MFS-8, MFS-10 in the search for copper ore deposits and for solving other geological problems.

The EMI method is described in detail in [*Veshev et al., 1978; Zhuravleva et al., 1994; Titlinov, Zhuravleva, 1995; Zaderigolova, 1998*]; special guidelines have been published [*Frantov, 1984*].

The methodology for studying the process of attenuation of the HFVMD in the layer of annual temperature fluctuations has been successfully tested for many years in the Republic of Sakha (Yakutia) and partially in the Trans-Baikal Territory, Amur Region [*Neradovsky, 2018*] and consists of the following. At the sounding site, at a height of about one meter, a transmitting antenna with a constant frequency of HFVMD is fixed parallel to the earth surface. The receiving antenna is removed from the transmitting antenna at distances from 3–5 m to 50–60 m by consecutive steps (2–5 m). With the horizontal position of the receiving antenna, the amplitude of the vertical component ($H_z$) of the HFVMD is measured with a microvoltmeter of the MEMS equipment; in the vertical position of the receiving antenna, the values of the horizontal component ($H_r$) are measured. The measurement result obtained at a height equal to the height of the transmitting antenna is attributed to the standing point of the transmitting antenna [*Frantov, 1984*]. The combination of $H_z$, $H_r$ measurements (or other combination of the components of the HFVMD polarization ellipse) depends on the distance between the antennas and is commonly called the EMI signal.

The experience of using the EMI method in different engineering and geological conditions of the cryolithozone of Yakutia suggests that in almost all cases, a regular nonlinear decrease in the values of the $H_z$ and $H_r$ amplitudes is observed on the EMI signal graphs and is described by the power function equation with a high multiple determination coefficient ($R^2$). The value of the exponent of the power function is assigned to the coefficient $k$. This is the main difference between the EMI method and its usual application in Russia and abroad for the sole purpose of studying the effective electrical resistance ($\rho_{ef}$) in the kilohertz frequency range. Of course, it is necessary to study this static characteristic of the electric field, which is the most important in geoelectrics. However, the result of the study in relation to solving problems of geology will becomes fuller with the addition of new knowledge on the attenuation of the HFVMD in the layer of annual temperature fluctuations. Alas, this most important and, in addition, poorly studied side of the energy interaction of the HFVMD with an inhomogeneous anisotropic geological medium is not interesting to geophysicists. Since the end of the 1970s, foreign geophysicists have been expanding the boundaries of the scientific and practical application of the EMI method in order to study $\rho_{ef}$ without going beyond the limits of the kilohertz frequency range. This is seen from the review paper [*Doolittle, Brevik, 2014*]. Only in some early works (e.g., [*Sartorelli, French, 1982*] and from the report of the Alaska Department of Transportation and Public Facilities [*McNeill, 1980*], in which only fleeting attention is paid to the dynamic side of the EMI signal that is

considered just as an inductive response from the layers of the lower half-space[1]. However, this is done one-sidedly in the context of studying $\rho_{ef}$ without studying the attenuation of the vertical magnetic dipole (VMD) field. The reason for the reluctance of Russian and foreign colleagues to study the attenuation of this field at low and, especially, high frequencies is not exactly known. Perhaps, this is hindered by the stereotype of thinking in terms of the mathematical and physical incorrectness of solving this problem in the conditions of the screening influence of the primary VMD field on the weak inductive response of the geological medium in the secondary field[2]. Surely, in the near zone of the primary field source, its influence on the secondary field is so strong that it prevents obtaining correct and reliable knowledge about the petrophysics of the lower half-space. The influence persists in the transitional zone of the source, where it is weakened to such an extent that it no longer prevents reliable study of the induction effect in the total field in dependence of the geological setting [*Neradovsky, 2018*].

In Neryungri, the work by the EMI method was carried out in the1990s during the experimental and methodological experiments in order to study the engineering and geological capabilities of this new and promising method. According to the recommendations of geophysicists of Yakutzoloto (Yakutian Gold) Company, who had extensive practical experience with the EMI method, the study of the sandstone massif was carried out at a frequency of 1.125 MHz and a spacing of 5–50 m with the measurements of $H_z$ and $H_r$ values for the sole purpose of determining the values of $\rho_{ef}$ from their ratio. With a retrospective analysis of the data of the EMI method, the goal has changed. Only the vertical component of the HFVMD was studied in order to determine the values of the *k* coefficient. The reason for this is explained by the higher geological informativeness of $H_z$ in comparison with $H_r$. According to A.A. Petrovsky [*1971*], $H_z$ carries about 70% of information about anomalous objects that are located in the lower half-space. Moreover, practical experience shows that $H_z$ is less dependent on the noise influence (topography, engineering structures, etc.).

As for the $H_r$ and $H_z$ measurements, they were made in the spring, i.e., in the period, when the seasonally thawing colluvium layer was completely frozen. Owing to this, the investigation depth of the sandstone massif by the EMI method increased. The distorting influence of the seasonally thawed layer on the HFVMD attenuation in this massif disappeared.

The effective penetration depth of the HFVMD into this layer ($h_{ef}$) was estimated for the entire territory of Neryungri by the values of the reduced distance parameter (*P*) equal to the product of the modulus of the complex wave number ($\zeta$) by the spacing values. The values of $\zeta$ were calculated according to the formulas of electrodynamics of continuous media. They are not difficult to find in any of the numerous textbooks on electrical exploration and therefore they are not given in this article.

The generalized estimates of the average effective values of electrical conductivity, as well as the real part of the complex permittivity ($\varepsilon_{ef}$) necessary for the calculation were determined in different ways. The conductivity was estimated by $1/\rho_{ef}$. The average value of $\rho_{ef}$ was calculated from the ensemble of $H_z/H_r$ measurements at the EMI points with the conversion of the $H_z/H_r$ ratio to the corresponding parameter *N*. Implicitly, this parameter takes into account the frequency influence of $\varepsilon_{ef}$ on $\rho_{ef}$. The values of *N* for $H_z/H_r$ values in the tabulated form are presented in the work by V.I. Igolkin with coauthors [*2016, p. 260–266*]. The formula for calculating $\rho_{ef}$ is given in the same paper in the following form:

$$\rho_{ef} = Nr^2f, \quad (1)$$

where *N* is the parameter of the dielectric constant, rel. units; *r* is the spacing, m; and *f* is the frequency, MHz.

For example, for the $H_z/H_r$ value equal to 1.5 rel. units measured at a distance of 15 m and at a frequency of 1.125 MHz, we find $N = 1.2$ rel. units in the specified table [*Igolkin et al., 2016, p. 263*]. Substituting it into formula (1) together with the values of the spacing and frequency, we get a $\rho_{ef}$ equal to 303.8 Ω·m.

Unfortunately, the value of $\varepsilon_{ef}$ in the presented procedure for determining $\rho_{ef}$ remains unknown. If, during the experimental and methodological works, measurements were made of the large and small axes of the polarization ellipse of HFVMD and of the angle of inclination to the horizon of the large axis, then the values of $\varepsilon_{ef}$ could have been determined using special pallets and nomograms [*Lebedev et al., 1991*] together with the values of $\rho_{ef}$. However, the lack of proper experience at the initial stage of mastering the MEMS equipment and the EMI method prevented the implementation of such a possibility. The missing values of $\varepsilon_{ef}$ were found in the course of georadar surveys in Neryungri with an OKO-2 georadar and the Triton antenna unit operating at a central frequency of 50 MHz [*Neradovsky, 2022*].

The values of $\varepsilon_{ef}$ were determined in a standard way by the angle of inclination of the branches of the

[1] This is what geophysicists call the geological medium in theoretical studies.

[2] The author of this article witnessed a similar situation when, in the mid-1980s, scientific and production tests of the first domestic samples of ground-penetrating radars were initiated by the Committee on State Construction of the Russian Federation. At that time, the absolute majority of geophysicists who worked not only in engineering and geological surveys but also in geological exploration categorically denied the real facts of the depth resolution up to 20–30 m of soundings in frozen soils at a frequency of tens to hundreds of megahertz.

hodographs of diffracted waves. The results of the determination of $\varepsilon_{ef}$ by this method are confirmed by an independent control check. It was made in Moscow by R.R. Denisov with the help of the well-known computer program "Georadar-Expert" developed by him. According to georadar data, the $\varepsilon_{ef}$ values for the layers were distributed in depth as follows. In an undifferentiated layer of road pavement soils, colluvial deposits, and a strongly weathered upper part of sandstone, the values of $\varepsilon_{ef}$ to a depth of 5–7 m vary in a narrow range from 4.12 to 4.88 rel. units. In the lower, relatively intact part of the sandstone massif, the values of $\varepsilon_{ef}$ at a depth of 7–28 m are equal to 3.5–4.0 rel. units. The decrease is caused by a change in the genesis and composition of geological formations with a natural decrease in the amount of clay material in deeper layers. In general, the average value of $\varepsilon_{ef}$ according to georadar data is 3.93 rel. units. This value obtained at a frequency of 50 MHz is further used to calculate the module $\zeta$ at a frequency of 1.125 MHz. The difference in frequency is very large, but it can be ignored without harm to the merits of the case, guided by the unspoken decision of the international community of geophysicists – possibility of using theoretical concepts of the so-called "georadar platform" in georadiolocation, where the values of $\varepsilon_{ef}$ almost do not change in a wide frequency range from 1 MHz to 1 GHz [*Vladov, Sudakova, 2017*].

As for the electrical conductance characteristic $1/\rho_{ef}$, the generalized estimate of its average value at a frequency of 1.125 MHz and in the spacing range of 5–50 m is 1/2800 Ω·m (0.000357 S). The actual values of $\rho_{ef}$ are determined from palettes and nomograms [*Lebedev et al., 1991*] based on the totality of $H_z/H_r$ values determined at all points of the EMI, in which the attenuation of the HFVMD in Neryungri was studied. The calculation based on the average values of $1/\rho_{ef}$ = 0.000375 S and $\varepsilon_{ef}$ = 3.93 rel. units showed that for this city the generalized value of the module $\zeta$ is 0.062 $m^{-1}$. The values of $P$ equal to 0.311 and 3.11 rel. units correspond to the spacing values of 5 and 50 m. Do they satisfy the criteria according to which the boundaries of the intermediate zone of the source of the primary HFVMD favorable for work by the EMI method are established?

Theoretically, the boundaries of the intermediate zone are set according to the criterion $P << 1$ (the neighborhood of the near zone) and $P >> 1$ (the neighborhood of the far wave zone). G.V. Molochnov and M.V. Radionov [*1983*] consider it correct to use the EMI method to designate the boundaries of the intermediate zone by $P$ values in the range of 1–10. V.I. Igolkin et al. [*2016*] link the boundaries of the intermediate zone with the accuracy of measuring the components of the HFVMD. These researchers establish the boundaries of the transitional zone according to the criterion $0.01 \leqslant P \leqslant 100$ with an accuracy of up to 1%. In the field, it is impossible to ensure such accuracy, which means that, strictly speaking, it is impossible to apply the proposed criterion. Thus, what criterion should be chosen? Let us make a choice based on a general theoretical criterion. Although it is fuzzy, it is applicable in many cases. In accordance with this criterion, the above defined values of $P$ equal to 0.311 and 3.11 rel. units, correspond to the boundaries of the intermediate zone, in which the problem of probabilistic prediction of the strength of the sandstone massif according to the EMI method is theoretically solved correctly.

To determine the desired generalized estimates of the average values of $h_{ef}$, we turn to the little-known work of V.S. Titlinov and R.B. Zhuravleva [*1995, p. 13*], borrowing from it a graph of the theoretical dependence of the $h_{ef}/h_s$ ratio on the parameter $P$. The theoretical value of the maximum thickness of the skin layer ($h_s$) (skin depth or penetration of the HFVMD at a frequency of 1.125 MHz) is determined by a simple formula given in the same work with reference to the textbook on electrical survey by M.S. Zhdanov:

$$h_s = \sqrt{2}/\zeta, \qquad (2)$$

where $h_s$ is the thickness of the skin layer, m; $\zeta$ is the modulus of the wave number, $m^{-1}$.

Setting $\zeta$ equal to 0.062 $m^{-1}$ in formula (2), we get $h_s$ = 22.8 m. With a value of $P$ = 0.311 rel. units, according to the above graph, we find $h_{ef}/h_s$ = 0.26. From this ratio, in turn, we calculate the value of $h_{ef}$ = 22.8·0.26 = 5.9 m. Similarly, for $P$ = 3.11 rel. units and the corresponding $h_{ef}/h_s$ = 0.78, we find $h_{ef}$ = 17.8 m.

Thus, for Neryungri, the accepted frequency (1.125 MHz) and the spacing range (5–50 m) provide correct determination of the attenuation of HFVMD within a relatively intact lower part of the sandstone massif at a depth of 5.9–17.8 m. This depth corresponds to the depth of the geological study of the strength of the massif in the core samples.

## SANDSTONE STRENGTH

In laboratory environments, the quantitative assessment of the strength of sandstone samples taken from air-dry or frozen core samples was carried out according to $R_c$ values. This strength characteristic is widely and universally used in Russian soil mechanics. In foreign geotechnics, it is applied together with other geological and mining characteristics in order to build probabilistic models. For example, a neural model of multiple regression in order to predict the velocity of borehole drilling with a diamond bit in the fields of Turkey [*Basarir et al., 2014*].

From the thousands of boreholes drilled by YuzhYakuttisiz during the construction development of Neryungri, $R_c$ values were collected from only 218 boreholes, but this amount of factual material is

Table 1. **Statistics of classification of laboratory values of the time limit of strength for uniaxial compression of sandstone samples in a water-saturated state**

| Parameter | $R_c$, MPa | | |
|---|---|---|---|
| | groups 2–4 | group 5 | group 6 |
| Arithmetic mean | 10.5 | 34.8 | 65.5 |
| Median mean | 11.5 | 38.0 | 58.9 |
| Modal mean | 18.0 | 16.2 | 54.2 |
| Weighted mean | 10.5 | 30.8 | 65.9 |
| Standard deviation | 12.1 | 11.1 | 16.4 |
| Coefficient of variation, % | 31.4 | 32.7 | 25.1 |
| Minimum value | 2.5 | 15.0 | 50.2 |
| Maximum value | 14.8 | 49.0 | 114.6 |
| Sample size | 46 | 104 | 68 |

Note: Groups 2–4 to sandstone of low, reduced, and moderately low strength ($R_c$ = 15 MPa); group 5, to moderately strong sandstone ($R_c$ = 15–50 MPa); and group 6, to strong sandstone ($R_c$ = 50–120 MPa).

sufficient for a reliable assessment of probability distributions of $R_c$ values using the "Stage" program [*Kulaichev, 2006*]. As for the error in determining the average $R_c$ values in the YuzhYakuttisiz soil laboratory, it is not known exactly. However, according to GOST (State Standard) 21153.2-84 [*1984*], with mass laboratory determinations in a series of six samples taken from each core, the error cannot be higher than ±20%.

With the arithmetic mean and median $R_c$ values of 39.1 and 40.7 MPa, the particular values varied from 2.5 to 114.6 MPa with the variation coefficient of 59.6%. In 70% of cases, $R_c$ values were distributed near the averages in the range of 15.8–62.4 MPa. According to [*GOST 25100-2020, 2020*], in the ordered sequence of $R_c$ increase in Neryungri, the sandstone massif is represented by five strength groups. The first and second groups (sandstone of low and reduced strength with $R_c$ equal to 1–5 MPa) are rarely present ((probability 2.7%). The probability of the third group (low-strength sandstone with $R_c$ = 5–15 MPa) is higher and equals 19.3%. The fourth group of moderately strong sandstone with $R_c$ = 15–50 MPa has the maximum probability of 47.7%. The fifth group of strong sandstone ($R_c$ = 50–120 MPa) has a lower probability of occurrence (30.7%).

The group statistics of $R_c$ values are presented in Table 1. With an abnormal distribution of $R_c$ values, the correct theoretical indicator of the average distri-

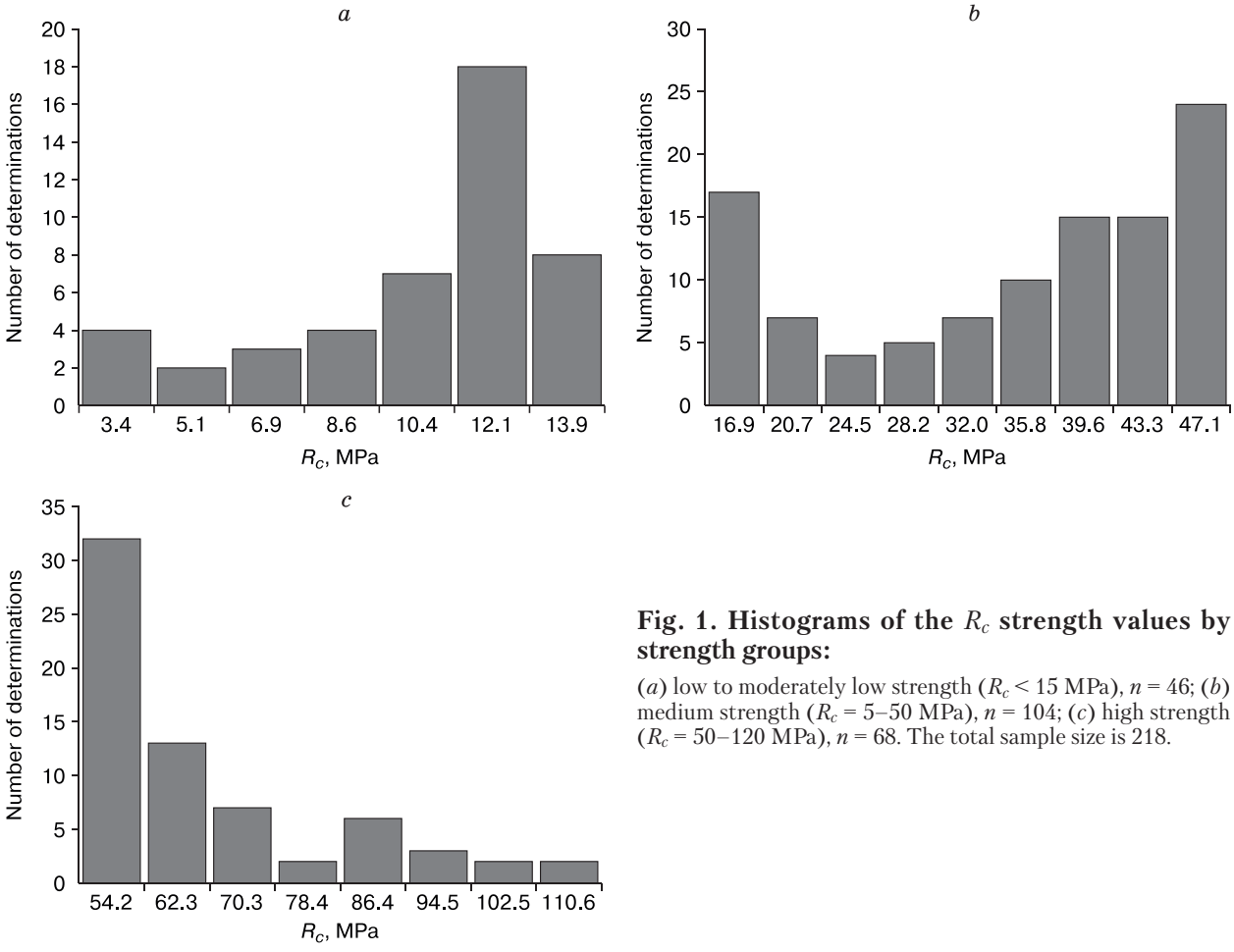


**Fig. 1. Histograms of the $R_c$ strength values by strength groups:**

(*a*) low to moderately low strength ($R_c$ < 15 MPa), $n$ = 46; (*b*) medium strength ($R_c$ = 5–50 MPa), $n$ = 104; (*c*) high strength ($R_c$ = 50–120 MPa), $n$ = 68. The total sample size is 218.

bution position is the median average value. The proximity of the arithmetic mean and weighted average values to the median average value serves as a true indication that, in Neryungri, the background distribution of the strength values of the sandstone massif obeys the normal law. However, with a small number of determinations in group samples (Table 1), the background of the $R_c$ distribution is complicated by the imposition of anomalous components on it. As a result, an inhomogeneous probabilistic structure is formed. It manifests itself as isolated maxima at the ends of histograms with abnormally low (below 10.4 MPa (Fig. 1*a*)) or high (above 70.3 MPa (Fig. 1*c*)) $R_c$ values with a small frequency of their occurrence.

The areas of abnormal $R_c$ values are considered as rare events indicating the appearance of two opposite groups of sandstone massif at the base of engineering structures in Neryungri: low and high strength. Most often, at the base of engineering structures there are sections of sandstone massif of medium strength and partly of low strength. These events are detected by the maxima of the general histogram of the $R_c$ characteristic (Fig. 2). The first maximum with a mode of 10–20 MPa identifies a joint group of a sandstone massif of low, reduced, and moderately low strength. In terms of construction, they are considered as an undifferentiated category of semi-rocky soils. The second and third maximums with modes 40–50 and 80–90 MPa indicate the existence of two strength groups in the sandstone massif forming the dominant category of rocky soils. These are the groups of moderately strong and strong sandstone.

## VERTICAL MAGNETIC DIPOLE FIELD

Recall that the values of the coefficient $k$ are taken as a quantitative assessment of the integral measure of the attenuation of HFVMD in the sandstone massif within the layer of annual temperature fluctuations. The error in determining this coefficient is estimated from the results of control measurements of $H_z$. With an average relative error of measuring $H_z$ values equal to 12.7%, a similar error in determining the values of the $k$ coefficient was 7.6%.

In Neryungri, the values of the $k$ coefficient vary from 1.08 to 4.41 $m^{-1}$. The width of the integral variability in the coefficient of variation is rather large and amounts to 42.3%. The average values of the $k$ coefficient are close and equal to 2.31; 1.88; 1.63 $m^{-1}$. In 70% of cases, the values of the $k$ coefficient vary near the average in the range of 1.33–3.29 $m^{-1}$.

Histograms constructed with reference to the boundaries of the rock – semi-rock soil classes show that the values of the $k$ coefficient inherit from the strength of the sandstone massif an inhomogeneous probabilistic structure, which is not described by either the law of normal distribution or the laws of abnormal distribution (Fig. 3). The statistics of the values of the coefficient $k$ obtained for the groups of different strength of the sandstone massif are presented in Table 2. It follows from this table that with a decrease in the strength of the sandstone massif, the average values of the $k$ coefficient increase. However, this variability is different, both in terms of the averages and the coefficients of variation. With a general decrease in the average values of the $R_c$ strength characteristic by 6.3 times, the average values of the $k$ coefficient increase by 2.6 times. With a more even integral variability (by the coefficient of variation) of the values of the $R_c$ strength characteristic with an average median value of 31.4%, the coefficient $k$ is significantly lower and equals to 14.6%.

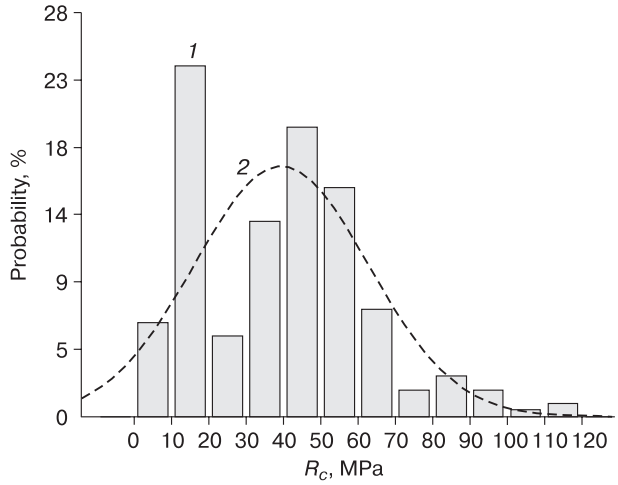


**Fig. 2. Summary of the (*1*) actual histogram and (*2*) theoretical variogram of the law of the normal probability distribution of the $R_c$ strength characteristic values.**

Sample size, 218 determinations.

Thus, the response of the HFVMD attenuation to the variability in the strength of the sandstone massif in Neryungri is weakened by the action of other permafrost and soil factors, such as temperature, mineral composition, grain-size distribution, type and composition of cement, presence of impurities, and other petrographic characteristics.

The result of the attenuation is visible on the histogram of the values of the coefficient $k$ constructed for the entire city of Neryungri (Fig. 4). In contrast to the same histogram of the $R_c$ strength characteristic (Fig. 2) in the histogram of the $k$ coefficient, there is no clear separation of the modes of the high and medium strength sandstone groups forming a mixed group with probable mode values in the range of 1.36–1.91 $m^{-1}$. The same group with a mode of 3.58–3.85 $m^{-1}$ is observed on the histogram on the right, combining sandstone groups of low, reduced, and moderately low strength.

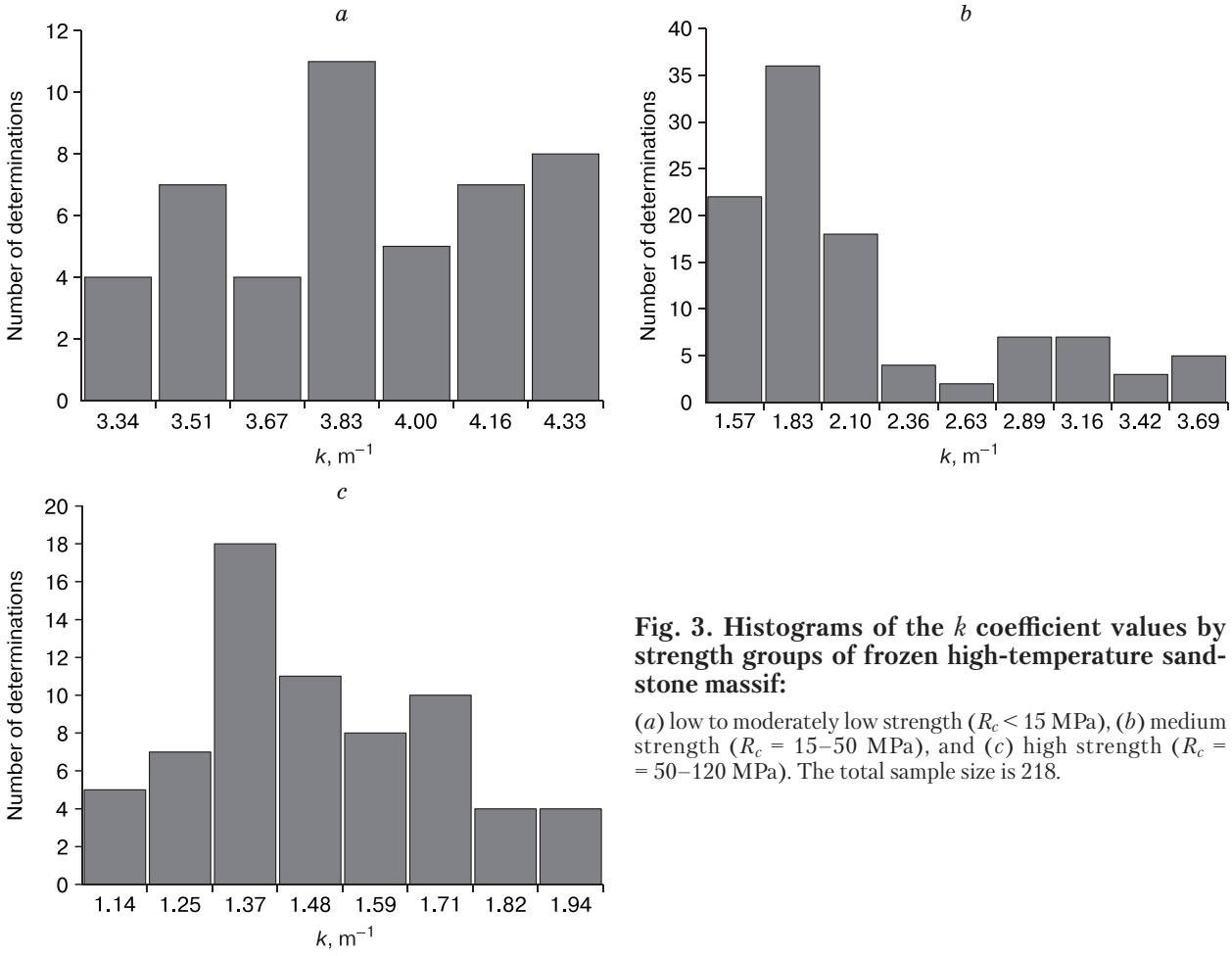


**Fig. 3. Histograms of the $k$ coefficient values by strength groups of frozen high-temperature sandstone massif:**

(*a*) low to moderately low strength ($R_c < 15$ MPa), (*b*) medium strength ($R_c$ = 15–50 MPa), and (*c*) high strength ($R_c$ = = 50–120 MPa). The total sample size is 218.

Table 2. **Statistics of the HFVMD attenuation in a frozen sandstone massif according to the coefficient $k$ values**

| Parameter | $k$, m$^{-1}$ | | |
|---|---|---|---|
| | groups 2–4 | group 5 | group 6 |
| Arithmetic mean | 3.86 | 2.14 | 1.49 |
| Median mean | 3.84 | 1.91 | 1.44 |
| Modal mean | 4.26 | 3.12 | 1.35 |
| Weighted mean | 3.88 | 2.21 | 1.49 |
| Standard deviation | 0.33 | 0.62 | 0.22 |
| Coefficient of variation, % | 8.4 | 29.0 | 14.6 |
| Minimum value | 3.26 | 1.44 | 1.08 |
| Maximum value | 4.41 | 3.82 | 1.99 |
| Sample size | 46 | 104 | 68 |

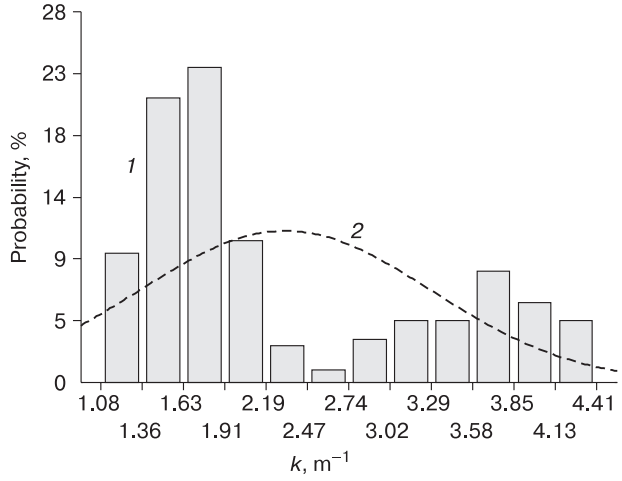


**Fig. 4. Summary of the (*1*) actual histogram and (*2*) theoretical variogram of the law of the normal probability distribution of the coefficient $k$ values for a frozen high-temperature sandstone massif.**

Sample size, 218 determinations.

The features of the probabilistic structure of the distribution of the values of the coefficient *k* show the weak and strong side of the EMI method in solving the problem of predicting the average strength of sandstone. The weak side is the difficulty of reliable recognition, even by the average values of the *k* coefficient, of a group of strong sandstones and a group of medium-strength sandstones forming one category of rocky soils in terms of construction [*GOST 25100-2020, 2020*]. The strength of the EMI method is a reliable distinction of the category of rocky soils from the category of semi-rocky soils (groups of sandstones of moderately low, reduced, and low strength). It is clear that the strength of the EMI method is of particular importance for design and survey work, especially for solving one of the main tasks of engineering-geological zoning of the built-up territories of South Yakutia and Neryungri according to the strength of the foundations of engineering structures.

## PROBABILISTIC MODEL

For a long time, the scale factor has been considered a fundamental obstacle to the application of probabilistic models linking geological and geophysical characteristics. The accumulated experience of field experiments shows that the incompatibility of point geological characteristics and volumetric geophysical characteristics is valid only in the space of disparate single determinations of these characteristics. When comparing a large number of values of geological and geophysical characteristics ordered by area and time, the dominant role of the scale factor loses its significance and does not interfere with detecting and studying statistical patterns [*Paskhaver, 1974*].

In the probabilistic model under consideration, in scientific terms, of course, the petrophysical side is interesting. It describes the correlation between the coefficient *k* and the strength characteristic $R_c$. In practical terms, another side of the model is important, which describes the physically unrealistic regression dependence of $R_c$ on *k*. It is this side of the model that provides a valuable opportunity to move from laboratory determination of the time limit of strength for uniaxial compression of water-saturated sandstone samples to a quantitative assessment of the same strength for a sandstone massif, that is, to solve the desired problem of predicting the strength of a sandstone massif according to the EMI method.

According to the rules and assumptions used in mathematical statistics, random variations of an independent variable associated with errors in laboratory determination should be insignificant in a probabilistic model in comparison with the general range of variability [*Draper, Smith, 2007, p. 41*]. This is a very strict theoretical condition, but it is practically met for the strength characteristic $R_c$, which is considered from the correlation side of the probabilistic model as an independent and non-random variable. In fact, with the relative variability of $R_c$ values equal to 191.5% (2.5–114.6 MPa), random variation of permissible laboratory errors of strength determination (no higher than ±20% according to [*GOST 21135.2-84, 1984*]) is only 10.4%.

The graph of the correlation dependence of *k* on $R_c$ is shown in Fig. 5. It follows from this dependence that the increase in the strength of the sandstone massif is accompanied by a regular nonlinear decrease in the average measure of attenuation of the HFVMD. The graph shows three sections with boundaries of sandstone strength groups [*GOST 25100-2020, 2020*]. The first section with a weak attenuation change and a correlation coefficient of –0.70 corresponds to a group of sandstone of moderately low, reduced, and low strength ($R_c < 15$ MPa). The second section with maximum attenuation variability and correlation coefficient –0.74 corresponds to a group of moderately strong sandstone with $R_c$ from 15 to 40 MPa. In the third section within the group of strong sandstone with $R_c > 40$ MPa, attenuation slows down again, but not as much as in the first section. At the same time, the correlation does not decrease and constitutes –0.79.

The described correlation is close to the cause-and-effect relationships that arise when the strength of the sandstone massif changes and the response to this variability of the measure of the HFVMD attenuation. It is difficult to say which mathematical functions correctly describe these relations, but with a high degree of probability, one of them is the logistic function. This function is known to correctly describe the behavior of natural-technical systems at their extreme transitions, i.e., from the initial state to the final state. In relation to the probabilistic model for Neryungri, the limiting transition is the transition from the low-strength sandstone to the strong sandstone in the rock–semi-rock basement of engineering structures.

The graph of the logistic function, constructed by the least squares method, is shown against the background of the scattering field of factual data on the paired values of $R_c$ and *k* (Fig. 5). The general record of the equation of the logistic function for all cases has the following form:

$$x = \left[ \left( a_0 + a_1 \right) \Big/ \left( 1 + a_2 \exp\left( a_3 y \right) \right) \right] + \delta,$$

where *y* is an independent variable (characteristic $R_c$); *x* is a dependent variable (coefficient *k*); $a_0, a_1, a_2, a_3$ are parameters depending on the conditions of application of the EMI method; and δ is a random error.

In relation to the engineering and geological conditions of construction and operation of engineering structures in Neryungri, the values of $a_0$–$a_3$ are equal to 1.2050, 3.5930, 0.1413, and 0.0795, respec-

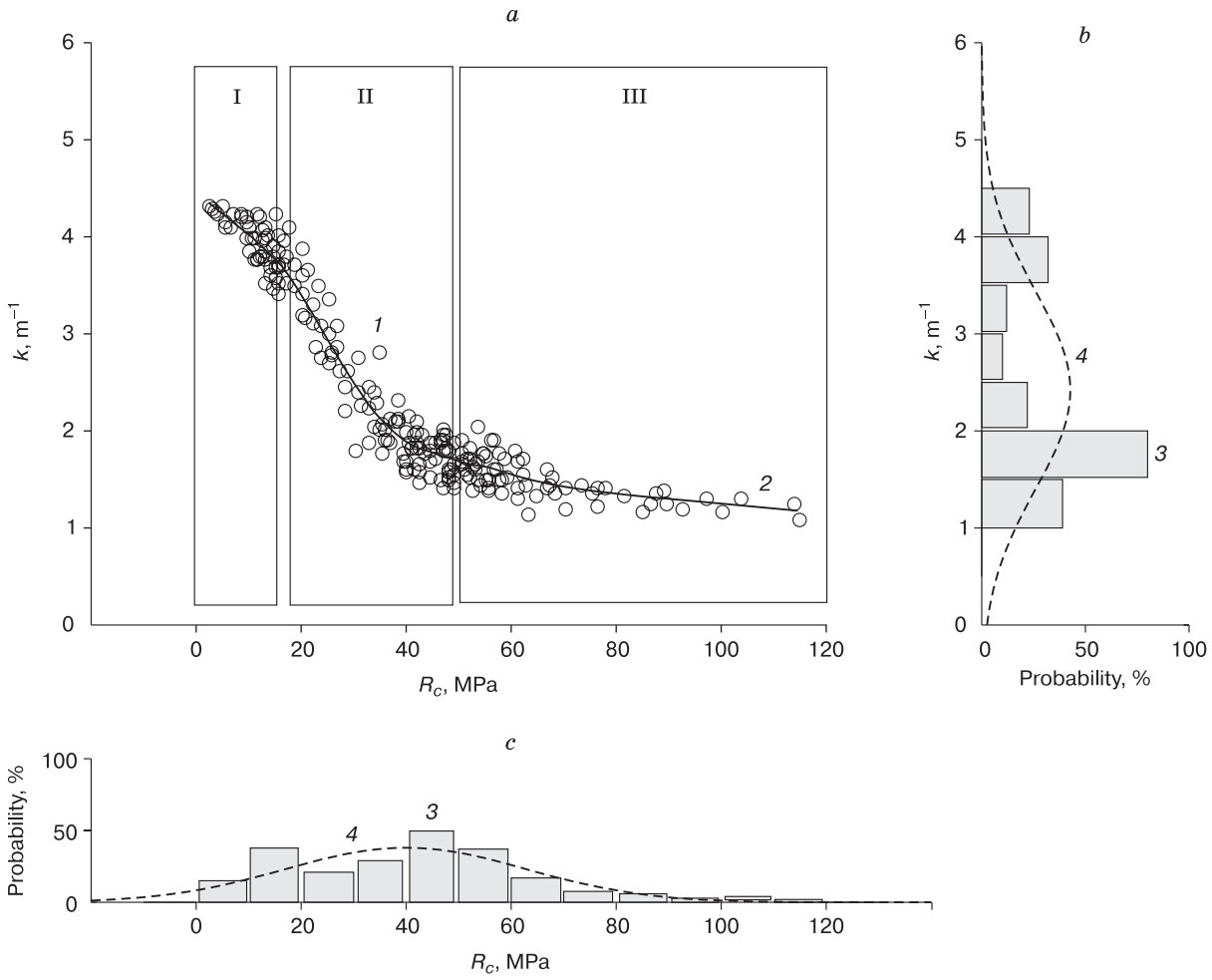


**Fig. 5. A probabilistic model for strength groups of water-saturated sandstone massif in accordance with [*GOST 25100-2020, 2020*] with the (*a*) correlation graph and graphs of probability distributions of the (*b*) coefficient *k* values and (*c*) strength characteristic $R_c$:**

(*1*) actual data, (*2*) graph of the logistic function equation, (*3*) actual histograms, and (*4*) theoretical variograms of the law of normal distribution. Strength groups of sandstone: (I) low to moderately low strength, (II) medium strength, and (III) high strength.

tively. They relate by probabilistic relations the strength of the sandstone massif and the average measure of the HFVMD attenuation with a multiple determination coefficient $R^2 = 0.959$. This means that the contribution of the strength factor to the variability of the attenuation of the HFVMD dominates among other factors and reaches almost 96%.

The graph of the logistic function equation is useful, because it makes it possible to solve a direct geophysical problem without calculations. Namely, at the design stage of the work, it is possible to estimate the measure of attenuation of the HFVMD by a priori data on the strength of the sandstone massif. In addition, knowing the values of the coefficient *k* according to the EMI method, it is easy to quickly solve two tasks in the field: (1) to obtain an initial assessment of the strength of the sandstone massif and (2) to construct a scheme of preliminary zoning of the studied territory by strength groups with division into categories of rocky and semi-rocky soils.

The inverse problem of geophysics – the prediction of the average strength of a water-saturated sandstone massif – is solved by a probabilistic model using a regression equation of a power function. It approximates the regular variability of the average values of the strength characteristic $R_c$ depending on the values of the coefficient *k* in the field of random scattering of factual data on Neryungri better than other functions. The graph of the power function equation is demonstrated in Fig. 6. It follows from this graph that the permutation of the places of variables has changed the mathematical form, but not the essence of the probabilistic relations between $R_c$ and *k*. Such a permutation should not cause confusion. It is inher-

ent in regression analysis and occurs when the direction of transition from one space of probabilistic relations of variables to another space changes.

The regression equation of a power function has the following form with a multiple determination coefficient $R^2 = 0.793$:

$$R_c = \exp(4.836)\, k^{-1.707}. \quad (3)$$

Equation (3) is applicable for surveys by the EMI method in the spring, when the seasonally thawing colluvial layer remains in the completely frozen state. Another condition for the correct application of this equation is the range of variability of the ensemble of the coefficient $k$ values (1.08–4.41 $m^{-1}$). Outside these boundaries, the parameters of equation (3) may be different.

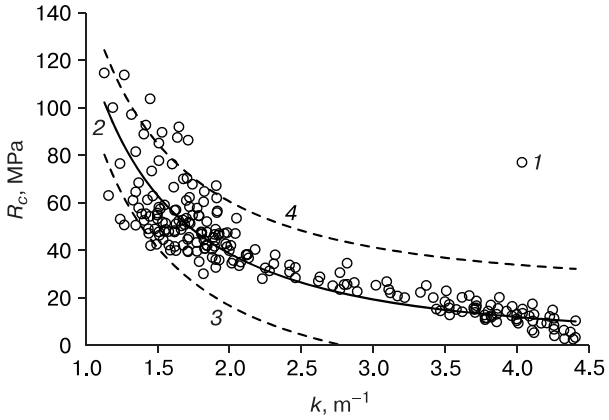


**Fig. 6. Probabilistic model for predicting the average strength of a sandstone massif ($R_c$) in a water-saturated state from the values of coefficient $k$:**

(*1*) actual material, (*2*) graph of the regression equation of the power function, and (*3*, *4*) lower and upper boundaries of the 95% confidence interval.

## FORECAST ERRORS

The errors of the probabilistic forecast model according to the EMI method of determining the average strength of a water-saturated sandstone massif present the difference between the laboratory values of the strength characteristic $R_c$ and the values calculated by equation (3). A test check made using the "Stage" program [*Kulaichev, 2006*] according to several independent criteria indicates that the probabilistic distribution of absolute and relative errors does not obey the normal law. This is also confirmed by the graphs of error histograms (Fig. 7). In 122 cases, errors have a positive sign and in 96 cases, a negative sign. Such an imbalance in the spread of single values near the averages is a mark of a certain tendency towards underestimating the calculated $R_c$ values in relation to laboratory values. The proportion of prediction errors of the probabilistic model, comparable in magnitude to the maximum permissible error of laboratory determination (±20%), is significant. In the actual material consisting of 218 determinations, errors of 20–30% occur in 61–78% of cases (Fig. 7*a*). A decrease in the sensitivity of the $k$ coefficient in the region of high values (above 4 $m^{-1}$) confined to an undivided group of low-strength sandstone, sandstone

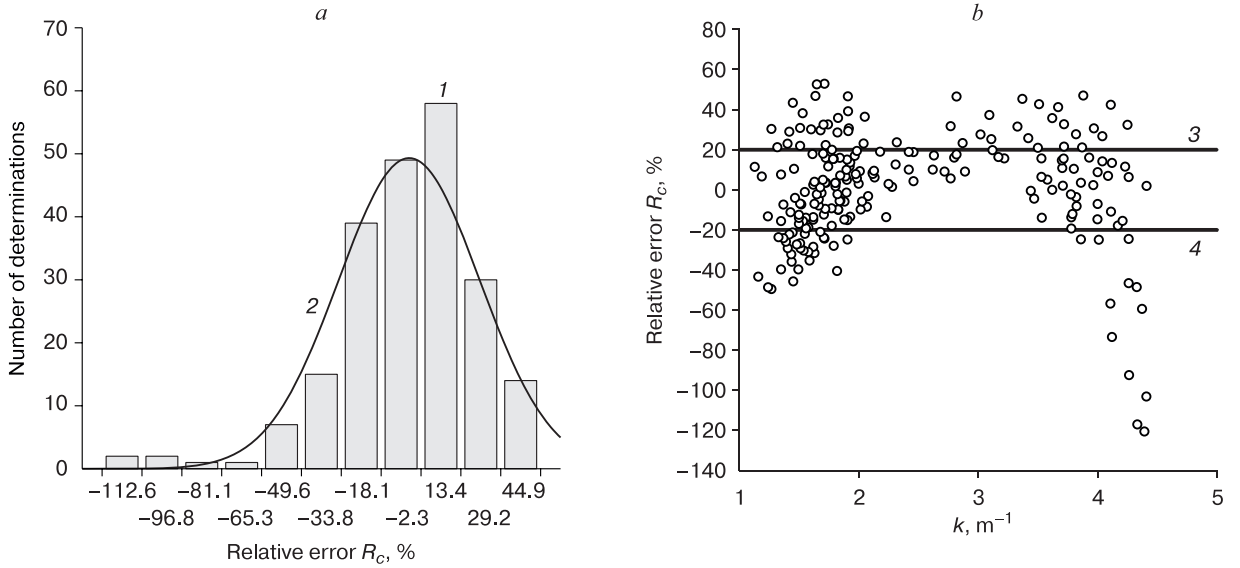


**Fig. 7. Graph of the distribution of errors of the probabilistic model (*a*) and the scattering field of model errors depending on the coefficient $k$ values (*b*).**

(*1*) actual histogram of errors, (*2*) theoretical variogram of errors according to the law of normal probability distribution, and (*3*, *4*) limits of the maximum permissible error of laboratory determination of the $R_c$ strength characteristic. Sample size, 218 determinations.

Table 3. **Statistics of errors of the probabilistic model of the average strength forecast of the sandstone massif in the water-saturated state according to the EMI method data**

| Parameter | $R_c$ error | |
|---|---|---|
| | MPa | % |
| Arithmetic mean | 0.65 | 0.21 |
| Standard error | 0.76 | 1.88 |
| Median mean | 1.04 | 3.50 |
| Modal mean | 1.75 | 3.50 |
| Standard deviation | 11.24 | 27.78 |
| Coefficient of variation, % | 17.3 | 132.3 |
| Minimum value | –34.7 | –120.5 |
| Maximum value | 38.2 | 52.8 |
| Sample size | 218 | 218 |

of reduced and low strength with average calculated values of the $R_c$ strength characteristic <15 MPa leads to an abnormal increase in errors up to –120%, i.e., to a systematic excess of the laboratory values of the $R_c$ strength characteristic (Fig. 7*b*). The share of such errors is equal to 8.2–9.6%. A more favorable pattern of error distribution for the EMI method is observed at relatively low values of the coefficient $k$ (<1.8 $m^{-1}$) for a group of strong sandstone with an estimated $R_c$ > 50 MPa. In this case, the maximum error does not exceed ±55%, and the share of such errors in relation to errors of ±(20–30)% is ±34.5 and ±20.7%.

It turns out that in about 7–8 cases out of ten, the expected forecast error will fall within the range of ±(20–30)%. With the variation of single errors from 1.75 MPa (3.5%) to 11.24 MPa (27.8%), the average error rates are close to zero (Table 3). If we take the moderate level of confidence[3] in the results of geophysics equal to about 70%, which has been accepted for a long time in geology in the prospecting and exploration of mineral deposits, then the calculation errors of the average $R_c$ values will be concentrated in the range ±11.22 MPa (±27.7%). At the confidence level of 80%, the errors become slightly larger and equal to ±14.07 MPa (±32.0%).

## CONCLUSIONS

A retrospective analysis of the factual material obtained in the 1990s in the permafrost of southern Yakutia in Neryungri allowed us to build a new probabilistic model. This model makes it possible to solve an important problem of geomechanics of frozen soils in terms of predicting the average strength of a frozen high-temperature sandstone massif that has passed into a water-saturated state under the influence of anthropogenic, technogenic and climatic factors on the basis of data obtained by the EMI method. With a probability of 70–80%, the model allows us to estimate the strength of the sandstone massif in this state with a relative error of ±(27.7–32.0)%. This error is comparable with the permissible laboratory error of ±20%. Such a level of accuracy gives grounds to apply the EMI method for the purpose of quick (ahead of expensive and labor-intensive drilling and laboratory works) economical and detailed zoning of the territory of Neryungri according to the strength category of rocky–semi-rocky foundations of engineering structures.

***Acknowledgments.*** *The author is grateful to N.L. Zykov, Deputy Director of Neryungristroyiziskaniya LLC, who has passed away, for admission to the materials of surveys in Neryungri; to Ph.D. A.E. Melnikov from the Laboratory of Engineering Geocryology of Melnikov Permafrost Institute, Siberian Branch of the Russian Academy of Sciences for the search for materials on the geology of South Yakutia; and to the former chief geophysicist of YuzhYakuttisiz G.K. Suvorova for participation in experimental and methodological work on application of the EMI method and valuable consultations on the geoelectric and seismic structure of frozen soils in Neryungri.*

## References

Akimov A.T., 1971. Theoretical and practical issues of electrical sounding of permafrost. In: *Proceedings of PNIIIS, USSR Gosstroy. Vol. VI. Geophysical Methods in Engineering Investigations*. Moscow, Publishing House of the Industrial Research Institute in Construction, p. 6–73 (in Russian).

Basarir H., Tutluoglu L., Karpuz C., 2014. Penetration rate prediction for diamond bit drilling by adaptive neuro-fuzzy inference system and multiple regressions. *Eng. Geol.* **173**, 1–9.

Boaga J., 2017. The use of FDEM in hydrogeophysics: a review. *J. Appl. Geophys.* **139**, 36–46.

Buldovich S.N., Melentiev V.S., Naumov M.S., Furikevich O.S., 1976. The role of recent faults in the formation of permafrost-hydrogeological conditions (an example of the Neryungri syncline of the southern Yakutian Mesozoic trough). *Merzlotnye Issledovaniya* (Permafrost Research), Moscow, Izd. Mosk. Gos. Univ., iss. XV, p. 120–125 (in Russian).

Doolittle J.A., Brevik E.C., 2014. The use of electromagnetic induction techniques in soils studies. *Geoderma* **223–225**, 33–45.

Draper N., Smith H., 2007. *Applied Regression Analysis*, 3rd ed. Translated from English. Moscow, Williams Publishing House, 917 p. (in Russian).

GOST 21135.2-84, 1984. *Rocks. Methods for Determining Uniaxial Compression Strength*. Moscow, Izd-vo Standartov, 1984, 7 p. (in Russian).

GOST 25100–2020, 2020. *Soils. Classification*. Moscow, Standartinform, 2020, 38 p. (in Russian).

Grib N.N., Samokhin A.V., 1999. *Physical and Mechanical Properties of Coal-Bearing Rocks of the South Yakutian Basin*. Novosibirsk, Nauka, 240 p. (in Russian).

[3] This is a relatively low level of confidence, but sufficient to assess the reliability of the results obtained by geophysical methods taking into account their geological ambiguity and mathematical incorrectness of solving inverse problems.

Frantov G.S. (ed.), 1984. *Guidelines on Electrical Sounding*. Leningrad, Nedra, 534 p. (in Russian).

Igolkin V.I., Shaidurov G.Ya., Tronin O.A., Khokhlov M.F., 2016. *Methods and Instruments for AC Electrical Sounding*. Krasnoyarsk, Siberian Federal University Press, 272 p. (in Russian).

Kudryavtsev V.A. (ed.), 1975. *Southern Yakutia: Permafrost-Hydrogeological and Engineering-Geological Conditions of the Aldan Mining Region*. Moscow, Izd. Mosk. Gos. Univ., 444 p. (in Russian).

Kulaichev A.P., 2006. *Methods and Tools of Comprehensive Data Analysis*. Moscow, FORUM: INFRA-M, 512 p. (in Russian).

Lebedev V.F., Onushchenko V.I., Litvintseva L.M., 1991. *MEMS Complex. Toolkit*. Krasnoyarsk, Izd. NPO Sibtsvetmetavtomatika SSSR, 83 p. (in Russian).

McNeill J.D., 1980. *EM-34-3 Survey Interpretation Techniques. Technical Note TN-8*. Ontario, Canada, Geonics Limited Mississauga, 15 p.

Melnikov V.P., 1977. *Electrophysical Studies of Permafrost*. Novosibirsk, Nauka, 108 p. (in Russian).

Molochnov G.V., Radionov M.V., 1983. *Frequency Electromagnetic Sounding with a Vertical Magnetic Dipole*. Leningrad, Izd. LGU, 217 p. (in Russian).

Neradovsky L.G., 2018. *Technology of Electromagnetic Sounding of Frozen Soils of the Layer of Annual Heat Exchange*. Moscow, ANO Nauchn. Obozrenie, 622 p. (in Russian).

Neradovskiy L.G., 2022. Engineering characterization of geological features in frozem sedimentary rocks using GPR, Neryungri, Southern Yakutia. *Razvedka i Okhrana Nedr*, no. 1, 41–54 (in Russian).

Neradovsky L.G., Fedorova L.L., 2015. Determination of the strength properties of sedimentary and intrusive rocks in the permafrost zone of South Yakutia using GPR. *Gornyi Inform.-Analitich. Byull.*, no. 10, 201–210 (in Russian).

Neradovsky L.G., Syasko A.A., 2015. Statistical patterns of electromagnetic properties of rocks in the permafrost zone of South Yakutia. *Inzhenern. Izyskaniya* **10** (11), 66–73 (in Russian).

Paskhaver I.S., 1974. *The Law of Large Numbers and Statistical Regularities*. Moscow, Statistica, 152 p. (in Russian).

Petrovsky A.A., 1971. *Radio Wave Methods in Subsurface Geophysics*. Moscow, Nedra, 224 p. (in Russian).

Sartorelli A.N., French R.B., 1982. Electromagnetic induction methods for mapping permafrost along northern pipeline corridors. In: *Proc. 4th Canadian Permafrost Conf.*, Calgary, Alberta, March 2–6, 1981. Ottawa, National Research Council of Canada, p. 283–295.

*System of Medium-Frequency Equipment for Electromagnetic Sounding (MEMS). Technical Description*, 1991. NPO Sibtsvetmetavtomatika USSR. Krasnoyarsk, 30 p (in Russian).

Titlinov V.S., Zhuravleva R.B., 1995. *Technology of Geometric Inductive Sounding*. Yekaterinburg, Nauka, 56 p. (in Russian).

Veshev A.V., Lyubceva E.F., Leonchikov V.M., Alekseev V.M., 1978. *Interim guide to the method of electromagnetic sounding with a vertical magnetic dipole*. Moscow, USSR Ministry of Nonferrous Metallurgy, 45 p. (in Russian).

Vladov M.L., Sudakova M.S., 2017. *Ground-Penetrating Radar. From Physical Foundations to Promising Directions. Tutorial*. Moscow, GEOS, 240 p. (in Russian).

Yakupov V.S., Kalinin V.M., Akhmetshin A.A., Danilov V.S., 1998. A probabilistic geoelectrical model for the frozen ground in Middle and Eastern Siberia. *Izv. Physics Solid Earth* **34** (7), 608–611.

Zaderigolova M.M., 1998. Radio Wave Method in Engineering Geology and Geoecology. Moscow, Izd. Mosk. Gos. Univ., 320 p. (in Russian).

Zhelinsky V.M., 1980. *Mesozoic Coal-Bearing Formation of South Yakutia*. Novosibirsk, Nauka, 119 p. (in Russian).

Zhuravleva R.B., Samodelkina S.A., Bakaev V.P., 1994. On the choice of interpretation parameters for geometric sounding and profiling using the DEMP-SC system. *Ross. Geofizicheskii Zh.*, no. 2–4, 67–70 (in Russian).

*Received January 21, 2022*
*Revised May 25, 2022*
*Accepted November 12, 2022*

*Translated by S.B. Sokolov*

**EARTH'S CRYOSPHERE**
SCIENTIFIC JOURNAL

*Earth's Cryosphere*, 2022, vol. XXVI, No. 6, pp. 50–51

*REVIEW*

# REVIEW OF A NEW BOOK BY L.N. KHRUSTALEV *"CALCULATION OF ENGINEERING CONSTRUCTIONS ON PERMAFROST"*

**A.Yu. Gunar**

*Lomonosov Moscow State University, Faculty of Geology, Leninskie Gory 1, Moscow, 119911 Russia*

**Corresponding author; e-mail: gunar_91@mail.ru*

A recently published book by L.N. Khrustalev, a leading specialist in engineering geocryology, professor of the Department of Geocryology, Faculty of Geology, Lomonosov Moscow State University is devoted to methods for solving a wide range of problems of engineering geocryology: thermal and mechanical interaction of engineering constructions with bearing rocks, land reclamation measures, methods for assessing the reliability of design solutions for construction in the permafrost zone, as well as methods of predictive calculations for monitoring of objects built on permafrost. This monograph contains a wide range of recommendatory and standard calculations, as well as some previously unpublished author's works. In essence, it is a desk reference for specialists involved in the design and calculations of engineering constructions on permafrost. Another highlight of the book is its electronic component: all the calculations proposed in the book are implemented in Microsoft Excel macros and are available for download and processing. This practically eliminates the possibility of errors (the user only needs to enter the correct input data).

***Keywords:*** *permafrost engineering, book, thermo-technical calculation, reliability.*

***Recommended citation:*** Gunar A.Yu., 2022. Review of a new book by L.N. Khrustalev "Calculation of engineering constructions on permafrost". *Earth's Cryosphere* **26** (6), 50–51.

In 2021, a fundamental book by Prof. L.N. Khrustalev – *Calculation of Engineering Constructions on Permafrost: A Training Manual* – was published. This book is a training manual for study courses *Basics of Geotechnics on Permafrost* and *Reclamation of Frozen and Thawed Ground in Permafrost Area* for the Master of Science program (first study year). However, it can be used not only as a training manual for students of the high school (geology, civil engineering, and transport programs) but also as a reference book for scientists, designers, civil engineers, and surveyors dealing with the problems of economic development in permafrost areas.

Lev Nikolaevich Khrustalev is a prominent permafrost researcher, who has been working on geotechnical problems in permafrost areas for more than 60 years. He worked at the Northern Branch of the Institute of Foundations and Underground Constructions of the State Committee for Construction in the Soviet Union (Gosstroy) in Vorkuta for twenty-six years, and at the Geocryology Department of Lomonosov Moscow State University for thirty-seven years. He is a doctor of technical sciences, professor, Honored Inventor of the Komi ASSR, Honored Scientist of the Russian Federation, Honored Professor of MSU. He is the author of over 180 scientific and methodological publications, including 23 books and 33 patents for inventions. A number of these inventions have been implemented into practice with great economic effect.

The recently published book accumulates computational analytical methods applied in the design of engineering constructions on permafrost and available from regulatory and technical literature. The training manual consists of five chapters:

1. Problems of thermal interaction between engineering constructions and frozen ground.
2. Problems of mechanical interaction between engineering constructions and frozen ground.
3. Related problems of thermal and mechanical interaction between engineering constructions and frozen ground.
4. Safety of engineering constructions on permafrost.
5. Problems of engineering construction monitoring on permafrost.

The first chapter describes the methods for the assessment of the dynamics of the thermal state of permafrost under the impact of engineering constructions (freeze-thaw cycles, active layer depth) depending on the adopted technical solutions. The second chapter considers procedures for calculating the bearing capacity of foundation, its subsidence, estimates of heaving power, as well as calculations of linear objects. Further, methods of thermo-technical calculations for civil engineering facilities at sites with deepened permafrost table (artificial thawing, stabilization of the upper permafrost, and calculation of the working layer for railways and highways) are considered. The fourth chapter should be specially high-

lighted: t contains personal developments of L.N. Khrustalev on the approaches for analytical safety estimations of building foundations and linear constructions. These developments focus on the choice of design solutions allowing to reduce the risks of failures of geotechnical systems by determining the optimal parameters of foundations and geotechnical systems. That is the one of most important design objectives. The fifth chapter presents calculation methods allowing to perform predictive calculations of the ground temperature field based on monitoring observations, i.e., temperature measurements in a borehole located at some distance from a building or pipeline.

The book aims at accelerating the process of thermotechnical calculations; several normative calculation methods have been revised: for each particulate method, the steps of calculation are given sequentially and in detail, without references to equations given in other chapters. The equations that have no analytical solutions are replaced by tables or approximated by linear functions. This approach significantly simplifies the calculations for the user. It should be noted that the search of the source literature is simple: reference sources are given within each chapter, where the equation is described in detail. When the equation is published for the first time, the description is given in the book. The derivations of the equations can also be found in the textbook by L.N. Khrustalev [*2019*]. The presented training manual is an excerpt from this book with several additions that were developed during the last two years after the textbook publication.

Calculation methods presented in the book were implemented by L.N. Khrustalev in the form of 44 MS Excel macros. They are stored in the cloud and can be requested using the link given in the book appendix. Macros work in the Excel environment, which makes them understandable and available for readers even without special training. The work with these programs is easy: user must only fill out the input column highlighted with yellow color and click the "Start" button located in the upper part of the sheet. Calculation results will appear in the gray column of this sheet. Herewith, the calculations are accelerated by several orders and are not subject to errors.


The new books by L.N. Khrustalev can be recommended for readers interested in engineering permafrost issues and specialists dealing with the economic development of areas underlain by permafrost. They can be ordered from publishers by phone:

+7 (495) 280-15-96 (add. 246) – "Infra-M" Publishing House

8-800-333-68-45 – "Direct-Media" Publishing House

## References

Khrustalev L.N., 2019. *Fundamentals of Geotechnics on Permafrost*. Moscow, INFRA-M, 543 p. (in Russian).

Khrustalev L.N., 2021. *Calculation of Engineering Constructions on Permafrost: A Training Manual*. Moscow; Berlin, Direct-Media, 124 p. (in Russian).

*Received Novermber 17, 2021*

*Translated by Yu.A. Dvornikov*